Digital Volume Correlation: Review of Progress and Challenges

Ante Buljac, Clément Jailin, Arturo Mendoza, J Neggers, T. Taillandier-Thomas, Amine Bouterf, Benjamin Smaniotto, François Hild, Stéphane Roux

Experimental Mechanics manuscript No.
(will be inserted by the editor)

Digital Volume Correlation: Review of Progress and Challenges

Ante Buljac · Clément Jailin · Arturo Mendoza · Jan Neggers · Thibault Taillandier-Thomas · Amine Bouterf · Benjamin Smaniotto · François Hild · Stéphane Roux

Received: date / Accepted: date

Abstract 3D imaging has become popular for analyzing material microstructures. When time lapse series of 3D pictures are acquired during a single experiment, it is possible to measure displacement fields via digital volume correlation (DVC), thereby leading to 4D results. Such 4D analyses have been performed for almost two decades. The present paper aims at reviewing the achievements of and challenges faced by such measurement technique. Ex-situ and in-situ experiments are discussed. A general and unified DVC framework is introduced. Various sources of measurement bias and uncertainties are analyzed. The current challenges are studied and some propositions are given to address them.

Keywords DVC · In-situ test · Laminography · Regularization · Tomography · Uncertainty quantification

A. Buljac, C. Jailin, A. Mendoza, J. Neggers, T. Taillandier-Thomas, A. Bouterf, B. Smaniotto, F. Hild,* S. Roux
LMT, ENS Paris-Saclay / CNRS / Univ. Paris-Saclay
61 avenue du Président Wilson, F-94235 Cachan Cedex, France
*Corresponding author. Email: hild@lmt.ens-cachan.fr

Foreword

The present paper aims at reviewing the major developments in Digital Volume Correlation (DVC) over the past ten years. It follows the first review on DVC that was published in 2008 by its pioneer [11]. In the latter, the interested reader will find all the general principles associated with what is now called local DVC. They will not be recalled hereafter. In such approaches the region of interest is subdivided into small subvolumes that are *independently* registered. In addition to its wider use with local approaches, DVC has been extended to global approaches in which the displacement field is defined in a dense way over the region of interest. Kinematic bases using finite element discretizations have been selected. To further add mechanical content, elastic regularization has been introduced. Last, integrated approaches use kinematic fields that are constructed from finite element simulations with chosen constitutive equations. The material parameters (and/or boundary conditions) then become the quantities of interest.

These various implementations assume different degrees of integration of mechanical knowledge about the analyzed experiment. First and foremost, DVC can be considered as a stand-alone technique, which has seen its field of applications grow over the last ten years. In this case the measured displacement fields and post-processed strain fields are reported. With the introduction of finite element based DVC, the measured displacement field is continuous. It is also a stand-alone technique. However, given the fact that it shares common kinematic bases with numerical simulations, it can be easily combined with the latter. One route is to require local satisfaction of equilibrium via mechanical regularization. Another route is to fully merge DVC analyses and numerical simulations via integrated approaches. Different examples will illustrate how these various integration steps can be tailored and what are the current challenges associated with various approaches.

Contents

1 Introduction

Computed (x-ray) tomography (CT), magnetic resonance imaging (MRI), optical coherence tomography (OCT), positron emission tomography (PET), single photon emission computed tomography (SPECT) are five well-known modalities in the medical field. They have revolutionized the way medical diagnosis is performed [102,138,167]. The new opportunities offered by these 3D imaging techniques have led to considerable instrumentation developments since the mid 90s, and increased accessibility have made microtomography one tool of choice in material science [142,200, 208]. It is possible to inspect internally industrial or natural materials [8,51] using lab tomographs or tomography beamlines at synchrotron radiation facilities. The microstructure of different materials can be visualized and quantified in nondestructive or minimally intrusive manner [208, 144].

For diagnosis, treatment and basic science [102] among other reasons, there is a need for developing intra- and inter-modality registrations [228,141,102]. In particular, following temporal motions of bones or tissues calls for registering different images for a better apprehension of qualitative and quantitative changes. Here again, medical applications have been a major driver for very early works especially from the image processing community (optics and applied mathematics). The same benefit is found in materials science, when the *same* sample is imaged in the bulk at different levels of load. Localization bands were first revealed within sand samples when x-rayed ex-situ [50].

Specific loading apparatus were subsequently designed to be compatible with the absorption of x-rays to perform in-situ tests. This is one critical element to consider when designing such testing devices [85,12,56]. Mechanical experiments coupled with x-ray tomography began with the observations of crack openings in aluminum alloy [85]. Other tests coupled with in-situ tomographic observations were developed over the years [26]. Significant progress was made in the design of new testing setups and more importantly on the understanding of various degradation mechanisms

that could only be revealed thanks to observations in the bulk of materials [56,26]. Depending on the imaging modality and the studied material, the loading device had to be adapted to the experimental environment [14,164,72].

Having access to ex-situ or in-situ observations during different types of loading histories, the next critical step was the measurement of displacement fields in the bulk of imaged samples. The first 3D displacement measurements via so-called *Digital Volume Correlation* (DVC) were performed on trabecular bone compressed in-situ in a computed microtomographic (µCT) scanner [12]. A *local* approach was implemented. Other applications followed in the field of biomechanics (*e.g.,* see Refs. [194,11,106,241,17,193,44,40,43,109]). At the beginning of the current decade, DVC was clearly identified as one technique very suited to biomechanical applications [239]. For instance, local variations in microstructure were associated with failure patterns in the vertebra [220]. The internal strain and failure in prophylactically-augmented vertebrae were studied thanks to DVC analyses [47]. The authors showed that the failure initiated inside the augmented vertebral body, next to the injected cement mass. Noninvasive assessments of the intra-vertebral heterogeneity in density improved the predictions of vertebral strength and stiffness [107].

In solid mechanics, different classes of materials were investigated thanks to DVC measurements. Very early on, various types of foams were imaged via tomography and their behavior was studied thanks to DVC [207,11,197,181,59,15,64]. The degradation mechanisms of such materials in indentation experiments received some attention [231,20,22]. One of the reasons is that tomography reveals their in-situ temporal development, which can only be assessed post-mortem with other investigations. Such observations were subsequently compared with numerical simulations for (in)validation purposes [201,21].

Localized phenomena are situations in which full-field measurements make a (huge) difference (*e.g.,* strain localization [127,1,214,49] and cracks [198,231,94]). This is particularly true when kinematic measurements can be performed nondestructively in the material bulk. Very het-

erogeneous strain fields were measured by *global* DVC in a compression test on polypropylene solid foam [197]. When analyzing compressed stone wool, it was shown that the material density was responsible for local heterogeneities in strains, and that correlations existed between local density and strain [97]. Similar trends were observed in low density wood fiberboard [222]. For cellulose fiber mats correlations between high density gradient zones and maximum eigen strains were reported [112]. More recently it was shown that the volume change in Si-based electrodes increased with the lithiation degree, while the gray levels decreased with respect to the original (*i.e.,* nonlithiated) state [178].

Nodular graphite cast iron, which is a model material for DVC analyses, has been extensively studied. Crack initiation was analyzed in very high cycle fatigue experiments with evaluated strain fields [66]. Stress intensity factor profiles were extracted from experimentally measured displacement fields [133]. Crack opening displacements were also evaluated in graphite via DVC [160, 163]. A single macrocrack was studied in a double torsion experiment on recrystallized porous silicon carbide by analyzing displacement and correlation residual fields [128]. Delamination in layered composites was quantified with the use of displacement [125] or strain [19] fields. Crack propagation features were analyzed. In particular, the local crack propagation law was extracted from the kinematic measurements [132]. Likewise, crack initiation was observed in cast aluminum alloy with kinematic and residual fields [234]. Short fatigue cracks were analyzed in cast magnesium alloy with the measured bulk displacement fields [147]. Stress intensity factor profiles were extracted from the analysis of a short fatigue crack in cast iron [119]. Such analyses are very challenging since the graphite nodules interact with short cracks.

Granular materials usually possess sufficient x-ray absorption contrast to enable for DVC analyses [69]. Force chains in Mason sand was evaluated by considering the minor eigen strains evaluated via DVC measurements [103]. The analysis of multiple debond cracks was shown to be possible in a tensile test on a propellant-like material thanks to global DVC by using the

correlation residuals [95]. The same mechanism was found in polymer bonded sugar in uniaxial compression [104]. The gray level residuals were also used to detect matrix/nodule debonding in cast iron [93, 219, 29]. Maximum eigen strain fields enabled multiple microcracking to be quantified in brittle materials [101, 231, 94, 240] and damage in SiC/SiC composites [201]. Other strain descriptors such as the first and second invariants were used to detect cracks [38].

The effect of temperature on the material response was analyzed thanks to ex-situ and in-situ tests. Cracking induced by accelerated (*i.e.,* ex-situ) desiccation of a cement paste containing glass beads was quantified via DVC [101]. Similarly, accelerated maturation of Kimmeridge clay was monitored in-situ up to 380°C [63] with 2-min acquisitions of 1800 radiographs. Sintering of copper was monitored in-situ at 1050°C. The motion of particles and shrinkage (*i.e.,* volumetric) strain fields were evaluated [151]. This type of approach corresponds to the first step toward model validation of sintering processes. In-situ thermomechanical tests have started in part thanks to fast acquisitions on synchrotron lines. Fatigue initiation and propagation mechanisms were analyzed in-situ at temperatures up to 250°C in cyclic tensile tests on Al-Si alloy [45]. The duration of each tomographic scan was 45 s. Thanks to fast acquisitions (*i.e.,* 4 s for 720 acquired projections per tomogram) damage mechanisms were observed and quantified in terms of strain fields during in-situ uniaxial compression of a semi-solid Al-Cu alloy at 550°C [32].

Most of the DVC analyses reported so far were based upon x-ray µCT. This technique is suited to elongated (*e.g.,* axisymmetric or cylindrical) samples. However, plate-like samples can also be imaged via computed laminography [87]. When compared to µCT [131], it leads to higher levels of measurement uncertainties [156], which are partly due to the missing spatial frequencies and reduced resolution of laminographic scans along the rotation axis [238]. However, it could still be used to analyze the flat-to-slant transition of ductile tearing of aluminum alloys for low stress triaxialities with global DVC [156, 158, 30] and regularized DVC [214, 157].

Registration of medical Magnetic Resonance images has been carried out for a long time for diagnosis and treatment purposes (*e.g.,* see Refs. [228, 209, 141, 102, 199, 195]). Conversely, there are very few results of in-situ mechanical tests imaged via MRI or µMRI. Global DVC was applied to the analysis of a compression test on cancellous bone [14]. It was shown that the measurement uncertainties were at most of the same order as for CT and that very early on such materials did not deform uniformly. Global DVC was applied to cardiac magnetic resonance images of a healthy human subject. A finite strain regularization framework was implemented [76].

All the previous examples dealt with opaque (to the human eyes) materials. For transparent materials, other methods can be used. For instance, fluorescence confocal microscopy was used to measure 3D displacements of compressed aragose gel containing fluorescent particles. In that case, the warping of each sub-volume was described by six degrees of freedom (*i.e.,* three translations, and three diagonal component of the stretch tensor [71]). Laser-scanning confocal microscopy can also be used to measure the deformation of the same material [105]. So-called cellular surface traction forces were determined by combining the previously mentioned imaging technique and DVC [148]. It was also shown that contractile forces regulate cell divisions [129]. Randomly distributed particles in transparent resins scatter light when illuminated by a planar laser beam [77]. When the position of the laser beam is changed, a stack of planar slices is obtained and can be registered by DVC. When compared to CT data, similar uncertainty levels were reported. Optical coherence tomography is another 3D imaging technique to image semi-transparent materials. It was shown that full-field OCT setups were well adapted to perform static elastography of tissue samples via regularized DVC [164]. Local DVC was used to monitor an inflation test on porcine cornea [72].

This non exhaustive literature review shows that many applications have been made possible thanks to the use of 3D imaging techniques combined with early ex-situ and now more frequently in-situ mechanical tests. DVC is becoming a tool of choice to quantify various deformation and

failure mechanisms. Gradually experimentally measured displacement fields are being compared with 3D numerical simulations for validation and identification purposes. To further illustrate the increased interest in DVC analyses, Figure 1 shows the yearly number of citations counted by the "Web of Science" platform. The one hundred mark was reached in 2010.

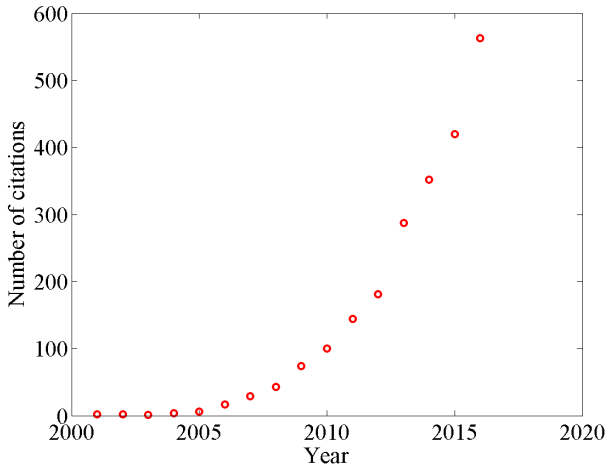

Fig. 1 Number of citations when the chosen topic is "Digital Volume Correlation" via Web of Science search on June 23, 2017

Even though many achievements have been reported, a number of cases/materials remain challenging. This papers aims at discussing many of them. However, the first required step is to summarize various 3D imaging techniques and to describe the possible artifacts they may induce in their quantitative use via DVC analyses. The next step is to review issues associated with ex-situ and in-situ mechanical tests. Various DVC approaches have been proposed in the last two decades. They are summarized and illustrated with examples. In order not to duplicate the existing review on local approaches [11], more emphasis is put on global approaches. One key aspect of DVC analyses is their uncertainty quantification, which is partly related to the way 3D images are obtained. Last, some research directions are sketched to address questions and

limitations of current implementations of DVC algorithms and their subsequent use for modeling and simulation purposes.

2 Three-dimensional imaging of unloaded and loaded materials

2.1 Three-dimensional imaging of materials

The aim of this section is not to give an exhaustive and detailed overview of 3D imaging. The reader will find general sources of information in all of the discussed techniques. Rather the focus is put on the possible consequences of the use of each technique in conjunction with DVC analyses (*e.g.,* artifacts induced by the acquisition process).

2.1.1 Tomography and laminography

X-ray computed tomography (or CT) produces 3D images of objects from a set of 2-dimensional x-ray images (*i.e.,* projections). In a CT system, the component to be imaged is placed on a turntable or a rotating axis between the radiation source and the imaging system. While the sample is rotated, the digital detector records a large set of 2D x-ray images for different angular positions. The x-ray attenuation (or sometimes phase contrast) map is then *computed* or *reconstructed* from these 2D projections. Various algorithms are available to carry out this reconstruction [114]. The x-ray source is either produced in a synchrotron facility (for which the x-ray beam is generally parallel, monochromatic and coherent) or by an x-ray tube (*e.g.,* microfocus sources) for lab tomographs where the beam is cone shaped, polychromatic and incoherent. The typical resolution is of the order of 1 to 10 µm per voxel for micro-CT. Therefore x-ray microtomography is sometimes referred to as x-ray microscopy [55,177].

There are numerous sources of artifacts in computed tomography [48]. Some of them lead to gray level variations (*e.g.,* beam hardening with polychromatic x-ray sources), specific curves

(*e.g.,* streak or ring artifacts) and some are associated with spurious motions (*e.g.,* source motion for lab systems, sample motion, wobbling) that degrade the reconstruction qualities. Not all of them are impacting DVC analyses. However, careful analyses should be performed to evaluate measurement uncertainties before reporting any result (see Section 4).

In tomography, the rotation axis is perpendicular to the x-ray beam. Consequently, most of the imaged samples have stick-like shapes so that the total x-ray attenuation does not vary too much between different angular positions. If the rotation axis is no longer parallel to the detector plane, then thin sheets can be imaged. This type of imaging configuration is designated as laminography [87], which is used for non destructive evaluations (NDEs) in the micro-electronics industry [81], but micrometer resolution is restricted (up to now) to synchrotron facilities thanks to the use of parallel beams.

All the artifacts listed above for computed tomography may occur in computed laminography as well. Further, it is noteworthy that the sampling of the 3D Fourier domain of the region of interest is incomplete in laminography [88], which leads to additional imaging artifacts [238]. These artifacts may degrade the displacement and strain resolutions when DVC is applied [156]. In Section 4.1, displacement and strain uncertainties are studied for three different materials that are imaged via laminography. Figure 2 shows sections of the three reconstructed volumes. For the two aluminum alloys, the volume fraction of features (*i.e.,* pores and secondary inclusions) to be used in DVC analyses is less than 0.8 % for the AA2139 grade (Figure 2(a)), and 0.3 % volume fraction of metallic inclusions (Figure 2(b)) for the AA2198 grade. Nodular graphite cast iron has different microstructural length scales where nodules appear in dark and the ferritic matrix in bright levels (Figure 2(c)).

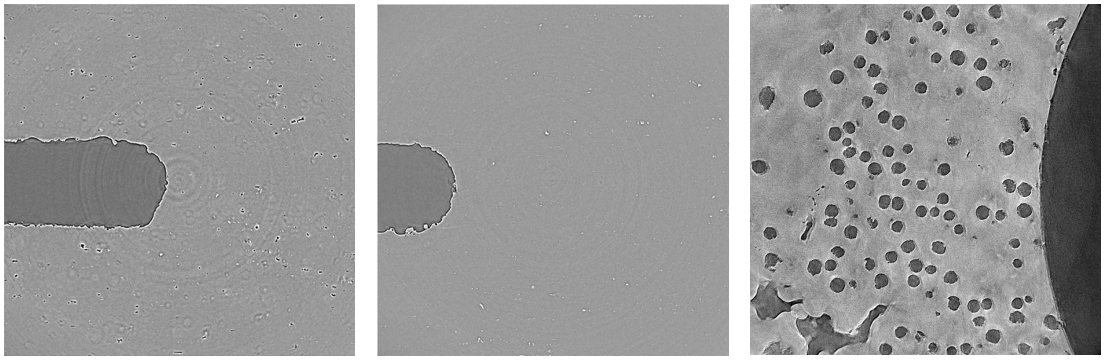

(a) AA2139 (b) AA2198 (c) GJS-400

Fig. 2 Mid-thickness section in 3D reconstructed volumes of two different aluminum alloys and one cast iron sample. The picture definition is 2040 × 2040 pixels for aluminum alloys and 1600 × 1600 for cast iron. The physical length of one voxel is 0.7 µm for aluminum alloys and 1.1 µm for cast iron. The ring artifacts from static features on the projection radiographs are visible (especially for sub-figures (a) and (b))

Nanotomography is nowadays accessible in synchrotron facilities and even lab tomographs thanks to various focussing devices of x-ray beams [237]. Resolutions as low as 20 nm can be achieved in synchrotron facilities [144]. This type of resolution requires very stable systems and very accurate actuation to allow for meaningful reconstructions. Nanolaminography was also shown to be feasible very recently at the European Synchrotron Radiation Facility [90].

Although tomography, because of its medical inheritance is mainly associated with the use of x-rays as the radiation source, the procedure *itself* is above all a technique of reconstruction of data acquired by the radiation-matter interaction where scattering is weak. It can therefore be adapted to many types of radiations as diverse as neutrons [224, 225], muons, electrons or gamma radiations [24, 173, 172, 174], visible optics, THz electromagnetic radiations, magnetic fields or ultrasound.

2.1.2 Magnetic Resonance Imaging

MRI is a noninvasive imaging technique that produces three dimensional images without the use of damaging radiation (*e.g.,* x-rays). It is often used for disease detection, diagnosis, and treatment monitoring [138]. Its principle consists of exciting and detecting the change in direction of the spins of magnetic atom nuclei, and in particular protons that are very convenient for imaging water in living tissues. Powerful magnets are utilized. They produce strong magnetic fields that force protons to align with them. When a radiofrequency current is then pulsed, the protons are stimulated and spin out of equilibrium, thereby "straining" them against the pull induced by the magnetic field. When the radiofrequency field is turned off, the sensors detect the energy released as the protons realign with the magnetic field. The time it takes for the protons to realign and the amount of released energy change depending on the environment and the chemical nature of the molecules.

Spatial encoding of the MRI signal is accomplished through the use of gradients in magnetic fields that cause atom spins in different locations to precess at slightly different rates. Phase tagging enables for another spatial encoding, thereby providing echo planar images (*i.e.,* one slice). As the protons undergo relaxation, the change in the local magnetic fields creates currents in the receive coils. These currents are detected as a change in voltage. The signal is then sampled, digitized, and finally stored for processing. It is broken down and spatially located to produce images.

Pixel sizes range in clinical MRI from mm to sub-mm. Voxel dimensions are given by the pixel size and the thickness of the slice (*i.e.,* measured along the magnetic field gradient). Slice thicknesses in clinical MRI vary from a maximum $\approx$ 5 mm, which is achieved using multislice imaging, to sub-mm with 3D scanning techniques. When using micro-MRI equipments, the voxel size can be decreased to typically 100 µm [14] but require extremely intense magnetic fields. The acquisition process associated with MRI is generally much longer than with (x-ray) tomography.

This is even longer when micro-MRI is performed (*e.g.,* 9 h for 512 × 256 × 256-voxel images with an isotropic voxel size of 78 µm, see Figure 3(a)). The trabecular network of cancellous bone revealed by micro-MRI was shown to be suitable for correlation purposes.

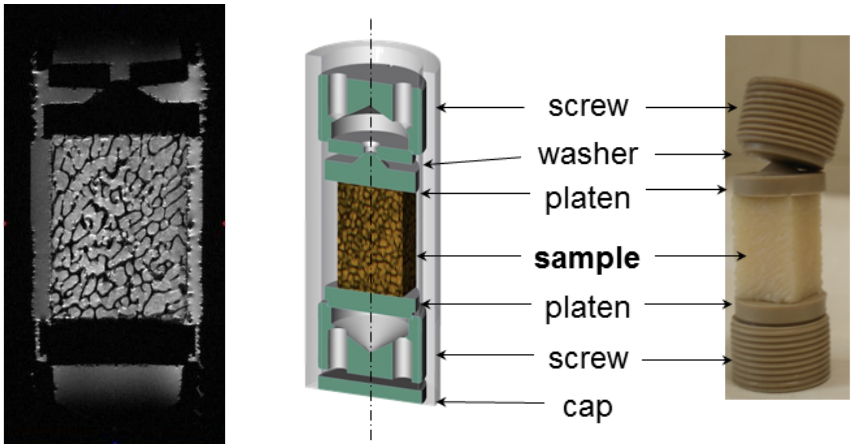

(a) (b)

Fig. 3 Compressive test monitored via micro-MRI [14]. (a) Frontal section of the reference configuration in which the sample and the loading device are shown. (b) Loading device for in-situ experiments

In any 3D imaging technique there are artifacts related to its operating principle [117]. One additional challenge in the medical field, which is not restricted to MRI, is associated with patient motion during the acquisition process. Registration techniques were developed in particular to tackle such issues [102].

2.1.3 Optical Coherence Tomography

Optical coherence tomography (or OCT) is a noninvasive imaging technique of optically semi transparent (*e.g.,* biological) materials at micrometer resolutions, *i.e.,* similar to that of optical microscopy. One of the most remarkable applications concerns ophthalmology. OCT is based on interferometry in so-called weakly coherent (*i.e.,* polychromatic or white) light. There are different variants of OCT, all of them typically use Michelson interferometers [182]. Full-field OCT utilizes

a Michelson interferometer with microscope lenses placed in both arms [13,54]. The length of the reference arm determines the inspected sample depth with equal optical length, and the amplitude of the coherent signal in both arms at a given location indicates the level of (single) backscattering. To extract the amplitude of the interference signal, interferometric images are acquired by means of a digital camera, and phase-shifted by the oscillation of the reference mirror. By computation, an image of the coherence volume is then obtained in real time (*i.e.,* at a typical rate of a few Hz). The illumination system uses a halogen lamp. Because of the very wide spectrum of the light source, interferences occur only for very small differential path length between both arms, thus limiting the thickness of the slice with a coherent backscattering, *i.e.,* the depth resolution. Typically, micrometer resolution can be achieved both in plane and perpendicular to it. Increasing the path length of the reference arm provides deeper and deeper images of the medium. Stacking those images produces a 3D volume of the (scattering) microstructure.

By construction, this technique is restricted to semi-transparent solids with low attenuation. The ability to image the inner structure for scattering media makes OCT very appealing for biological tissues. Figure 4 shows two such examples. In both cases, a 2D slice is shown with the observation face located at the top. The first example, Figure 4(a) is a porcine eye cornea, which constitutes a good model system for human eyes. For such a transparent medium, the technique is very well suited and the scattering is very weak (*i.e.,* inner structures are clearly revealed). The second example (human breast tissue) is more delicate to image because of attenuation and much more intense scattering. Inner micro-nodules (with about no scattering) are clearly seen. Yet, their shape is not enough to determine their nature. Elastography may help diagnose their possible carcinogenic character. One way to have access to such information is from imaging the same tissue under slightly different mechanical loadings. DVC is a technique of choice to provide the relative strains within the medium, and hence the sought elastic contrast [164].

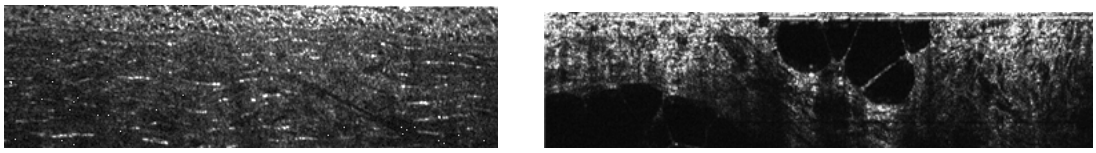

(a) (b)

Fig. 4 Section view through full-field OCT for two biological samples. The top of these images is the observation side. The width of these images is about 1 mm. (a) Porcine eye cornea revealing a lamellar collagen microstructure; (b) Human breast tissue where micro-nodules are visible. Both examples are taken from Ref. [164]

In terms of 3D imaging characteristics, OCT has some specificities. First, standard optics may require refraction corrections to be applied for curved objects [72]. This is important for a genuine rendering of the microstructure. Second, images are naturally noisy because of the low level of the coherent scattering signal as compared to the total light intensity, and because of the fast scanning through the depth (imposed for biological samples to avoid motion, viscous creep, or the mere time evolution of the living tissues). Further, because of multiple scattering or light absorption, images tend to display an artifactual gradient in the depth direction (*i.e.,* deeper is darker). The same effect is also responsible for a "shadowing" effect whereby a scatterer will be more or less visible depending on the medium along the optical path (this can be guessed to be responsible for the faint vertical columnar structure in Figure 4(b)). Similarly, noise also increases with depth. This effect can be accounted for in registration techniques (as discussed below in Section 3.1.2).

2.1.4 Other 3D imaging techniques

DVC was also applied to 3D images acquired with other modalities. Its feasibility was shown for volumes obtained by optical slicing (or scanning) tomography [77,78], optical rotating scanning tomography(ORST) [155], terahertz tomography [84], confocal microscopy [148], laser-scanning confocal microscopy (LSCM) [194], and ultrasonic imaging [24].

2.2 Ex-situ and in-situ experiments

The majority of in-situ experiments cited so far in this paper have been performed with x-ray imaging devices (*i.e.,* either in synchrotron facilities or lab tomographs even including medical scanners). Therefore, the two following sub-sections will deal with x-ray imaging. Some of the discussed features may also apply to in-situ experiments using other imaging modalities (*e.g.,* MRI [14]). However, they will not be reviewed hereafter. Conversely, MRI will prevent the use of magnetic materials in the design of the loading frame, as opposed to x-ray imaging, provided it does not intersect the beam. Figure 3(b) shows the mini-compression stage that was built from glass fiber reinforced PEEK (polyethyletherketone) to be MRI-compatible.

2.2.1 Ex-situ imaging

Ex-situ imaging is the easiest and most natural way of analyzing mechanical tests. It requires imaging to be performed at different loading steps. However, if some mechanical load is applied it has to be removed and it may change some of the studied phenomena (*e.g.,* cracks may close when damage is investigated). Conversely, permanent changes, such as plasticity or densification, do not significantly change upon unloading the sample. For some materials (*e.g.,* sand), the fact that the specimen was unloaded to be x-rayed ex-situ did not change the sought information (*e.g.,* density maps [41]) provided it is held in a constant hydrostatic confinement. Tomodensitometric measurements allowed Desrues *et al.* [50] to study the complex pattern of localization bands in the bulk of sand samples as early as in 1996.

In some other cases, the load is not necessarily of mechanical origin. For instance, cracking induced by accelerated desiccation of concrete-like material could be studied via ex-situ imaging even though the climatic chamber was located next to the beamline. In such cases, it is worth remembering that large rotations may occur because of repositioning issues [232] and consequently

consistent strain descriptors may be considered even though the strain levels themselves remain low [101]. This observation also applies to in-situ tests [14].

The following example is devoted to the analysis of accelerated desiccation [101]. The model material was made of 35 vol.% of glass beads (2 mm in diameter) included in a cement paste (cement CEM II/B 32,5R; water/cement ratio equal to 0.5). The analyzed sample was a cylinder (diameter: 8 mm, height: 20 mm) cored from a larger parallelepiped (volume: $40 \times 40 \times 160$ mm^3), which was cured in water at 20°C for 6 months. Prior to the initial scan, the specimen was preserved from desiccation. The sample was then dried for 23 hours at 60°C and scanned again. This ex-situ experiment was performed on beamline BM05 of the European Synchrotron Radiation Facility (ESRF, Grenoble, France) using a monochromatic beam with an energy of 30 keV. 900 radiographs were acquired at equally spaced angles between 0° and 180° using the FRELON CCD camera. The resulting radiographs, whose definition is 2048 × 2048 pixels, were used to reconstruct, via an in-house filtered back-projection algorithm [61], 3D images whose final voxel size is 10.2 μm.

DVC analyses were conducted with 4-noded tetrahedra (*i.e.,* T4-DVC [93]). The measurement mesh was adapted to the cylindrical geometry of the sample. The external radius of the region of interest is equal to 305 voxels, and the height is equal to 260 voxels (*i.e.,* the analyzed volume contains 76 million voxels). The advantage of such elements is that the actual geometry can be faithfully meshed with 19,494 T4 elements (Figure 5). The characteristic element size, which is defined as the cubic root of the average number of voxels per element, is equal to 16 voxels. The spatial displacement resolution, which is defined as the cubic root of the mean number of voxels considered for the nodal displacement measurement, is equal to 27 voxels.

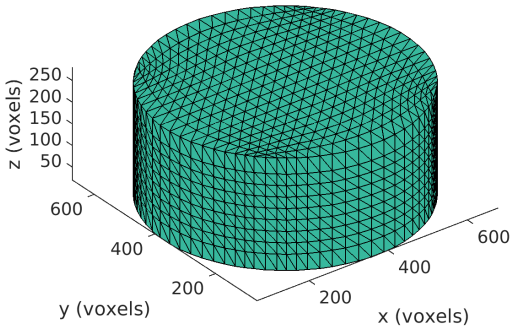

Fig. 5 Cylindrical region of interest and corresponding mesh of T4 elements.

A Matlab implementation was used to run the following analyses. Optimized C++ kernels [121] computed all the data needed to perform DVC. Binary MEX files were then generated and called in the Matlab environment. The DVC computation was run on a workstation with an 8-core Intel Xeon E5-2650v2 (2.6 GHz and 32 Go of memory). It took less than 2 minutes for the DVC code to converge (*i.e.,* the norm of displacement corrections is then 10^{-4} voxel). Figure 6(a) shows a 3D rendering of gray level residuals. The latter ones correspond to the gray level difference between the volume in the reference configuration and the volume of the deformed configuration, which was corrected by the measured displacement field. The high gray levels corresponded to the various cracks induced by accelerated desiccation. These residuals are very useful when checking the consistency of a DVC analysis. In the present case, the registration was successful except at the exact location of the cracks because displacement continuity was assumed. The only information left in the thresholded residuals was the cracks (Figure 6(b)). It was concluded that two damage mechanisms operate, namely, inclusion/matrix debonding and matrix cracking.

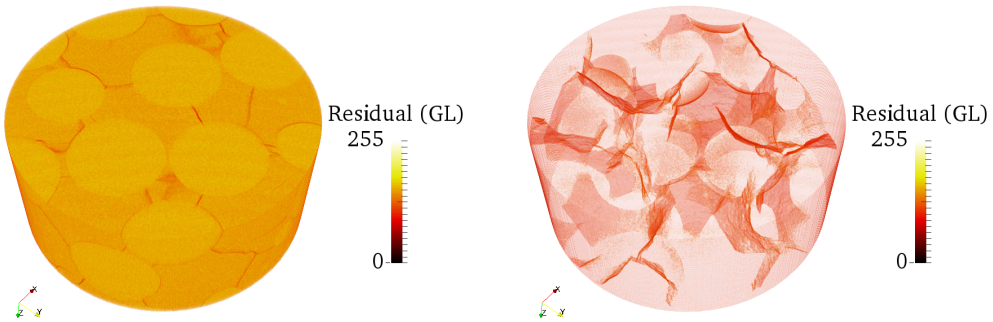

(a) (b)

Fig. 6 (a) 3D rendering of the gray level residuals. (b) Thresholded residuals highlighting the two damage mechanisms of the cementitious matrix reinforced by glass beads

2.2.2 In-situ tests

In the vast majority of cited works, in-situ experiments were conducted. In that case, the sample is imaged when the load is applied. This required for the design of specific testing machines. One key aspect is related to the fact that both tomography and laminography use a set of projections equally spaced, thus all angular positions should be accessible without any part of the testing machine obscuring the x-ray beam. This has led to the use of external tubes as frames of the testing machine [26]. In that case the whole testing machine is mounted on the turntable. Figure 7(a) shows one of the first in-situ testing machines that was used on beamline ID19 at the European Synchrotron Radiation Facility (ESRF) in Grenoble (France). It was used to study different damage mechanisms in the bulk of an Al/SiC composite [27].

More recently, commercial systems have been designed in which the testing machine allows the loaded sample to be rotated under load without using the turntable of the tomograph. One natural solution is to have *two* rotational actuators that allow torsion to be applied and to perform tomographic acquisitions, in addition to a longitudinal actuator (Figure 7(b)). Again, one

limitation is related to the minimum distance between the testing machine and the (divergent) x-ray source. Resolutions as low as ≈ 6 µm can be achieved in LMT's tomograph.

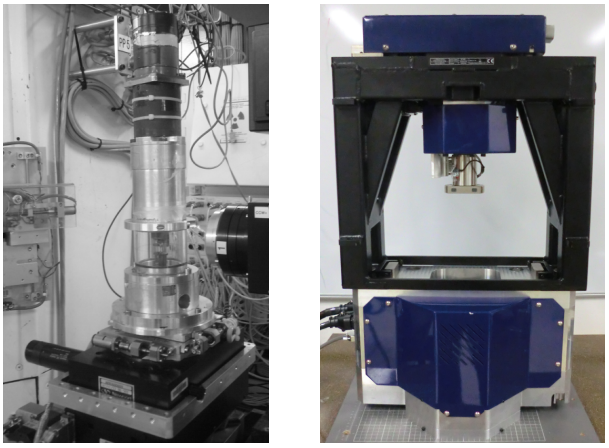

(a) (b)

Fig. 7 Example of testing machines for in-situ tests. (a) Tension/compression testing machine on a synchrotron beamline [27]. (b) Tension/torsion/compression testing machine for a lab tomograph

One way of validating such new testing machines is to check whether 3D reconstructions can be performed at full load capacity. Figure 8 shows a 3D rendering of an indentation test on two half-cylinders 35 mm in diameter made of granite when loaded at 20 kN. During the 360° rotation, the force had fluctuations less than 5 % the maximum level, which did not jeopardize the reconstruction. The quality of the latter was identical to that observed without any applied load for a physical voxel size of 20 µm. One scan lasted 1 h when 1,000 radiographs were acquired (beam tension: 210 kV, electron current: 100 µA). Cracks are observed in the lower half-cylinder.

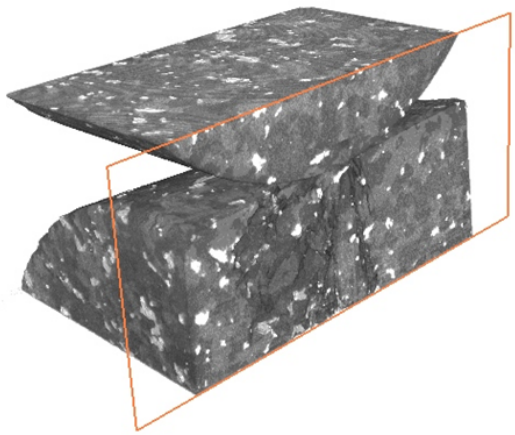

Fig. 8 3D rendering of indentation test on granite samples

Very recently, nanotomography was used to image mechanical tests in lab tomographs or synchrotron facilities. In particular, ex-situ [161] and in-situ [177] indentation tests were analyzed. For the last case, one key challenge was associated with the design of a nanomechanical test stage that could be integrated into x-ray nanotomographs.

As previously discussed, even though x-ray tomography is the most utilized 3D imaging procedure, it is also possible to image sheet-like samples via laminography. Consequently, the loading device becomes larger in comparison with tomography (Figure 7(a)). Figure 9(a) shows a testing machine that is fitted on the turntable to perform synchrotron laminography at the European Synchrotron Radiation Facility (ESRF) in Grenoble, France. The distance of the sample center point and the detector is ≈ 130 mm, which is compatible with micrometer resolutions thanks to the availability of parallel x-ray beams. In order to perform nanolaminography lightweight testing machines are needed (*i.e.,* the whole experimental setup weighs less than 50 g). It is was shown that good quality reconstructions were obtained for an in-situ tearing test when the physical size of one voxel was equal to 100 nm. The subsequent feasibility of DVC analyses was also proven. This study was crucial to understand the development of plasticity and damage in an aluminum alloy [28].

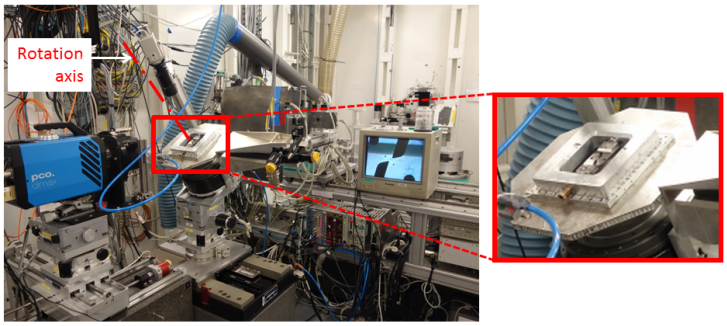

Fig. 9 Example of testing machine for in-situ tests in synchrotron laminography on beamline ID15 of ESRF. The zoomed section shows the testing stage. The central part of the sample is shown on the screen

With the development of in-situ tests, one challenge is related to the fact that most of the 3D imaging techniques mentioned above require acquisition times that are not compatible with uninterrupted experiments. At various stages of the test, the sample can still be loaded, provided it is motionless with respect to the turntable during the whole scanning duration. Such limitations are gradually pushed back via two complementary solutions to achieve time-resolved (or 4D) tomography [33, 65, 143, 178, 213]:

- On third generation synchrotron, the x-ray beams are very energetic and may even be "pink" (*i.e.,* with a finite band of wavelength to further intensify the beam, and thus tomography may not require very long exposure times). Consequently, the use of high speed digital cameras offers the possibility to perform *full* scans at frequencies as high as 20 Hz. To achieve such levels, the sample and its loading frame have to be spun continuously at high rotation speed, thereby possibly degrading the reconstruction quality when standard algorithms are used [143].
- Soft routes [213] can also be devised by combining DVC analyses and image reconstruction procedures. Under these conditions, the reference scan is performed when the sample is unloaded (or very modestly preloaded), and then radiographs are acquired on the fly without any inter-

ruption of the test [110]. In such situations, Projection-based DVC (P-DVC) is utilized [124]. The spirit of this technique will be presented in Section 5.6.

– Both previous cases may be combined to enable the tests to be run even faster without degrading the overall quality of the measured displacements and the reconstructed volumes.

3 From local to integrated DVC

To measure bulk displacement fields, there are two classes of registration techniques, namely, feature (or particle) tracking (which produces *sparse* sets of correspondences) and correlation procedures (which produce *dense* sets of correspondences). In the following, feature tracking (*e.g.,* see Refs. [217,116,216,62,146]) will not be reviewed. The discussion will focus on different variants of DVC in which mechanical information is gradually included.

In experimental fluid mechanics, a sister technique is referred to as tomographic particle image velocimetry (or tomo-PIV) when dealing with the measurement of 3D velocity fields via correlation techniques [57,203]. In the medical field (and applied mathematics), such technique is called "image registration" and appeared earlier [228,141,102] than in experimental mechanics [12,207]. One reason of this delay may come from the needed resolution for the technique to be useful, which varies with the field of application. In medical imaging an uncertainty of about one voxel is generally considered as acceptable, whereas in mechanical testing, at least some 10^{-1} voxel-size uncertainty on displacements (or better) is needed to estimate meaningfully commonly encountered strains. This difference in ambition for medical applications, materials science or mechanics of materials may thus have required a technique that had matured within the domain of medical imaging confronted with other issues than accuracy. However, it is also noteworthy that cross-references are scarce, so that it is also plausible that these techniques emerged independently and progressed with their own specificities as called for by applications.

It is also interesting to note that the same distinction has been made in both fields between so-called local and global approaches [228, 197]. Local approaches to DVC [12, 207] consist of dividing the region of interest into small volumes (hereafter referred to as subvolumes). The registration is performed independently on each subvolume. Conversely, in global approaches [228, 197] the registration is performed over the *whole* region of interest (ROI).

3.1 Overall presentation of DVC

The two 3D images to be registered are denoted as $f(\boldsymbol{x})$ (assumed here to be the "reference" image) and $g(\boldsymbol{x})$ (the "deformed" image), where f and g are scalar gray levels at each voxel location $\boldsymbol{x}$. Fundamentally, DVC rests on the basic assumption that upon a mere change in the position of voxels, defined by a displacement field $\boldsymbol{u}(\boldsymbol{x})$, the two images can be brought to perfect coincidence such that

$$g(\boldsymbol{x} + \boldsymbol{u}(\boldsymbol{x})) = f(\boldsymbol{x}) \tag{1}$$

Although this equation appears as trivial, a number of common issues can be mentioned that motivated different variants in the past:

1. Images are strictly defined only at integer voxel positions. However, in practice $\boldsymbol{u}$ may assume arbitrary values, and hence it is essential (and this becomes really critical when subvoxel resolutions are aimed for) to provide an estimate of the gray level at an arbitrary position.
2. Images are naturally discrete, not only from the voxel structure, but also from the encoding of gray levels. This argument is not very stringent for computed tomography where gray levels are computed, and hence the gray level discretization of the starting images (radiographs) is largely erased. However, in other cases, or when the contrast is poor, a modest gray level dynamic range may reveal limiting.
3. Images are noisy. Even when no motion is expected between two images of the same scene acquired consecutively and with the same device, *i.e.,* $\boldsymbol{u}(\boldsymbol{x}) = \boldsymbol{0}$, f and g are different. Their

difference $\eta(\boldsymbol{x}) \equiv g(\boldsymbol{x}) - f(\boldsymbol{x})$ is at best (*i.e.,* excluding the case of spurious changes of intensity or motion) the sum of the noise affecting g (often assumed to be statistically similar to that of f) and $-f$.

These three items imply that Equation (1) even with the exact displacement is not strictly satisfied. In fact interpolation and discretization errors are both expected to be of zero mean, and hence they can be included in what is called (effective) noise. Thus, rather than trying to exploit the above identity voxel-wise, it is important to assess how good (or bad!) the registration is. In fact the natural answer is the following: assuming that the exact answer for $\boldsymbol{u}$ is known, how credible is it to measure locally a gray level f on one voxel, and to estimate (via interpolation) $\widetilde{g}_{\boldsymbol{u}}$ at the same position, after displacement correction

$$\widetilde{g}_{\boldsymbol{u}}(\boldsymbol{x}) = g(\boldsymbol{x} + \boldsymbol{u}(\boldsymbol{x})) \tag{2}$$

This is assessed with a suited *similarity measure* $S(f, \widetilde{g}_{\boldsymbol{u}})$. For any displacement field $\boldsymbol{u}$, one may construct a corrected image $\widetilde{g}_{\boldsymbol{u}}$, and thus a cost function (see Section 3.1.2)

$$\mathfrak{T}_{\mathrm{DVC}}[\boldsymbol{u}] = S(f, \widetilde{g}_{\boldsymbol{u}}) \tag{3}$$

The solution of DVC is given by the displacement field, *i.e.,* the argument that minimizes the above cost function. This can be seen as defining a tolerance to the deviation between the above estimates. f and $\widetilde{g}_{\boldsymbol{u}}$ are allowed to differ by a gray level difference that is compatible with what is known from the noise statistical characteristics. It is also noteworthy that when noise has a specific spatial correlation this similarity measure is *intrinsically* nonlocal. This is also the reason why after a DVC analysis, it is very important to examine carefully the so-called *residual field*

$$\rho(\boldsymbol{x}) = \widetilde{g}_{\boldsymbol{u}}(\boldsymbol{x}) - f(\boldsymbol{x}) \ , \tag{4}$$

because even if overall characteristics such as the global variance may be compatible with noise, faint correlations can be easily visualized and detected to signal a violation of the DVC hypotheses

(to be interpreted as being acceptable or requiring an enhanced model). In order to ease notations in the following, the subscript to $\widetilde{g}$ will be omitted.

Considering that Equation (1) is now endowed with some tolerance, the determination of the displacement field $\boldsymbol{u}(\boldsymbol{x})$ is an ill-posed problem. This constitutes the major difficulty of DVC. In order to make the problem well-posed, constraints are to be added to the displacement field, $\boldsymbol{u}$. Namely, rather than leaving the displacement vectors free to vary arbitrarily from one voxel to its neighbors, displacements may be sought in a restricted space, $\mathcal{U}$, and it is only within this space that the image similarity is to be optimized. Specifying some of these spaces will naturally lead us to distinguish local and global approaches. Restriction to a subspace of displacement field can be interpreted as a (strong) regularization, and tuning the dimensionality of this subspace will allow the conditioning of the problem to be adjusted, and in turn the robustness of the displacement field measurement with respect to noise.

Another route for making the problem well-posed, is to opt for a weak regularization. This approach consists of introducing two displacement spaces $\mathcal{U}_1 \subset \mathcal{U}_2$, such that the displacement field is allowed to explore the space with a higher dimensionality, $\mathcal{U}_2$, although the more restricted space $\mathcal{U}_1$ is expected to be more likely. To express this choice, another functional for the trial displacement field $\mathfrak{T}_{\text{Reg}}[\boldsymbol{u}]$ is introduced, which is a penalty given to the candidate $\boldsymbol{u}$ when it does not belong to the preferred subspace. This penalty is usually chosen as a function of the distance between $\boldsymbol{u}$ and its projection $\mathit{\Pi}_1[\boldsymbol{u}]$ onto $\mathcal{U}_1$

$$\mathfrak{T}_{\text{Reg}}[\boldsymbol{u}] = \varphi\left(\|\boldsymbol{u} - \mathit{\Pi}_1[\boldsymbol{u}]\|\right) \tag{5}$$

Tikhonov regularization [215] is such a weak regularization. For DVC, it will be shown that some specific forms of regularization are very well suited, thereby allowing for a smooth continuation of DVC to mechanical identification of a constitutive behavior.

It is important to note that such a regularization may be considered from different standpoints. If some information about the mechanical behavior is known, it is natural to use it in the above

term, and a large weight is adequate. However, when the constitutive law is unknown, the above regularization may be seen as selecting the equivalent of "shape functions." Hence the subspace $\mathcal{U}_1$ is to be compared with that obtained from, say, a finite element discretization. This may be convenient, even if it is not meant to be realistic at the scale of elements. In the following, it will be shown that $\mathcal{U}_1$ may be the kernel of a differential operator, meaning that locally the shape function obeys a specific differential equation. Interestingly, depending on how much the regularization is trusted, from a neutral shape function generator up to a reliable mechanical description, one may continuously tune the weight of the above functional.

Last, it is natural to wonder about the possibility of being misled by the "nice-looking" aspects of the obtained solution, by the use of regularization. For this reason, the following presentation will emphasize the use of gray level residual fields that measure very accurately (*i.e.,* voxelwise) the relevance of the proposed solution. Hence if a regularization property is forced illegitimately on the displacement field, then the residual field will very clearly show that the proposed solution is not suitable. One cannot overemphasize the usefulness of such residuals.

3.1.1 Gray level interpolation

The question of gray-level interpolation is not specific to 3D images, and for Digital Image Correlation, with 2D images, this question has been very thoroughly studied [212]. Because pixels and voxels can be seen as integrating a fine scale information over an elementary square or cube, it is natural to consider the gray level as resulting from a convolution of an intrinsic fine scale texture by an elementary d-dimensional rectangular window function $w(\boldsymbol{x})$ (valued one if the absolute value of all coordinates are less than 1/2, and 0 otherwise). Such a function enhances the regularity of the original signal.

For instance, starting from discrete spikes (*i.e.,* Dirac comb) centered at voxel centers, this convolution provides a piecewise (*i.e.,* voxelwise) constant function. Starting from a voxelwise

constant function, its convolution would be a continuous one, piecewise linear along lines parallel to axes. More generally, if the original fine scale texture is $\boldsymbol{C}^n$ (derivatives up to order n exist and are continuous), its convolution by $w(\boldsymbol{x})$ is $\boldsymbol{C}^{n+1}$. Exploitation of this line of thought has led to the powerful concept of *spline functions*, that provide an elegant way of generating an interpolation function with a prescribed position at integer coordinates, with a tunable smoothness [205]. Cubic splines are very popular, because of their good trade-off between smoothness (resulting interpolation is $\boldsymbol{C}^2$) and compact support leading to efficient implementations. The limit of an infinite order spline interpolation is an interesting and appealing object as it produces a $\boldsymbol{C}^\infty$ interpolation function. It can be shown theoretically that this coincides with the convolution with a cardinal sine function, and hence it would match precisely what is implicitly performed with a Fourier transform (where translation is obtained by simple phase shift on the Fourier transform [36]).

It is unfortunately difficult to go much further from the theoretical side, as the starting point is the fine scale reality that is unknown. From experience, a piecewise linear interpolation (which is a first order spline interpolation), is cheap and easy but does not lead to a high fidelity. Cubic (and even quintic) splines have been observed to be a better approximation (leading to smaller interpolation errors and uncertainties) [212, 186].

It may be observed that before achieving perfect registration, using a poorer but faster interpolation procedure may provide an easily accessible acceleration at no implementation cost. Once a reasonable registration has been achieved, then very few additional iterations using the best available interpolation procedure will provide the desired final hundredths of voxel corrections.

3.1.2 Similarity measures

It was earlier mentioned that different similarity measures have been proposed to assess registration. That is for each voxel, $\boldsymbol{x}$, the reference gray level $f(\boldsymbol{x})$ and that of the deformed image corrected by a trial displacement field $\widetilde{g}(\boldsymbol{x})$ are to be compared. As earlier stated, their difference

is at least (that is when the trial displacement field is the exact solution) equal to the sum of the noise affecting each image. Thus the similarity measure implicitly involves a noise model.

The most common model is white Gaussian noise, which states that the probability distribution function for the noise η is

$$p(\eta) = \frac{1}{\sqrt{2\pi}\sigma} \exp\left(-\frac{\eta^2}{2\sigma^2}\right) \tag{6}$$

where σ is the standard deviation. Generally, a displacement field is not to be judged based on a single voxel prediction, but rather over a zone of interest, $\mathcal{Z}$. The "whiteness" of noise means that it is uncorrelated from one voxel to any other one. As a result, the probability of observing a residual field $\rho(\boldsymbol{x}) = \widetilde{g}(\boldsymbol{x}) - f(\boldsymbol{x})$ is

$$\begin{aligned} P[\rho] &= \prod_{\boldsymbol{x}\in\mathcal{Z}} p(\rho(\boldsymbol{x})) \\ &\propto \exp\left(-\frac{1}{2\sigma^2} \sum_{\boldsymbol{x}\in\mathcal{Z}} \rho(\boldsymbol{x})^2\right) \end{aligned} \tag{7}$$

Assuming that the noise variance is identical for all voxels, maximizing the likelihood $P[\rho]$ for the residual field, is equivalent to minimizing its cologarithm, and hence, a natural similarity measure appears

$$S_{\mathrm{SSD}}[\rho] = \sum_{\boldsymbol{x}\in\mathcal{Z}} \rho(\boldsymbol{x})^2 \tag{8}$$

where it is recalled that $\rho(\boldsymbol{x}) = g(\boldsymbol{x} + \boldsymbol{u}(\boldsymbol{x})) - f(\boldsymbol{x})$. This first measure is the sum of squared differences that is postulated as an appropriate similarity measure [197,171]. This observation calls for some comments:

- First, there is no reason to *postulate* an expression for S. It has to result from the properties of noise. In the case of *uniform*, *Gaussian* and *white* noise, the most appropriate measure is the sum of squared differences.
- All the above qualifiers (uniform, white, Gaussian) are essential. Any violation of the above would call for a modified measure.

– Let us consider full-field OCT as a practical case. The 3D image consists of a stack of 2D images that correspond to the scatterers assumed to be dilute in a semi-transparent medium. Thus for each slice at a constant depth, a uniform white Gaussian model is a fair approximation (which can easily be checked). However, as depth increases the noise amplitude increases. This is partly due to the ambient scattering produced by the medium, which limits the signal amplitude (however, the same bias affects both the reference and the deformed image, and hence its correction is not essential as long as the displacement does not involve very large depth z variations). The depth z also affects the noise amplitude that is expected to grow with it. However, it is quite easy to measure the noise variance as a function of depth, $\sigma^2(z)$. From the later, a modified criterion results

$$S_{\mathrm{OCT}}[\rho] = \sum_{\boldsymbol{x}\in\mathcal{Z}} \frac{\rho(\boldsymbol{x})^2}{\sigma(z)^2} \tag{9}$$

where the fact that the residual involves two images should have led to doubling the variance, but because a constant multiplicative factor in S plays no role, it has been discarded from the above expression.

– Often, as is the case for optics, the noise variance is a function of the gray level intensity itself. The brighter a voxel, the higher its absolute noise level, and as the noise amplitude grows sub-linearly with the intensity, its relative noise level decreases with the intensity. This is true for any Poisson (or shot) noise where $\sigma(f) = \varsigma\sqrt{f}$. However, as the number of "counts" increases, the distribution can be well accounted for by a Gaussian distribution. Moreover, a white noise assumption can still be valid, and hence only uniformity is to be questioned. In such cases, it is straightforward to extend the previous analysis to obtain

$$S_{\mathrm{Poisson}}[\rho] = \sum_{\boldsymbol{x}\in\mathcal{Z}} \frac{\rho(\boldsymbol{x})^2}{f(\boldsymbol{x})} \tag{10}$$

As above the constant factor of $1/(4\varsigma^2)$ has been omitted. In such cases, as noted in Ref. [211], taking the Anscombe transform of the original gray levels [145] or more simply, taking the

square root of gray levels, $\hat{f} = \sqrt{f}$, restores a constant variance noise affecting $\hat{f}$. Hence it suffices to register $\sqrt{g}$ onto $\sqrt{f}$, using S_{SSD}, as an appropriate similarity measure

$$S_{\text{Anscombe}}[\rho] = \sum_{\boldsymbol{x}\in\mathcal{Z}} \left(\sqrt{g(\boldsymbol{x}+\boldsymbol{u}(\boldsymbol{x}))} - \sqrt{f(\boldsymbol{x})}\right)^2 \tag{11}$$

Note however that this transformation relies on the fact that a zero gray level ($f = 0$) means that the light intensity is 0, and hence an offset in gray levels, which is commonly used without questioning its relevance, is *not allowed* without taking it into account in the above expression.

– If the noise is uniform and Gaussian but not white, one should measure its covariance

$$\text{Cov}(\boldsymbol{y}) = \langle \eta(\boldsymbol{x}+\boldsymbol{y})\eta(\boldsymbol{x})\rangle_{\boldsymbol{x}} \tag{12}$$

where the dependence only on $\boldsymbol{y}$ results from the assumed statistical stationarity. The inverse covariance is a metric kernel $A(\boldsymbol{y})$, defining the so-called Mahalanobis distance [140]. It is conveniently computed from its Fourier transform that is equal to the inverse of the Fourier transform of $\text{Cov}(\boldsymbol{y})$. If $\mathfrak{F}$ designates the Fourier transform and $\mathfrak{F}^{-1}$ its inverse, then

$$A(\boldsymbol{x}) = \mathfrak{F}^{-1}\left(\frac{1}{\mathfrak{F}(\text{Cov}(\boldsymbol{x}))}\right) \tag{13}$$

From this metric, the (Mahalanobis) similarity measure writes

$$S_{\text{Mahalanobis}}[\rho] = \sum_{\boldsymbol{x}\in\mathcal{Z}}\sum_{\boldsymbol{y}\in\mathcal{Z}} \rho(\boldsymbol{y})A(\boldsymbol{y}-\boldsymbol{x})\rho(\boldsymbol{x}) \tag{14}$$

When the covariance is purely local (*i.e.,* at the voxel level), it is to be noted that this formula coincides exactly with S_{SSD}. As for the Anscombe transform, there exists a filter H, such that the mere quadratic difference of $\hat{f} = H \star f$ and $\hat{g}(\boldsymbol{x}) = [H \star g](\boldsymbol{x}+\boldsymbol{u}(\boldsymbol{x}))$ coincides with $S_{\text{Mahalanobis}}[\rho]$. In Fourier space, this filter is the square root of $\mathfrak{F}(H) = \mathfrak{F}(A)^{1/2}$.

– Finally, let us consider the case when the noise is uniform, white, but not Gaussian. In this case, it is characterized by a nontrivial probability density function (p.d.f.), $p(\eta)$. Following the above derivation, it is observed that the absence of correlation implies that probabilities

can be multiplied, and hence their logarithm summed, thereby providing a similarity measure that is still proportional to the log-likelihood, or up to a change of sign to comply with the above Gaussian case, the similarity measure to be minimized reads

$$S_{nG}[\rho] = -\sum_{\boldsymbol{x}\in\mathcal{Z}} \log(p(\rho(\boldsymbol{x}))) \tag{15}$$

A simple and useful application of the above result consists of having the superposition of two Gaussian noises. In particular, one can be a low probability one but with a broad variance, akin to "salt and pepper noise". In such cases, the $-\log(\rho)$ function is no longer a mere parabola, but for large arguments it may open up to a cone (if one wants to preserve convexity, a very useful property here) or flatten out to a constant asymptote.

Let us emphasize that the above expressions are all derived from *measurable* properties from the noise, and no free parameters are to be tuned.

Yet, the list of popular similarity measures is far from being exhausted. For instance, cross-correlation is frequently chosen since the early developments of DVC [12,212]. Let us first note that if the zone of interest is large, and if the displacement is uniform over the zone, the (normalized) cross-correlation function of f and g coincides, up to a translation, with the auto-correlation function of the reference zone of interest, but reaches its maximum at a position that is equal to the displacement between the two zones. Moreover, the cross-correlation function is easily obtained in Fourier space as $\mathfrak{F}^{-1}\left[\mathfrak{F}[f]\overline{\mathfrak{F}[g]}\right]$. Thus, it offers the possibility of exploring all potential displacements simultaneously and this for a modest cost using fast Fourier transforms [42]. Finally, using a subvoxel interpolation of the cross-correlation, very precise localization of the maximum can be achieved, which is implicitly based on a $\boldsymbol{C}^{\infty}$ interpolation of both images. Those properties made the success of Particle Image Velocimetry (PIV) in the early days [2] during which robust and fast methods that could be implemented easily were sought, and this technique was a well suited answer to these needs.

However, it is to be stressed that raw fast Fourier transform algorithms assume spatial periodicity of the functions to be transformed. Thus if the two zones for f and g do not coincide, the cross-correlation function (be it computed with FFT or not) takes into account non overlapping edges and hence is not a satisfactory measure. This can be corrected by progressively clipping the zone in the deformed image to the predetermined displacement, but the iterative scheme reduces drastically the attractiveness of this similarity criterion. This correction consists of computing the cross-correlation between f and $\widetilde{g}$ rather than f and g

$$\begin{aligned} S_{\mathrm{CC}}[\rho] &= \sum_{\boldsymbol{x}\in\mathcal{Z}} (\widetilde{g}(\boldsymbol{x}) - \langle\widetilde{g}\rangle)(f(\boldsymbol{x}) - \langle f\rangle) \\ &= (1/2)\sum_{\boldsymbol{x}\in\mathcal{Z}} (\widetilde{g}(\boldsymbol{x}) - f(\boldsymbol{x}))^2 \\ &\quad -(1/2)\sum_{\boldsymbol{x}\in\mathcal{Z}} [\langle\widetilde{g}^2\rangle - 2\langle\widetilde{g}\rangle\langle f\rangle + \langle f^2\rangle] \end{aligned} \tag{16}$$

The last term in the sum does not vary with the displacement iff the statistical sampling of the gray values allows $\langle\widetilde{g}^2\rangle$ and $\langle\widetilde{g}\rangle$ not to vary much when the zone of interest is moved. In this case, the cross-correlation function coincides with the quadratic difference.

Second, and more importantly, there is no way to deal efficiently with a displacement field that is not a pure and uniform translation. Even a rigid rotation cannot be represented simply in Fourier space. Additionally, the computation load for estimating $\widetilde{g}$ is much greater than computing the above quadratic difference and its gradients.

It is often mentioned that the cross-correlation criterion to be maximized is independent of a possible affine transformation of gray level that would affect g but not f. This is true, however, it is odd to express such a demand at this stage. What is meant here is that the starting point, Equation (1), is not satisfied and should rather be written as

$$g(\boldsymbol{x} + \boldsymbol{u}(\boldsymbol{x})) = (1 + a)f(\boldsymbol{x}) + b \tag{17}$$

where the brightness b and contrast a corrections have been written so that the previous case coincides with $a = b = 0$. It is noteworthy that if no information is available on a and b, it

may be seen as saying that a and b are part of the noise, but they have some specificities. For instance if they have known spatial correlations (say long wavelengths only), the above similarity measure $S_{\text{Mahalanobis}}$, will lead to cancel brightness and contrast modulations over large distances by a moving average filter (*i.e.,* removing the effect of a and b fields), and this will be done automatically without having to formulate the appropriate filter "manually." The limit case of having a spatially constant a and b is obtained by taking care of the appropriate limit (the direct covariance function becomes somewhat undefined).

Alternatively, it is possible to consider a and b in a similar fashion as $\boldsymbol{u}$, as unknown parameters to be determined to register at best the two images. This can be formulated easily as a natural extension of the optimization of the similarity measure, leading to the joint determination of the gray level transformation and of the displacement simultaneously [100]. One may also consider a sequential determination, searching first for a and b at fixed displacement, and then for $\boldsymbol{u}$ using the predetermined gray level corrections for $\widetilde{g}$, and iterating these two steps up to convergence. With this formulation, it is straightforward to notice that a and b are given by a mere linear regression, which consists of matching the mean value and the standard deviation of f and $\widetilde{g}$, which is precisely what is obtained treating a and b as noise. However, let us insist on the fact that once again, after having written Equation (17) properly, and chosen to treat a and b either as noise or as unknowns, the appropriate similarity measure is naturally generated and leads to the solution. Without much surprise, the same solution emerges whatever the choice is made for the status of a and b.

Let us also note that Equation (17) may mean that the same parameters a and b hold for the entire image. This is not at all equivalent to treating the problem with a partition into zones, for each of whom a and b are determined anew. The latter problem introduces much more unknowns than the former, and hence the uncertainty attached to the determination of the displacement (and gray level corrections) is much higher (especially for small subvolume or element sizes, see

Section 4). It may be desirable to introduce some flexibility in the gray level corrections, but in this case again, the best way to proceed is to introduce a parameterization of the way a and b may vary in space.

In cases where two images may be related by more complex contrast corrections, other statistical measures have been introduced. The so-called mutual information [209,199], $I(f,\widetilde{g})$, checks for the existence of a well defined value of $\widetilde{g}$ knowing f without having to specify explicitly the relation between the two. More precisely, the mutual information is defined as

$$I(f,\widetilde{g}) = \sum_{f,\widetilde{g}} P(f,\widetilde{g}) \log\left(\frac{P(f,\widetilde{g})}{P(f)P(\widetilde{g})}\right) \tag{18}$$

where $P(f,g)$ is the joint distribution function. If f and $\widetilde{g}$ were unrelated then their joint distribution would be equal to the product $P(f)P(\widetilde{g})$, and their mutual information would be 0. The mutual information measures the "entropy reduction" brought by the knowledge of one of the two gray levels, say f, when considering the other one. It is more transparent when noting that the argument of the log function is nothing but the ratio of the conditional probability distribution, $P(\widetilde{g}|f) = P(f,\widetilde{g})/P(f)$ and the probability of $\widetilde{g}$, $P(\widetilde{g})$ without the knowledge of f. Interestingly, when the joint distribution of f and $\widetilde{g}$ (assuming displacement corrections have converged) is Gaussian, it has been shown that the mutual information reduces to a function of the normalized covariance, $\log(1 - \mathrm{Cov}^2)$ [118]. Thus when one quantity would be Gaussian and related to the other one by an affine relationship, the mutual information criterion reduces to *maximizing* the covariance or the cross-correlation.

The freedom of being able to deal with an arbitrarily complex (*i.e.,* nonlinear) relationship has however a large cost related to sampling issues. In order to faithfully infer a joint distribution function, a large sample size is needed and thus a local approach is inappropriate because of the small number of voxels involved. In addition, a purely local approach would allow the nonlinear relationship relating f and $\widetilde{g}$ to differ from one zone to another, thereby further relaxing the registration constraints. Another difficulty is that gray levels are subjected to noise, and hence

they should rather be defined as an interval of width σ (or rather a probability distribution function (pdf) having a standard deviation σ). This is essential to compare two gray levels that are supposed to be identical. One may wonder where this key parameter appears, since this is usually not made explicit. In fact the statistical entropy measure involves a probability distribution that is defined numerically with a particular binning, that should have a width σ. The strong dependence of the entropy on this binning (or discretization) is very seldom discussed. This is a fragility of this criterion, together with the fact that locally all spatial correlation is lost (voxels may be shuffled spatially without consequence on the resulting entropy).

A second weakness is the lack of "distance" or progressiveness in the joint distribution function. When $\widetilde{g}$ differs from most other gray levels in voxels having the same f value, the difference $\widetilde{g} - \langle g(f) \rangle$ does not come into play, and hence no difference is made between a small or a large violation of a potential $g(f)$ relationship. This in turn implies a lack of convexity of the similarity measure, and the numerical difficulties resulting thereof, that is lack of uniqueness, and the solution possibly depends on the type of minimization algorithm (and on possible convergence parameters when required). Finally, it is to be stressed that cases where an arbitrary complex relationship between f and $\widetilde{g}$ are not very frequent to say the least. When it is needed to take into account such complex correspondence, one may simply parameterize this relationship (*e.g.,* stating that $g(f)$ be a polynomial or any other nonlinear functional form) and identify the required parameters with the least variability that is needed (*e.g.,* not estimating a different polynomial for each zone when a local approach is used).

3.1.3 Inter-modality registration

Among the few cases when such nonlinear correspondence may be useful, is when a different modality (and hence a different contrast) is used for f and g and still one would like to register the two images. One such example was studied in details [225], where x-ray and neutron tomographic

images of the same sandstone sample were captured, and a common referential was sought to fully benefit from both modalities and their resulting contrast. The presence of elements that display different contrasts with only one modality forbids the use of parametric relationships, yet it is possible to design a learning scheme that is a simple extension of standard DVC, and that leads to registration and simultaneously allows the different phases to be naturally segmented.

Plain x-ray tomography as such delivers a scalar field (*i.e.,* x-ray absorption) that is relative to a specific energy for monochromatic sources as is usually the case in synchrotron beamlines, or to an energy spectrum for lab µCT scanners. This provides a very rich information in terms of 3D spatial resolution. Yet, in some cases, it is difficult to discriminate between different phases. Thus, very early on, the idea of combining different modalities has emerged. The main motivation came from the field of medical imaging where the patient motion has always been a difficult obstacle to overpass. Thus a secondary modality that could detect the phase of breathing or cardiac rhythm allows radiographs to be acquired in situations close to steadiness in spite of uninterrupted motions [228]. Such a case however involves a rather poor usage of the secondary acquisition device.

However, still in the field of medical imaging, it was realized that two 3D-imaging modalities could be combined to get a richer information, as the physical origin of contrast in the two modalities could differ [141]. In order to achieve full benefit from these modalities, it is essential to be able to express them in the same reference frame. This automatically calls for image registration as a powerful tool to put the two images in coincidence. However, for the very purpose of using different contrasts, not to mention different resolutions or different acquisition times that could induce slight distortions between the two modalities, it is difficult to define what a good matching is. Reference [102] provides a review of early registration techniques that were used on the turn of the century.

In the field of materials science, dealing with different modalities has the potential of revealing chemical contrast. For instance dual source x-ray tomography with a simultaneous acquisition of the two perpendicular beams set at two different energies provide two 3D images with different contrasts [67,113,180]. Yet, in that case, the two volumes are expected not to be very different, and registration may not be extremely challenging. The association of x-ray and neutrons but bring out much more salient differences [6].

Specific features or markers that have a well defined signature in both modalities were first a privileged way to find a common reference frame. This technique however refers to marker tracking rather than DVC. It is fair to note that when a simple mapping is sought (*i.e.,* translation, rotation and scale factor) and when there is no need for very accurate registration, this marker tracking technique offers a simple solution. However, the definition and selection of the appropriate markers are essentially manual and hence registration requires a significant and incompressible time. Additionally, this technique cannot be considered as optimal in terms of an abstract consideration of the usage of information that is present in the images as only a small fraction of the image is used.

It is worth noting that DVC (or DIC for 2D images) strictly speaking cannot be used as the conservation of brightness, which lies at the very heart of the method, does not hold. Hence a much more general similarity measure is to be used (see Section 3.1.2). If no more than two phases are considered an affine transform of gray levels is sufficient, and hence a standard DVC algorithm allowing brightness and contrast changes, enables a proper registration to be achieved. Care should be taken to perform the gross gray level correction early enough to be consistent with a correction scheme based on small perturbations. In more general cases, however, correspondence between the two images has to phrased in more general terms. Even a nonlinear relationship between the gray levels of the two modalities may be inadequate, as the same gray level of one modality may be expressed as different gray values in the other modality.

It is for these registrations that a similarity measure based on mutual information is suited [236, 139]. Mutual information is one choice out of many comparable measures based on joint histograms, called f-information or f-divergence [226]. As earlier mentioned, the joint histogram does not take into account the spatial correlation in the images and depends on the chosen binning of the histogram.

Introducing a similarity measure that is a function of the pair of gray levels on the registered images, $\Phi(f(\boldsymbol{x}), \widetilde{g}(\boldsymbol{x}))^2$, rather than the mere quadratic difference as used earlier, allows one to come up with a generalized formulation of DVC. A Bayesian framework provides an interpretation of the joint distribution and in agreement with the noise interpretation of the quadratic difference that was presented earlier, the Φ^2 function can be chosen as the cologarithm of the joint histogram. In Ref. [225], it was shown that the analytical formulation of the Newton's descent minimization algorithm assumes a form that is a natural extension of the incremental correction, see Equation (24). Moreover, if Φ^2 is adjusted from a previous determination of the registration, such an approach can be seen as a learning scheme of the suited potential to be minimized. Such an approach was shown to be successful for x-neutron tomography registration that was performed for a Bentheim sandstone with a rather similar resolution [225]. Figure 10 shows two complementary composite checkerboard images made of squares extracted from one modality or the other after registration. It is seen that some morphologic features (crack or boundary) are visible in both modalities and show an excellent continuity. Conversely, other features such as the large white inclusion show a large attenuation with neutron imaging but appears as almost invisible with the x-ray modality.

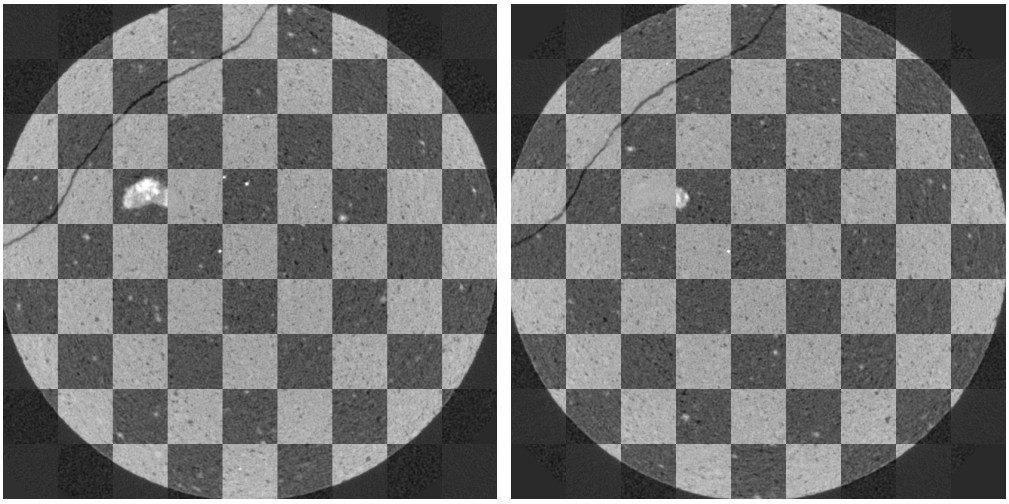

(a) (b)

Fig. 10 Complementary mosaic images showing alternating square patches cut out of the two tomographic modalities (x-ray or neutrons) after registration. It is observed that some features (boundary, crack) show an excellent continuity, whereas other features exhibit a very different contrast.

3.2 Kinematic basis

Let us now discuss the choice of the kinematic basis. As mentioned earlier, the choice of the space $\mathcal{U}$ the displacement field belongs to is the key to provide a regularization and to make the problem well-posed. Therefore a well suited choice will help convergence to a satisfactory measurement result and above all it will yield small uncertainty levels [23, 196, 191, 149, 150]. Conversely, if not well chosen, it may limit the possible performance of the algorithm and thus the quality and reliability of the obtained measurement. In a few words: it is crucial to use the least number of parameters to describe the displacement fields, but as this number is reduced the risk of excluding the actual displacement from the trial space increases, and hence it may induce a model error [23, 94]. Thus it is essential to judge the quality of the obtained displacement from the residual field ρ to check whether manifestations of unanticipated phenomena would not be visible.

Another factor may be taken into account, namely, computation time. The manipulation of a large quantity of data naturally leads to heavy computational load. Hence a natural idea is to partition the images into small subvolumes and register them independently. When subvolumes are small, it is not needed to incorporate many parameters to account for the local kinematics, and hence one may be faced with a large number of very small sized problems, each of which being possibly addressed in parallel (see Section 5.2). This is the spirit of the so-called *"local"* approaches.

3.2.1 Local DVC

As of today, local approaches to DVC are more often used than global approaches (see all the examples discussed in the introduction). There are several reasons, one of them being that they were developed ten years earlier than global approaches. Local DVC was first implemented in which the mean 3D translations per considered subvolume were evaluated [12]. The local rotations were subsequently added in the set of measured degrees of freedom per subvolume [207]. The method was applied for the analysis of a compression test on aluminum foam (*i.e.,* representative of the behavior of trabecular bone). An extension of the previous technique is to apply it to measure the rigid body motions of grains of complex shape. It has been referred to as discrete DVC [86,3] and has been utilized to study strain localization in sand for which the local grain rotations play a major role. The first order warping of subvolumes was proposed by Bornert *et al.* [18] and Verhulp *et al.* [230]. Higher order interpolations were implemented later on [70,130, 186]. All these improvements aim at better capturing the local kinematics arising in mechanical tests.

However, even if more and more parameters are used to perform the registration of subvolumes, often only the displacement vector of the center is kept, and a final post-processing is carried out that consists of computing an interpolated (and smoothed) displacement field based on the discrete

measurements at each subvolumes center. This last operation is performed without reference to the analyzed images and thus is not considered here as part of the DVC computation. However, one should note that this is a critical step for computing, say, strain fields.

The interested reader will find many details on this technique in the first review paper on DVC [11]. Similarly, some examples can be found in the same paper on its early use. The introduction of the present paper also lists more recent applications. In order to have a fully dense displacement evaluation (*i.e.,* for *any* position within the ROI), global approaches were introduced. The registration is therefore using all the voxels belonging to the ROI at once.

3.2.2 Global DVC

Global approaches to DVC were developed more recently. In that case, the kinematic degrees of freedom are spatially coupled, and hence there is no way to compute parts of the problem independently except if parallel algorithms based on domain decomposition methods are implemented [176]. The latter ones have yet to be extended to global DVC. A single and hence "global" solution has to be determined at once. This may appear as leading to very heavy computations. However, a number of algorithmic features may be used to preprocess some computations used several times. It then appears that the computation of $\widetilde{g}$ with the current determination of the displacement field is the most time intensive part of the computation, and hence computing time is (today!) not a relevant argument for choosing one approach or another one.

The first implementation of a global approach consisted of discretizing the region of interest with 8-noded cube (C8) elements for which trilinear shape functions are chosen [197]. It is now referred to as C8-DVC. It is to be noted that there is not a big difference between local and global descriptions of the kinematics. The same type of intrinsic complexity may be incorporated within one C8-element and one local cubic zone of the same shape and size [122]. However, within a global setting, the displacement field is continuous at *any* location within the ROI (without resorting

to a post-processing step), and the field used for the determination is trusted for *each* voxel, rather than keeping only the central displacement and discarding all other computed parameters. Moreover, the global feature of the approach leads to the fact that neighboring elements help each other. If one element lacks contrast but its surrounding ones are contrasted then global DVC may still converge and succeed in determining the displacement field [156,30,157,28]. Most applications of global DVC were based upon finite element discretizations of the ROI. This is not mandatory. For instance, spectral approaches have been implemented even more recently and, up to now, have been only applied to synthetic cases [159].

Most of the global DVC results have been obtained by using C8 elements [197], which is a natural choice to make structured meshes compatible with the underlying voxels. More recently, T4 elements have also been used [93]. One of their advantages lies in the fact that more complex geometries can be faithfully meshed (see Figure 5). In both cases bilinear or linear shape functions have been considered. Higher order displacement interpolations may be considered. However, it will require the size of the elements to be increased in order to keep the uncertainty levels under control. Since DVC analyses are an inverse problem, the general guideline is the smaller the number of unknowns with respect to the available number of voxels, the lower the measurement uncertainty (this observation is true for local and global DVC). However, if the number is too small, interpolation errors may occur. The gray level residuals are the key quantity to make sure the choices have been adequate.

When studying cracks, the continuity property is no longer satisfied across the cracked surface. As earlier mentioned, this violation will often be quite visible in the residual fields [192,133,198, 94]. This is a very nice property as it allows one to clearly see a crack that may sometimes be difficult to detect otherwise. Segmentation may then be quite easy. Moreover, it has been proposed to use an enriched kinematics, following X-FEM approaches (as in 2D-DIC [188]), through an eXtended C8-DVC (or XC8-DVC) [192,185].

To illustrate such situations, let us consider a four-point flexural test on plasterboard. This material is composed of a plaster foam core cast between two paper linings. It now is the most widely used interior finish in construction. In addition to the fire resistance to be checked, a lightweight plate must meet mechanical requirements, the most severe of which is resistance to flexure, a crucial mechanical property for transport, handling and installation of the plate. The studied sample was prepared from industrial plasterboard and cut to a size of $200 \times 13 \times 15$ mm^3. The outer span was 150 mm, and the inner span 40 mm. The supports were machined PMMA cylinders 16 mm in diameter. The setup used in this study is shown in Figure 11(a). It enables two specimens to be tested at the same time. The central part of the device is clear from any obstruction in order to allow for x-ray transmission. Loading was applied manually by turning the two wing screws.

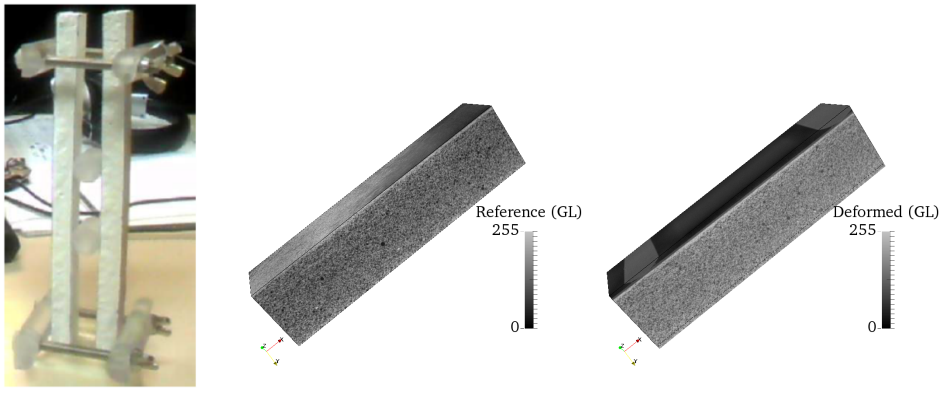

(a) (b) (c)

Fig. 11 (a) In-situ flexural testing device. The sample was imaged in the initial state (*i.e.,* without loading, b) and at several loading levels (the final deformed configuration is shown in c). 1 voxel $\equiv$ 50 µm

The experiment was carried out on LMT's tomograph (NSI X50+) with the following acquisition parameters: the beam tension is 90 kV and the electron current 200 µA, the physical size of one voxel is 25 µm. 900 radiographs were acquired in a 360°-rotation for each scan. The total du-

ration of an acquisition is 60 min. The sample was imaged at initial state and then at three levels of loading. Figure 11(b-c) shows the analyzed volumes by DVC. The ROI after voxel aggregation has a size of 792 $\times$ 192 $\times$ 192 voxels. The physical voxel size then becomes 50 µm. No crack is visible on the section of the volume in the deformed configuration.

The size of the C8 elements was chosen to be equal to 12 voxels. The DVC results are shown in Figure 12. The root mean square correlation residual for the analyzed scan is equal to 2.65 % of the dynamic range of the reference scan. This level being virtually identical to that observed when no crack is present validates the registration. The gray level residual field shows hardly visible traces of cracks (Figure 12(a)) since their opening is very small (*i.e.,* less than one voxel). Discontinuities on the displacement fields are less visible; this is related to the effect of the continuity requirement on the displacement fields (*i.e.,* smoothing effect). Given the small dynamic range of the displacement field, local fluctuations are due to measurement uncertainties. Conversely, the maximum eigen strain field gives very clear indications of the presence of numerous cracks (Figure 12(c)). The crack spacing is of the order of the thickness of the plate.

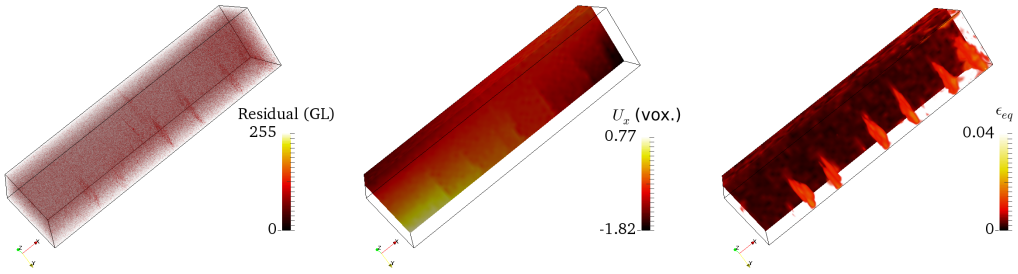

(a) (b) (c)

Fig. 12 DVC results in 4-point flexure. 3D renderings of thresholded gray level residual (a), longitudinal displacement (b) expressed in voxels (1 voxel $\equiv$ 50 µm), and maximum eigen strain fields (c)

Let us insist on the fact that the tomographic observations alone would not allow the mechanism of failure of plasterboard to be deduced from such tests. The contribution of DVC is crucial in order to finely analyze them.

3.3 Numerical implementation

In order to detail the numerical implementation, the sum of squared differences similarity criterion is chosen as it is the most generic one (*i.e.,* relevant for Gaussian and white noise). Thus

$$\mathfrak{T}_{\mathrm{DVC}}[\boldsymbol{u}] = \sum_{\boldsymbol{x}} \left(g(\boldsymbol{x}+\boldsymbol{u}(\boldsymbol{x})) - f(\boldsymbol{x})\right)^2 \tag{19}$$

As previously discussed, a space of displacement field $\mathcal{U}$ is selected, and introducing a kinematic basis with a set of vector fields $\boldsymbol{\phi}_i(\boldsymbol{x})$, is chosen so that the displacement is expressed as

$$\boldsymbol{u}(\boldsymbol{x}) = \sum_i u_i \boldsymbol{\phi}_i(\boldsymbol{x}) \tag{20}$$

Let us note that such a writing holds for both local and global methods. Local would simply mean that some functions $\boldsymbol{\phi}_i$ and $\boldsymbol{\phi}_j$ have a non overlapping support when $i \neq j$. With those notations, DVC consists of measuring all amplitudes u_i that may be gathered into a (long) column vector of unknowns denoted $\{\boldsymbol{u}\}$.

The minimization of $\mathfrak{T}_{\mathrm{DVC}}$ is performed using Newton's descent scheme. The problem being nonlinear, it is solved iteratively, by computing incremental corrections $\{\delta\boldsymbol{u}\}$ to the current estimate at step n, $\{\boldsymbol{u}\}^{(n)}$, so that $\{\boldsymbol{u}\}^{(n+1)} = \{\boldsymbol{u}\}^{(n)} + \{\delta\boldsymbol{u}\}$. The correction is computed from the osculating quadratic form that approximates $\mathfrak{T}_{\mathrm{DVC}}$. The following linear system is thus to be solved

$$[\mathbf{M}]\{\delta\boldsymbol{u}\} = \{\boldsymbol{b}\} \tag{21}$$

where the matrix $[\boldsymbol{M}]$ is the Hessian of $\mathfrak{T}_{\mathrm{DVC}}$, which can be computed once for all at convergence [197,170], *i.e.,* replacing $\widetilde{g}_{\boldsymbol{u}}$ by f

$$M_{ij} = \sum_{\boldsymbol{x}} (\boldsymbol{\nabla} f(\boldsymbol{x}) \cdot \boldsymbol{\phi}_i(\boldsymbol{x}))(\boldsymbol{\nabla} f(\boldsymbol{x}) \cdot \boldsymbol{\phi}_j(\boldsymbol{x})) \tag{22}$$

and the right hand side vector is computed (and this is critical) *without approximation*

$$b_i = \sum_{\boldsymbol{x}} (\boldsymbol{\nabla} f(\boldsymbol{x}) \cdot \boldsymbol{\phi}_i(\boldsymbol{x}))(\widetilde{g}_{\boldsymbol{u}}(\boldsymbol{x}) - f(\boldsymbol{x})) \tag{23}$$

The pseudo-inverse of $N_i(\boldsymbol{x}) = (\boldsymbol{\nabla} f(\boldsymbol{x}) \cdot \boldsymbol{\phi}_i(\boldsymbol{x}))$ is recognized, so that $[\boldsymbol{M}] = [\boldsymbol{N}]^\top [\boldsymbol{N}]$, $\{\boldsymbol{b}\} = [\boldsymbol{N}]^\top \{\boldsymbol{\rho}\}$, and one may also write

$$\{\delta \boldsymbol{u}\} = [\boldsymbol{M}]^{-1} \{\boldsymbol{b}\} = [\boldsymbol{N}]^\dagger \{\boldsymbol{\rho}\} \tag{24}$$

where the notation $[\boldsymbol{N}]^\dagger \equiv ([\boldsymbol{N}]^\top [\boldsymbol{N}])^{-1} [\boldsymbol{N}]^\top$ stands for the so-called Moore-Penrose pseudo-inverse matrix [154,179].

There is a huge diversity of issues associated with nonlinearities. For DVC, they are not too limiting. The approximation of the objective functional by its osculating paraboloid (*i.e.,* using the Hessian at convergence) is generally an excellent choice. Yet there are two pitfalls to avoid. The first one is the existence of poorly conditioned modes when too many kinematic degrees of freedom are proposed as compared to the available information. Typically, when very small subvolumes, or very small elements are considered, the ratio of the to-be-measured parameters to the given information becomes too large, eigen-modes of the $[\boldsymbol{M}]$ matrix appear with very small eigen values. Here the solution is to be less ambitious for the spatial resolution, and/or to provide additional prior knowledge [123,122]. This is the spirit of regularization that will be detailed further down.

The second pitfall is that the above osculating harmonic potential is a good approximation only within a range of variation of the displacement that can be compared to the correlation length of the image texture. This means that when $\boldsymbol{u}$ is close to the actual solution, say because

it has been well initialized, it will easily converge to the correct solution. In contrast, for very poor initial guesses, *i.e.,* very remote from the actual one, the above Newton's algorithm may not converge.

The previous observation applies to both local and global approaches. Finding suitable starting points for the final optimization step is critical, and all usable codes spend considerable effort on this. One of the easiest ways to circumvent this problem is to devise multiscale approaches [197, 97, 60, 45]. If the (reference and deformed) images are low-pass filtered prior to registration, local minima are erased with the wavelength of the filter around the solution. This naturally provides a much more robust approach. However, because images are low-passed filtered, the registration is not very precise. Understanding that this filtering is only a temporary operation provided to get an approximate solution to start with, then the solution is to built up a pyramid of progressively more and more filtered images, which can conveniently be down-sampled to reduce the computation load, and start registration from the top of the pyramid, and use the resulting displacement field as an initialization of the lower level, down to the original image in which no filtering is being used [98, 245, 16, 187, 80].

As detailed below, regularization will provide an additional functional $\mathfrak{T}_{\mathrm{Reg}}$ to be added to $\mathfrak{T}_{\mathrm{DVC}}$. The numerical strategy to solve the regularized problem will be essentially the same as above. A new Hessian and second member will be computed and added to the above $[\boldsymbol{M}]$ and $\{\boldsymbol{b}\}$, so as to estimate the displacement field. The regularized Hessian is aimed at obtaining a better conditioning, and thereby decreasing the uncertainty, as will be shown in the next section.

3.4 Identification and Validation

In the above discussions, the kinematic bases were chosen mostly based on numerical convenience. However, little consideration was paid to the relevance of a particular basis. To do so, it is necessary to incorporate some additional information coming from the mechanical behavior of the sample.

Thus prior to discussing more elaborate regularization strategies, a short review of the usage of DVC-measured displacement fields in the context of mechanical identification is proposed.

Comparisons between DVC measurements and FE calculations have been first attempted for cancellous bone to validate the strain predictions of the numerical model [242]. A good agreement was observed in the loading direction, yet less accuracy was achieved in the transverse directions. It may be hypothesized that parameters affecting the accuracy may include lateral boundary conditions. It was confirmed for a scaffold implant under uniaxial compression for which the measured boundary conditions were applied to each boundary of the region of interest. Good agreements between the results from the DVC measurements and the FE simulations were obtained in the primary loading direction as well as in the lateral directions [137].

It is worth noting that *experimental* boundary conditions are very important inasmuch as one cannot guarantee that a mechanical test be always perfect (in particular for in-situ testing where the rigidity of testing devices is often a limitation, see Section 2). This is especially true in biomechanics where the specimen shape is not chosen but given [106]. For instance, the failure mechanisms may change when intervertebral disks are present or not. Further, when experimentally measured boundary conditions are utilized in FE simulations, the displacement errors between DVC-measured fields and computed fields via FE simulations were the lowest [108]. This trend was also recently confirmed in the study of cancellous bone [37] and the analysis of vertebral failure patterns [108]. Further, micromotions captured by DVC were shown to be consistent with FE simulations of implants [210]. Damage in bone-cement interfaces was assessed via DVC and consistently compared with FE simulations [221].

Validation frameworks based on 3D (and 4D) imaging have been proposed [160, 29, 37]. One key aspect is related to the management of boundary conditions [78, 185, 206], as discussed above for biomechanical studies. If measured boundary conditions are used, it is possible to evaluate gray level residuals from simulated displacement fields and estimate the *absolute* quality of numerical

models [29]. Otherwise, only *relative* qualities are obtained when measured displacements are compared with computed fields. With such approaches, ductile damage predictions could be probed for different experimental configurations with cast iron and partial validations were achieved with microscale FE simulations [29, 206].

Extended FE simulations were validated against experimentally measured displacement fields via extended DVC by comparing measured and predicted profiles of stress intensity factors [185, 189]. Crack opening displacements measured via DVC were compared to predictions by FE analyses for a test with a chevron notched sample made of polygranular graphite to validate a cohesive zone model [160]. Similar analyses were reported for a woven ceramic matrix composite [202]. Phase field simulations were validated against experiments through the comparison of crack patterns in lightweight concrete and plaster [166].

Very few parameter calibrations have been reported so far when dealing with DVC measurements and FE simulations. Among them, the virtual fields method was used to calibrate elastic parameters for cornea [73], trabecular bone [79] and 3D particulate composite [184]. Finite element model updating was used to calibrate plastic parameters when Al-SiC composite and cast magnesium alloy were indented in-situ [162]. Such parameters were also calibrated for nodular graphite cast iron when cyclically loaded in uniaxial tension [93]. The criterion describing the transition from pristine to compacted (*i.e.,* crushed) states was determined by analyzing in-situ indentation tests on plaster foam [21].

3.5 Regularized DVC

In registration techniques applied to medical imaging, regularization techniques have been considered very early on. They all derive from Tikhonov-like propositions [215] to account for various constraints by adding a penalty term to the DVC cost function [199, 102, 195, 115]. In experimental mechanics such type of approaches were introduced more recently [123, 122, 214] extending elastic

regularization initially introduced in 2D-DIC [190,218]. The regularization strategy allows the DVC problem to be made well-posed even when discretized onto a very fine mesh. It was shown that the ultimate limit of a regular cubic mesh with elements reduced to a single voxel could be handled with such a strategy [123]. However, in that case, the number of unknowns becomes very large, and the regularization kernel involves a more complex problem to solve, and hence regularized DVC becomes much more demanding in terms of computation time and memory management. To overcome this difficulty, a dedicated GPU implementation has been set up that can handle several million degrees of freedom problems within an acceptable time (less than 10 minutes) [122]. When analyzing localized phenomena (*e.g.,* strain localization and cracks), special care should be exercised to properly capture high local strain gradients [214] or displacement discontinuities [94,119]. It will be illustrated in Section 3.5.4.

3.5.1 Regularization functional

When designing the penalty term, two questions have to be addressed: What should the penalty be based on in order not to bias the measurement? How should its weight be set?

The very early suggestions by Tikhonov and Arsenin [215] were to add to the DVC functional a term such as $\|\boldsymbol{u}\|^2 = \sum_{\boldsymbol{x}} |\boldsymbol{u}(\boldsymbol{x})|^2$. This choice is here not appropriate as it tends to drag displacements toward $\boldsymbol{u} = \boldsymbol{0}$, especially in zones where the image texture is poor. Introducing the norm of a differential operator such as $\mathfrak{T}_{\text{Reg}}[\boldsymbol{u}] = \sum_{\boldsymbol{x}} |\mathcal{L}(\boldsymbol{u})|^2$, where $\mathcal{L}(\boldsymbol{u}) = \nabla \otimes \boldsymbol{u}$ instead of the raw displacement, would be a better choice as uniform translations would not be affected as they belong to the kernel of the gradient operator. However, rigid body rotations have a nonzero gradient and hence they would be dampened out by such regularization. Requiring that all rigid body motions belong to the kernel of $\mathcal{L}(\boldsymbol{u})$, selects automatically linear functions of strain. Hence $|\mathcal{L}(\boldsymbol{u})|^2$ coincides with the potential energy density of a linearly elastic solid. Such a form may be

suited when observing a solid that is not subjected to a mechanical loading, but for mechanical tests, such a regularization would drive the solution toward a rest state.

Following along these lines leads to a second order differential operator for $\mathcal{L}$, which can be compared to the divergence of the stress field for a linear elastic solid. When a finite element description is used for the displacement field, *i.e.,* supported by a mesh, one may rely on the numerical model of elasticity to relate the $\mathcal{L}$ operator to the finite element stiffness matrix $[\boldsymbol{K}]$. In the absence of body forces, this matrix applied to the vector of nodal displacement provides a vector of unbalanced forces at nodes $\{\boldsymbol{f}\} = [\boldsymbol{K}]\{\boldsymbol{u}\}$. Choosing as penalty the quadratic norm of the vector $\{\boldsymbol{f}\}$ (restricted to internal nodes) gives precisely what is needed as a Tikhonov regularization functional, the kernel of which contains all displacement fields that are solution to a linear elastic problem [123,122]. This means that a zone where the texture is poor or simply missing, would be interpolated as the solution to an elastic problem matching the displacement at the boundaries where it is known. This is in line with the "regularization" property of this additional functional, which is to alleviate ill-conditioning by adding prior knowledge on the displacement field.

It is to be observed that linear elasticity involves several parameters that can be tailored to a situation at play [123,122,214,94]. If the actual behavior of the sample is elastic, one would like to use a regularization kernel as close as possible to the actual constitutive law. However, sometimes, one may want to depart from the real behavior. For instance, for developed plastic flows, one may neglect elastic strains, and hence the elastic kernel to be used for regularization should mimic plastic strain. For instance, plastic strains are generally isochoric, and hence one may choose an incompressible elastic law to prevent any volume change [214]. More generally, the tangent behavior is a good candidate for identifying the proper elastic law to be used. When approaching a perfectly plastic plateau, there exists a strain direction where the elastic stiffness

vanishes. This calls for an anisotropic elastic kernel that would leave free the easy strain direction but would penalize shear in a different direction.

3.5.2 Regularization weight

The second question to be answered deals with the weight to be given to the regularization kernel. Different heuristics have been proposed in the literature [58]. However, it is difficult to assess how relevant they would be for the present purposes. Here it is proposed to follow a different route that gives a simple interpretation to this weight.

For any trial displacement field, $\boldsymbol{u}$, the similarity measure of DVC provides a cost function, $\mathfrak{T}_{\mathrm{DVC}}[\boldsymbol{u}]$. In the immediate vicinity of the optimal solution, $\boldsymbol{u}^*$, one may Taylor expand the functional $\mathfrak{T}_{\mathrm{DVC}}[\boldsymbol{u}^* + \boldsymbol{\delta u}]$ for a small perturbation, $\boldsymbol{\delta u}$, as

$$\begin{aligned} \mathfrak{T}_{\mathrm{DVC}}[\boldsymbol{u}^* + \boldsymbol{\delta u}] &= S(f, \widetilde{f}_{\boldsymbol{\delta u}}) \\ &= S(f, f + \boldsymbol{\nabla} f \cdot \boldsymbol{\delta u}) \\ &= S_0 + S_2[\boldsymbol{\delta u}] + \mathcal{O}[\boldsymbol{\delta u}^4] \end{aligned} \tag{25}$$

where S_0 is a constant (which can be neglected in the minimization), and S_2 is a quadratic form in $\boldsymbol{\delta u}$ whose kernel is the Hessian of $\mathfrak{T}_{\mathrm{DVC}}$, denoted as $[\boldsymbol{M}]$ in Equation (22). The linear term in $\boldsymbol{\delta u}$ is absent as a result of S being minimum. It is to be noted that in the above equation, the second argument of S has been changed to f because $\widetilde{g}_{\boldsymbol{u}^*} \approx f$. S_2 is thus the osculating harmonic approximation of the nonlinear DVC functional. Using the notation $\{\boldsymbol{u}\}$ for the discretized displacement field represented as a column vector of nodal displacements, S_2 reads

$$S_2[\{\mathbf{u}\}] = \{\mathbf{u}\}^\top [\mathbf{M}] \{\mathbf{u}\} \tag{26}$$

Similarly, the regularization functional using linear elasticity is a quadratic form of the displacement field. Within a finite element discretization where $[\boldsymbol{K}]$ is the elastic stiffness matrix, one can write

$$\mathfrak{T}_{\mathrm{Reg}}[\{\boldsymbol{u}\}] = \{\boldsymbol{u}\}^\top [\boldsymbol{K}]^\top [\boldsymbol{D}] [\boldsymbol{K}] \{\boldsymbol{u}\} \tag{27}$$

where $[\boldsymbol{D}]$ is a diagonal matrix valued 1 for internal nodes (where the balance equation holds) and 0 on boundary nodes (where a displacement or nonzero load is prescribed).

Let us now consider as a trial displacement field a plane wave, $\boldsymbol{v}_\lambda(\boldsymbol{x}) = \boldsymbol{e}_1 \exp(i\boldsymbol{e}_2 \cdot \boldsymbol{x}/\lambda)$ with a wavevector along $\boldsymbol{e}_2$, a unitary vector, with displacements parallel to $\boldsymbol{e}_1$ (chosen perpendicular to $\boldsymbol{e}_2$ so that the strain is pure shear), and $2\pi\lambda$ the wavelength. When the wavelength is varied, on average the quadratic form S_2 remains constant. Conversely, $\mathfrak{T}_{\mathrm{Reg}}[\boldsymbol{v}_\lambda]$ is proportional to the inverse fourth power of λ. This exponent 4 defines the "spectral sensitivity" of the regularization term, as compared to 0 for the DVC problem. This comes from the fact that $[\boldsymbol{K}]$ is the discrete form of a second order differential operator acting on the displacement field. This difference in sensitivity requiring an intrinsic length is now exploited to write a full cost function as

$$\mathfrak{T}_{\mathrm{Tot}}[\{\boldsymbol{u}\}] = \frac{(\mathfrak{T}_{\mathrm{DVC}}[\{\boldsymbol{u}\}] - S_0)}{S_2[\{\boldsymbol{v}_\lambda\}]} + \frac{\xi^4}{\lambda^4} \frac{\mathfrak{T}_{\mathrm{Reg}}[\{\boldsymbol{u}\}]}{\mathfrak{T}_{\mathrm{Reg}}[\{\boldsymbol{v}_\lambda\}]} \tag{28}$$

Let us note that the weight of the regularization part is set by a free parameter, ξ, whose meaning becomes transparent. The relative magnitude of the two terms in the above sum depends on the length scale over which the displacement field varies. When this scale is larger than ξ the DVC functional dominates over the regularization part, and conversely, shorter length scales are controlled by the regularization part. Thus the above expression has a minimizer that is a low-pass filtered DVC displacement field, and tuning ξ allows one to adjust the cut-off frequency.

In order to better appreciate the usefulness of this formulation, it is worth making the following remarks:

– Any discretization involves a cut-off length scale, namely, the subvolumes size in local DVC, or the element size in unregularized global DVC, but in those approaches the small-scale shape functions are not designed to be mechanically realistic but rather convenient, either for parallel computation or for benefitting from all meshing tools available. In contrast, the above regularization uses a much more realistic small-scale displacement interpolation;

- Provided the regularization length is larger than the element size, the influence of the mesh (and its fineness) is reduced to a minimum;
- Changing the regularization length is trivially performed without having to re-mesh. It is noteworthy that for slender objects or regions of interest, one may introduce a regularization length that is larger than the smallest size of the sample/ROI. Such a property is not available using a regularization based on the window size or element size in the mesh;
- It has been shown that using the ultimate regular mesh composed of $1 \times 1 \times 1$ voxel cubes could be handled with such a regularization, with a weight that could be decreased down to very few (*i.e.,* 3.3) voxels [123];
- Edges (which are not free boundaries) are not regularized by the above construction. They cannot be considered as balanced nodes because the outer region exerts unknown forces / torques on the studied domain. It is however possible to construct linear operators acting on the boundary nodal displacements that behave in the same way (invariant under a rigid body motion, and are the discrete version of a second order differential operator [123, 214]). This regularization introduces a similar tunable smoothness as the bulk regularization, although the mechanical justification is more fragile. However, it remains exactly within the spirit of a mathematical regularization for ill-conditioned problems;
- The tunable length scale is convenient to capture a first rough approximation of the displacement field (*i.e.,* using a large regularization length scale), and progressively relaxing ξ to a small value. As shown in 2D analyses [218], even in the limit of a vanishing ξ, such an initialization procedure may provide better solutions than that obtained with the same discretization but without regularization [29].
- Although this regularization is a filter, it should not be confused with a filtering performed in a post-processing stage. The former is applied together with the registration procedure, and hence the filtered field is evaluated on its registration quality, while the latter has lost

its connection with the images, and hence the detrimental effect of filtering on registration cannot be estimated.

If the linear elastic problem used for the regularization is not trusted, then a small regularization length scale is to be chosen, and regularization will only provide an effective "shape function" with nicer regularity properties than standard finite elements. Alternatively, if identification is aimed at, then ideally an infinite regularization length scale will leave enough freedom to account for arbitrary boundary conditions, and this without negative incidence on the value of the residual. Conversely, a wrong constitutive law will lead to higher residuals and hence minimizing the residuals (as usually carried out in DVC) with respect to the constitutive parameters is an identification procedure (i.e., "integrated" if the regularization length is infinite).

3.5.3 Extension to nonlinear regularization

The above regularization was set to the simplest form that could be introduced without interference with naturally expected displacements. Thus the lowest order linear differential operator was selected. It was very recently extended to hyperelasticity (*i.e.,* in a finite strain framework [76]), and applied to cardiac magnetic resonance images. However, there is no first principle argument that would prevent from using any more sophisticated nonlinear laws. In the field of applied mathematics, other nonlinear regularizations have been proposed [58]. For instance, rather than using an L_2-norm of the unknown field or of a differential operator acting on it, other norms have been proposed such as L_p

$$\mathfrak{T}^p_{\mathrm{Reg}}[\boldsymbol{u}] = \left(\int |\mathcal{L}(\boldsymbol{u})|^p d\boldsymbol{x} \right)^{2/p} \tag{29}$$

When $\mathcal{L}$ is the symmetric part of the gradient, and $p = 2$ this form looks like an elastic energy density. When p tends to 1, the (nonlinear elastic) behavior would look like perfect plasticity. When p is less than 1, a softening branch develops implying loss of convexity. In fact convexity ($p \geq 1$) is a very convenient property that ensures the existence of a unique minimum and hence

an independence with respect to the algorithm used to minimize the functional. On the other hand, $p \leq 1$ tends to concentrate high strain over small supports, a feature called "localization instability" frequently met in plasticity and damage theories [126]. When dealing with cracks, it is very useful to be able to concentrate strains (up to displacement discontinuity) over a support that should finally coincide with a possible crack. Hence, here, what is usually a major difficulty for numerical modeling becomes an advantage. In such a case, one would appreciate both convexity *and* localization ability, thereby leading to $p = 1$. Higher order $\mathcal{L}$ operators could also be considered, such as those expressing balance of inner nodes but for a nonlinear elastic law mimicking perfect plasticity.

3.5.4 Application to cracked sample

The flexural test discussed in Section 3.2.2 is again considered to show the effect of elastic regularization. For comparison purposes, Figure 13(a,d) shows the displacement field in the longitudinal direction, and the maximum principal strain when unregularized DVC is run with 12-voxels elements (see Figure 12). Figure 13(b,e) shows the same fields when regularized DVC is run with a regularization length of 120 voxels with the same mesh. The dimensionless root mean square correlation residual is slightly higher (*i.e.,* 2.67 % instead of 2.65 % for unregularized DVC), which is to be expected since the displacement field is more constrained in the present case. The displacement gradients have been filtered out due to the elastic regularization, which acts as a low-pass filter. The high frequency fluctuations (*i.e.,* measurement uncertainties) have also been taken out since they are not mechanically admissible.

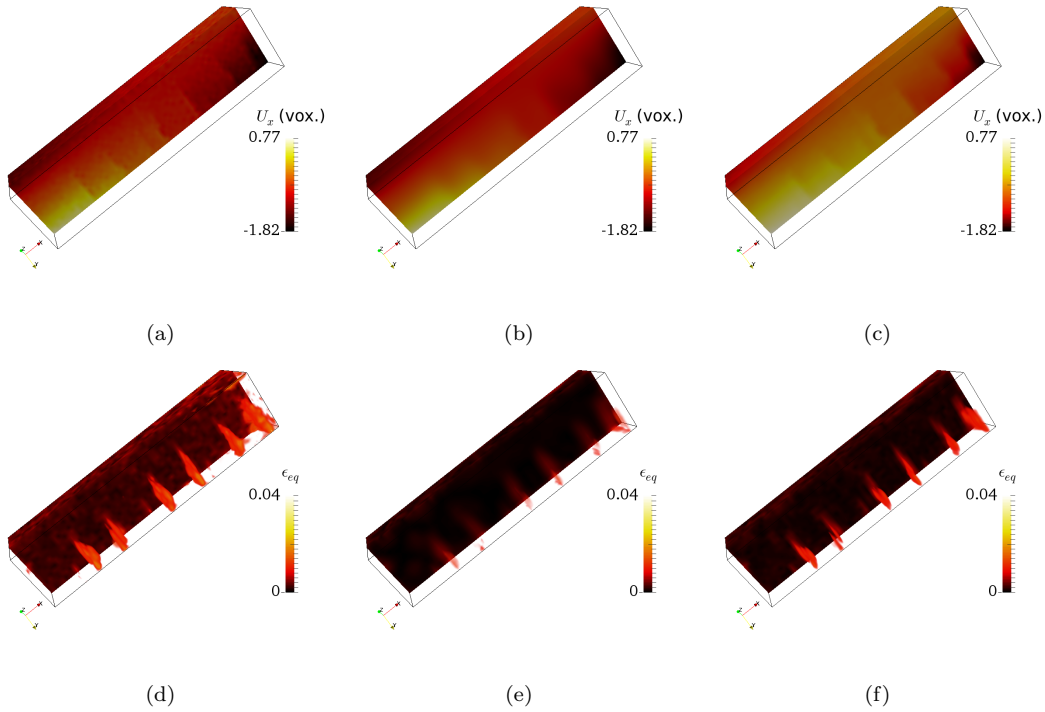

Fig. 13 Foamed gypsum subjected to 4-point flexure. 3D renderings of the longitudinal displacement (expressed in voxel,1 voxel $\equiv$ 50 µm) and measured with regularized DVC with different regularization kernels: (a) no regularization (or vanishing regularization length ξ), (b) elastic law with large length $\xi = 120$ voxels, (c) damage law with small length $\xi = 12$ voxels. Corresponding maximum equivalent strain for the same three laws shown respectively in (d), (e) and (f). The same mesh is used in all cases.

To localize the strain field, the regularization is relaxed by using a damage variable [94]. A final calculation is then run with no damage and a very small regularization length (*i.e.,* 12 voxels) in order to only filter out high frequency fluctuations. The root mean square correlation residual is equal to 2.65 % (as for unregularized DVC). Figure 13(c,f) shows the displacement field in the longitudinal direction, and the corresponding maximum principal strain. In the present case, the displacement field is very smooth outside the cracked areas, which are well captured and localized (at the scale of one element size).

3.6 Integrated DVC

The limit of a diverging regularization length scale $\xi \to \infty$ is also well-defined. It reduces the search space for $\boldsymbol{u}(\boldsymbol{x})$ to $\mathcal{U}_1$ that is now defined as the kernel of the operator $\mathcal{L}[\boldsymbol{u}]$. Therefore, the dimensionality of this space is much reduced, as typically a unique solution for $\boldsymbol{u}$ can be computed when boundary conditions are fixed. Allowing for some variability of the constitutive parameters (and possibly also boundary conditions) all gathered into a column vector $\{\boldsymbol{p}\}$, allows the set of all mechanically admissible displacement fields to be defined as an *affine* space about a nominal $\{\boldsymbol{p}_0\}$ vector

$$\boldsymbol{u}(\boldsymbol{x}, t; \{\boldsymbol{p}\}) = \boldsymbol{u}_0(\boldsymbol{x}, t; \{\boldsymbol{p}_0\}) + \boldsymbol{s}_i(\boldsymbol{x}, t; \{\boldsymbol{p}_0\})(\{\boldsymbol{p}\} - \{\boldsymbol{p}_0\}) \tag{30}$$

where $\boldsymbol{s}_i$ is the sensitivity of the displacement field with respect to p_i (*i.e.*, $\boldsymbol{s}_i(\boldsymbol{x}, t; \{\boldsymbol{p}_0\}) = \partial \boldsymbol{u}/\partial\{\boldsymbol{p}\}(\boldsymbol{x}, t; \{\boldsymbol{p}_0\})$). In the above expression the dimensionality of the displacement field is that of the unknown vector $\{\boldsymbol{p}\}$. This generally very small dimensionality implies also a much reduced value of the uncertainties as compared to less guided DVC approaches. One example of such an approach where the number of unknowns was turned from several 10^5 down to about 10 can be found in Ref. [23]. The advantage of such approaches is that the measured kinematic field is also statically admissible (in the finite element sense). However, the difficulty is that the parameterized constitutive law has to be realistic as compared to expectation. In some cases, elasticity is clearly sufficient [23,21]. In some other cases, elastoplastic postulates were tuned at meso [93] or micro [31] scales.

In the following integrated DVC will be applied to a pre-cracked parallelepipedic sample made of spheroidal graphite cast iron (Figure 14(a)) and subjected to tensile loading by using the testing machine shown in Figure 7(a). The same procedure as discussed in Refs. [133,132,185] was followed in the sample preparation. The cross-section of the sample is 1.6×1 mm^2. The

specimen is loaded in seven incremental steps (Figure 14(b)). The first two scans of the reference configuration allow displacement uncertainties to be evaluated.

A complete scan of the sample corresponds to a 360° rotation along its vertical axis, during which 1,000 radiographs are acquired with a definition of $1,944 \times 1,536$ pixels. Each scan lasted less than 20 min. The physical voxel size is 7.2 µm, and the reconstructed volume is encoded with 8-bit deep gray levels. In the following, the mesoscopic behavior will be studied. The constitutive equation investigated hereafter is Ludwik's law [136] associated with J2 plasticity and isotropic hardening described by a power law function of the cumulative plastic strain.

The integrated DVC code, Correli 3.0 [121], is a Matlab implementation that uses in a non intrusive way a finite element code to compute the spatiotemporal sensitivity fields in addition to the current estimates of the displacement fields and reaction forces [93]. The inputs to such simulations are the measured displacements of top and bottom boundaries of the ROI. In the present case, the commercial finite element package Abaqus/Standard is used with its built-in constitutive laws. C++ kernels compute all the other data needed to perform DVC analyses, namely, the DVC matrix $[\boldsymbol{M}]$, the instantaneous voxel residuals $\rho(\boldsymbol{x}, t)$, and the instantaneous nodal residual vector $\{\boldsymbol{b}(t)\}$. Binary MEX files were generated and called in the Matlab environment to compute the Hessians and residual vectors to be utilized in the Newton scheme introduced above.

Figure 14(b-d) summarizes the identification results for the mesh considered in the present analysis. To account for the presence of the crack, a node splitting technique is used. The shape of the crack surface is obtained by first running T4-DVC with no crack (*i.e.,* global DVC with 4-noded tetrahedra and linear shape functions). The characteristic element size is equal to 12 voxels (Figure 14(c)). From the gray level residuals of unregularized DVC with no crack, the shape of the crack surface is determined [185].

At convergence, the hardening modulus is found to be equal to 1300 MPa and the hardening exponent is equal to 0.4. The yield stress for an offset of 0.2 % is found to be equal to 200 MPa.

When the measured load history is compared to the corresponding predictions (Figure 14(b)), significant differences are observed. The global residuals are significantly higher than the measurement uncertainties (*i.e.,* 10 times higher). This is an indication of model errors. At least three origins can be invoked in the present case. First, the geometry of the cracked surface is not fully consistent with the experiment. Second the mesh is not fine enough to properly capture mechanical fields via FE simulations. Third, the constitutive law is only an approximation of the actual behavior.

At convergence of the integrated DVC code, the gray level residuals are very low (Figure 14(d)) in comparison with the reference microstructure (Figure 14(a)), except in the immediate vicinity of the crack . This result can be explained by the fact that the mesh is not fine enough to precisely describe the cracked surface. It is worth noting that mesh refinement could be used for integrated DVC as opposed to regular DVC analyses for which the spatial resolution cannot be decreased at will (see Section 4.1). In the other areas of high residuals, it is rather due to the boundary conditions that were not perfectly captured with unregularized (due to the fineness of the mesh). On average, the gray level residuals are only 25 % higher than those observed when virtually no motion occurred (*i.e.,* between scans#1 and #2). Moreover, ring artifacts are seen quite clearly, and contribute to this residual. This is an additional sign that registration was successful. When compared to unregularized DVC, with the same mesh, the global residual is only slightly higher (*i.e.,* a factor 1.25 for integrated DVC instead of 1.22 for unregularized DVC, when the global residuals are normalized by the level observed with almost no motion).

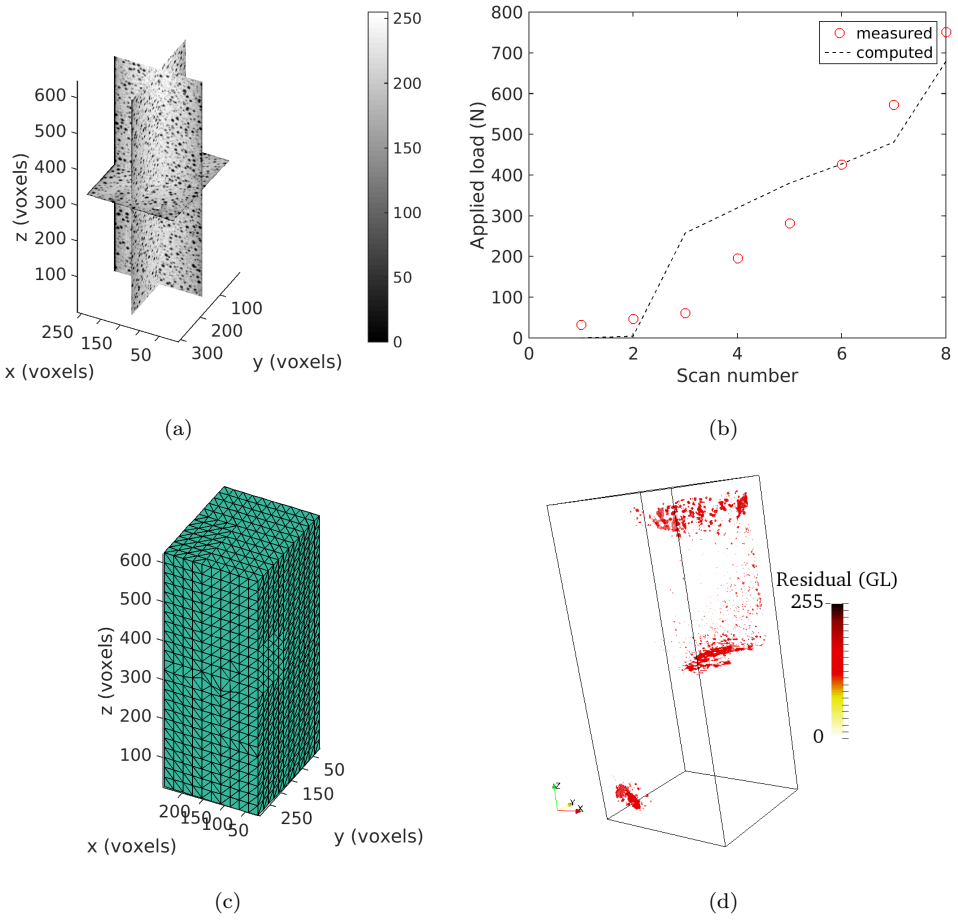

Fig. 14 Identification results via 4D registration. (a) Orthoslice of the gray level volume of scan #1. (b) Comparison of measured and predicted load levels. (c) T4 mesh used in the present study. (d) 3D rendering of the thresholded gray level residuals of scan #8

In the present case, the chosen mesh is not too fine so that DVC and integrated DVC results can be compared. This is generally not the case as integrated DVC allows very fine meshes to be used [93,29,31]. The RMS difference between measured and computed displacement fields is equal to 0.5 voxel. This level is to be compared with the measurement uncertainty. With the chosen discretization, the standard displacement uncertainty is equal to 0.06 voxel. The RMS difference is ≈ 8 times the displacement uncertainty, again signalling a model error. To understand where

the displacement discrepancies are located, Figure 15 shows the displacement fields measured by DVC and integrated DVC for the next to last scan. It is worth remembering that the Dirichlet boundary conditions of integrated DVC are measured data (via regular DVC). Consequently, the displacement errors cancel out at upper and lower surfaces of the considered ROI. However, very close to it the differences are quite significant. This is due to uncertainties in the boundary conditions. Some filtering could used by using verification tools [93]. The other area where the largest gaps are observed in the cracked zone. This is to be expected because of model errors discussed above.

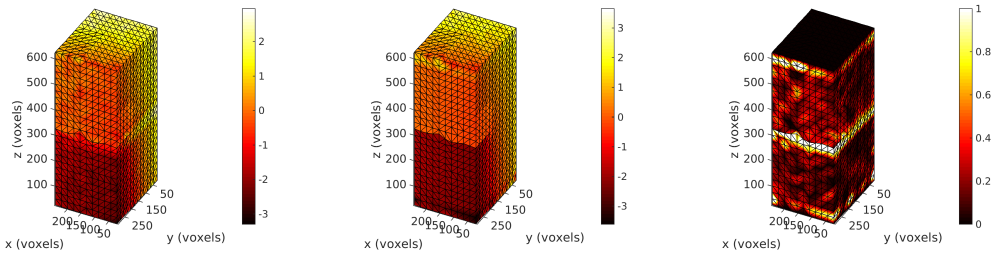

Fig. 15 3D renderings of the longitudinal displacements (expressed in voxels) of scan #7. (a) DVC measurements, (b) integrated DVC at convergence, and (c) difference of the two

The fact that gray level residuals, load residuals and displacement residuals have levels less than ten times the measurement uncertainties shows that the simple elastoplastic model considered herein should not be discarded. However, it should be enriched to account for damage especially at the last load level where all residuals increase significantly. There is clearly some room for progress by improving the numerical model along all the lines discussed above.

3.7 DVC for NDE purposes

Considered from an abstract standpoint, DVC is the art of computing image differences taking into account possible deformations between images. Differences arising from distortions could be erased by taking them into account through corrected images $\widetilde{g}$.

Although most previous examples were taken from mechanically loaded specimen, this is not compulsory. In particular, industrial manufacturing implies the production of a large number of parts of about the same microstructure. DVC can be used for the comparison between a "master piece" and any produced part. Here the displacement field is not physical, but it reflects variable distortions due to the manufacturing process. Some of them could be deemed acceptable and some others not. As such DVC would then provide an NDE of the production line. Additionally residuals would evidence irreducible flaws that are topological differences.

A natural field of applicability of these concepts is NDE of woven composites. These composite materials are becoming key in many applications mainly due to their very attractive specific properties (*e.g.,* strength to weight ratio). They are conformed by yarns (reinforcement phase) woven after a three-dimensional pattern and held together by a resin (matrix phase). The increasing interest in these materials has generated a high demand for proper characterization methods as well as for accurate simulations.

In this context, DVC provides a *quantitative* evaluation of continuous deformations (*e.g.,* stretching and bending of yarns) that may define acceptable/unacceptable weaving distortions due to resin impregnation or infiltration, molding, curing as well as for a qualitative insight into the detection of weaving abnormalities (*e.g.,* missing yarn, bad positioning, loop). The former are called "metric differences," while the latter are called "topological differences" (see Figure 16) as they cannot be reconciled by a simple continuous deformation of the medium [204, 152].

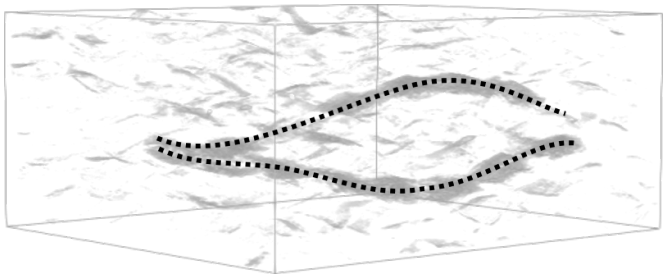

Fig. 16 Residual field. The lowest values are made transparent to allow for visualization of the largest differences. In this particular test case, two yarns were omitted in one weaving as compared to the reference one. The black dotted curves are drawn by hand to guide the reading along the missing yarns. Residuals highlight differences that cannot be resolved by a deformation of the medium, and thus referred to as "topological differences." This example illustrates the potential of DVC for NDE applications

Then the use of DVC under a multiresolution isotropic approach [152] for two different manufactured samples allows for the measurement of relative displacements and subsequent estimation of relative strains (deformations). These calculated relative strains are not a result of any loading prescribed to the sample, but rather of the many phenomena present during the manufacturing process that result in slightly different samples.

Extending this concept to cases where the gray levels may vary (as discussed in Section 3.1.2) offers a very convenient framework for the comparison between a real part (*e.g.,* x-ray scanned after production) and its theoretical model (*e.g.,* CAD, weaving model, or mesh). As such, the studied sample is considered as in a so-called deformed or warped configuration with respect to the virtual reference. This reference configuration corresponds to the ideal weaving pattern, as can be defined by virtual models (FE, CAD). The procedure allows woven composites volumes (obtained from tomography) to be unwarped into a more convenient representation [153].

As expected for woven fabrics, it is important to identify and follow the weaving process itself (*i.e.,* the yarns) from a tomographic image. DVC in such cases may offer a very convenient alternative to segmentation since topology is preserved. The transformation between model and

actual part allows for the transfer of whatever feature available from one world into the other one. For instance, if yarns are labelled in the model, their label can immediately be transferred onto the actual image. If a mesh has been tailored to the model, it can be mapped without effort onto the actual geometry. Shape metrology can be obtained for free. Clearly, manual intervention is possible for extracting such information. Needless to say, this is a tedious and time consuming operation that could suffer from operator bias and lack the required resolution. Alternatively, advanced image processing methods are also available. However they often are too specialized or overly sensitive to slight changes on the input image (*i.e.,* resolution, noise, artifacts) or to the material itself.

In Figure 17, a modified version of the multiresolution isotropic approach helps to overcome the challenge imposed by the poor texture provided by the discretized (*i.e.,* voxelized) version of the weaving model and succeeds in properly relating it to the tomographic image of the manufactured sample. The resulting mapping is used to display the shear strain magnitude onto the virtual model.

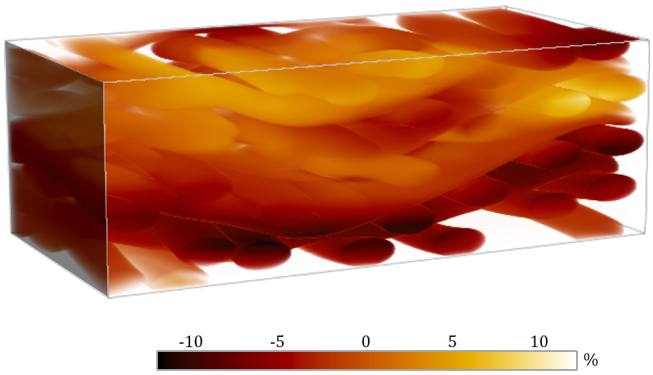

Fig. 17 Example of a computed virtual strain field obtained from a tomographic image projected onto the corresponding virtual model of the textile. The color encoding refers to the shear strain ε_{xy}, where (x, y) is the front plane

In general, DVC applied to composite materials offers applications ranging from NDE of composite parts up to the validation of new weaving architectures for composite structures. Moreover, it improves over current NDE tools since they may not provide enough information to detect subtle deformations (and even not so subtle ones) such as those originated from the aforementioned "topological differences."

This section shows that in particular for (demanding) industrial applications DVC offers unprecedented opportunities at very low cost. Segmentation usually proceeds from the smallest scale toward the larger ones and hence topology is not securely preserved. The advantage of DVC over classical approaches is that the large scale features, and in particular topology, are preserved in the mapping.

4 Uncertainty and bias quantifications

4.1 Uncertainty quantifications

As discussed above, DVC is an ill-posed problem. To circumvent this difficulty, the needed regularization is often implicitly introduced through the choice a kinematic basis for the sought solution. Relaxation of this regularization, as motivated by enhanced spatial resolution, is unavoidably accompanied with a degradation of the measurement uncertainty [18,131,122,46,243]. This effect has been referred to as the "curse of displacement resolution versus spatial resolution in DIC" [96].

There are various ways of estimating the uncertainties of correlation techniques [46]. When only one acquisition is available, artificial motions *i.e.,* generally uniform translations are applied to create a new volume that is subsequently registered with the reference volume [197,14,133, 95,137,46]. For extended DVC, the prescribed translation was uniform or discontinuous to probe the uncertainties associated with discontinuous enrichments [192,185]. This first type of analysis mainly probes the interpolation scheme of the gray levels to achieve sub-voxel resolutions.

The second type of approach also uses only one reference volume but consists of adding noise to create a new volume, which is correlated with its noise-free reference [123,122]. The advantage of such approaches is that i) closed-form solutions can be derived, and ii) their predictions can be validated against actual DVC calculations [122,156,93]. The sensitivity to noise is addressed in this type of procedure.

Last, the two previous sources of uncertainty can be probed in a more reliable way when the same type of analysis is performed with real experimental data [18,134,97,131,46]. Such is the case when analyzing two consecutive scans of the sample in a given loading state (it may also be unloaded) with preferably a deliberately introduced motion between the two acquisitions. The main advantage is that both sources of error are investigated at the same time for the material of interest. For computed tomography, different displacement resolutions have been reported when the displacement is prescribed along or perpendicular to the rotation axis [97,131]. Further, the general tendencies observed with DVC approaches are higher measurement uncertainties when compared with DIC [134,97]. When using regularized approaches, the levels could be reduced to those reached in 2D-DIC [122,214].

Let us note that there are few comparisons between local and global approaches to DVC [122, 137,169,93,168]. Overall, it is found that the measurement uncertainties are of the same order of magnitude when the total number of kinematic unknowns are similar. There is however an additional bonus for the standard displacement resolution (*i.e.,* of the order of 20% for hexahedra [122] and even higher for tetrahedra [93]) when the continuity requirement is enforced. The price to pay is related to the computation time that is higher.

In the sequel, some very recent results obtained for laminography are summarized. Contrary to tomography, the laminography technique [82,88] enables for in-situ imaging of studied regions in plate-like samples but involves incomplete sampling, which may increase the measurement uncertainty. Laminography is still a recent imaging technique [87,89]. Consequently, there is a

need for metrological assessment of the measured displacement fields and the corresponding strain fields [156,28]. The uncertainty levels are estimated by following the last presented method that includes multiple scans prior to the experiment itself:

- repeated scan - *bis*: two scans are acquired without any motion between the two acquisitions.
- rigid body motion - *rbm*: two scans are acquired when a rigid body motion is applied prior to the second acquisition. This case is deemed difficult [156] because the reconstruction artifacts (*e.g.,* rings) do not follow the motion and may severely bias the displacement measurements.

To assess the contribution induced by rigid body motions *bis* and *rbm* cases are compared. These effects will be probed for three different materials:

- aluminum alloy AA2139 grade (*i.e.,* Al-Cu-Mg alloy), with intermetallic volume fraction determined to be 0.45 % and an initial void volume fraction of 0.34 % (see Figure 2(a)). Two different heat treatments were studied [157,28], namely, T3 denotes the recrystallized state, solution heat-treated, stretched by between 2-4 % and naturally aged to obtain T351 (T3) condition. Conversely, T8 stands for the recrystallized state after an artificial aging treatment.
- aluminum alloy AA2198 grade (*i.e.,* Al-Cu-Li alloy), which has no initial porosity and 0.3 % volume fraction of metallic inclusions (see Figure 2(b)). Again, two different heat treatments (T3 and T8) have been studied [158,30,28].
- commercial nodular graphite cast iron (EN-GJS-400 [29,28,206]), which represents another class of materials with different microstructural length scales (Figure 2(c)).

The listed materials are analyzed by first conducting DVC analyses to measure displacement fields. The latter ones are interpolated to account for rigid body motions, both translations and rotations. The identified rigid body motions are then extracted from measured fields resulting in an estimation of the measurement errors [131]. The root mean square error associated with each displacement component is then computed, whose average σ_u will be reported for C8-DVC. The size ℓ of each C8 element is the length expressed in voxels of any edge. Different element

sizes are considered, namely, 16, 24, 32, 48 and 64-voxel elements. Figure 18 shows the standard displacement uncertainty as a function of the element size. In the figure, repeated scans (*i.e., bis* cases) are shown with solid lines while rigid body motion (*rbm*) cases are depicted with dashed lines.

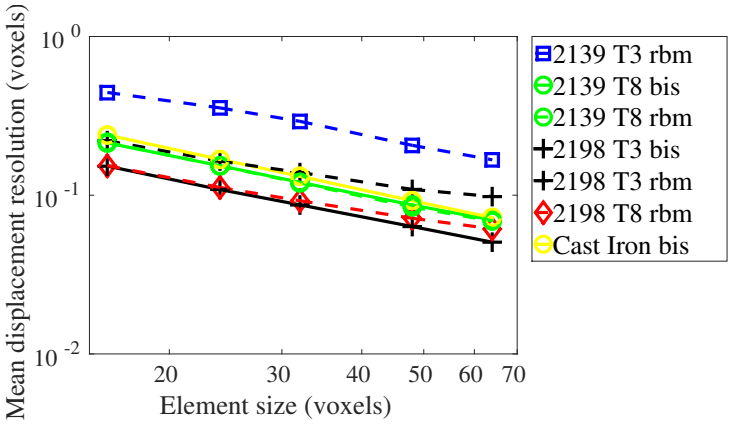

Fig. 18 Standard displacement uncertainty as function of the element size for the analyzed materials

These results illustrate the displacement uncertainty versus spatial resolution compromise to be made in DVC analyses [197,123,122], which is a signature of the ill-posedness of the underlying problem. It can be expressed by a power law relationship [197,131]

$$\sigma_u = \frac{A^{\alpha+1}}{\ell^{\alpha}} \tag{31}$$

where A is a constant expressed in voxels [131,156].

AA2198 T8 *bis* case has overall the lowest uncertainty values. The amount of rigid body in case of AA2198 T8 *rbm* is small and mainly in the direction of the rotation axis (*i.e.,* artificial rings do not move) and it can be considered as equivalent to a *bis* case. This is why AA2198 T3 *bis* and AA2198 T8 *rbm* results almost coincide. However, when larger rigid body motions are applied to the AA2198 microstructure, significant degradations occur as can be seen in the example of AA2198 T3 *rbm*.

Conversely, the AA2139 microstructure (with initial voids) is less affected by rigid body motions. AA2139 T8 *rbm* and AA2198 T3 *rbm* have almost identical size/position of the region of interest and amount of rigid body motion but still the relative gap between the corresponding *bis* and *rbm* cases are not identical. This case highlights an additional criterion concerning DVC uncertainty for laminography data, namely, its sensitivity to rigid body motions associated with the sample geometrical features (*e.g.,* notch, drilled holes, crack). According to these results, a microstructure with intermetallic particles only (*i.e.,* without voids and thus showing less contrast) is more sensitive to the detrimental effect of rigid body motions.

Even though cast iron represents another class of materials with different microstructural scales (Figure 2(c)) the reported displacement resolution virtually coincides with *bis* uncertainty levels for aluminum alloys. When compared to tomography resolutions [131] of the same type of material (cast iron) but not the same resolution (*i.e.,* side length of one voxel is 3.5 µm), laminography is more challenging than tomography since there is a difference of at least a factor of 3 between the two uncertainty levels [28].

When successful, DIC/DVC calculations yield gray level residuals reduced to the level of noise (*e.g.,* in the case of correlations between initial and artificially deformed initial images there is almost a one to one correspondence between the normalized RMS residual (by dynamic range Δf) and the dimensionless noise level $\sqrt{2}\sigma$ [99]). In the studied example (*bis* and *rbm* cases shown in Figure 18), the overall noise level (*i.e.,* acquisition and reconstruction) is unknown but can be estimated by the RMS value of the residual at convergence. Figure 19 shows the best and worst cases from Figure 18 normalized by the overall noise level calculated from the corresponding residual fields. When controlled by white Gaussian noise, nodal displacement uncertainties divided by the noise level are expected to follow a power law of the element size ℓ with an exponent $-3/2$ [122]. The results in Figure 19 show that this dependence is not observed. This may be due

to the occurrence of ring artifacts, which are observed in Figure 2 and which are clearly more significant than random noise for these cases.

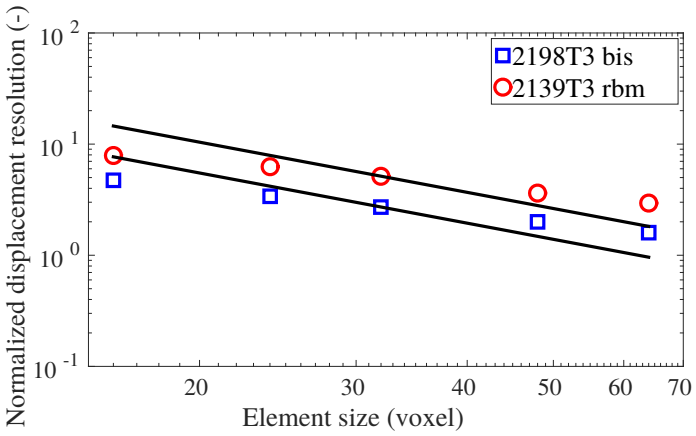

Fig. 19 Standard displacement uncertainty normalized by the (estimated) noise standard deviation as a function of the element size for the two aluminium alloys. The solid lines show $-3/2$ power laws that would be expected in the case of white Gaussian noise as controlling uncertainty. This seems not to be the case

In the present case, it appears that the uncertainty mainly comes from the laminography technique and its associated artifacts [88,238]. The uncertainty levels are equal or higher with rigid body motions since some of the artifacts are not attached to the microstructure (*e.g.,* phase-contrast edge enhancement) but intrinsic to the acquisition set-up (*e.g.,* ring artifacts). This result calls for caution and it is advisable to acquire at least two scans in the reference configuration, if possible by slightly moving the setup between the two acquisitions, to evaluate the practical displacement and strain resolutions of the studied material.

4.2 Theoretical study of projection noise

One important source of uncertainty (albeit not always dominant as seen in the previous examples) is the presence of noise in the images. This question, at least when the variance of noise is

low enough, can be treated on a theoretical ground using perturbation analyses. They provide quantitative estimates of the influence of noise on the kinematic analysis. This is important inasmuch as the obtained estimates of the full covariance matrix can be further used to evaluate the uncertainty of parameters identified with the measured displacement fields [165]. Moreover, the explicit expression of the covariance matrix on the measured degrees of freedom allows the "best" metric to be tailored in order to perform this identification step. Best is not just arrogant, but among all unbiased methods (and an infinite number of them exist), the "best" one refers to the one that delivers the sought parameters with the least uncertainty.

Before addressing the specific case of tomographic noise, let us first recall general DIC results that were obtained first for regular 2D-DIC [16, 99], but hold for all dimensionalities [122]. Let us consider that all images are corrupted by white and Gaussian noise, $\eta_f(\boldsymbol{x})$ and $\eta_g(\boldsymbol{x})$, for f and g respectively for the reference and deformed images (white in this context means that noise is spatially uncorrelated from pixel to pixel). The whiteness is not limiting and the same argument can be readily extended to an arbitrary spatial correlation. The Gaussian character is more limiting as it provides a very nice and comfortable stability property, namely, through linear operations (or through the linear tangent operators when the noise amplitude allows), noise will remain Gaussian, and hence the fluctuation of the measurement, here displacement fields, will also be Gaussian. Likewise the average of the noise being null, the obtained result will also be affected by a fluctuation whose expectation is null, which is to say the measurement is *un-biased*. Therefore, only variances are sufficient to characterize the noise-induced fluctuations of the result. When noise is non-Gaussian, it will tend to a Gaussian distribution, and the variance (and co-variances) are correctly computed with an argument based on Gaussian noise. However, higher order moments (that is 4th — or kurtosis — to start off with) have to be considered to see how close the measurement fluctuation is to a Gaussian distribution.

It can be noted that the situation is equivalent to the one where the noise affecting the reference image would be null and that of g would be an effective noise $\widetilde{\eta}_g = \eta_g - \eta_f$, white, Gaussian and of variance $2\sigma^2$, where σ^2 is that of each η_f or η_g. This observation gives an easier computation but the result does not depend on it. Introducing this noise in the images will induce an uncertainty $\{\delta \boldsymbol{u}\}$ in the measured displacement. The latter is formally evaluated by exploiting the computation of the displacement with successive corrections using the Newton's descend method. Equation (24) thus provides

$$\{\delta \boldsymbol{u}\} = [\boldsymbol{N}]^{\dagger}\{\widetilde{\boldsymbol{\eta}}_g\} \tag{32}$$

This linear relationship implies that the result is unbiased, $\langle\{\delta \boldsymbol{u}\}\rangle = 0$. The covariance matrix of this measurement noise is $[\boldsymbol{Cov}_u] = \langle\{\delta \boldsymbol{u}\}\{\delta \boldsymbol{u}\}^{\top}\rangle$ where the angular brackets designate the expected value. From the above expression, the covariance matrix becomes

$$\begin{aligned}
[\boldsymbol{Cov}_u] &= \langle [\boldsymbol{N}]^{\dagger}\{\widetilde{\boldsymbol{\eta}}_g\}\{\widetilde{\boldsymbol{\eta}}_g\}[\boldsymbol{N}]^{\dagger\top}\rangle \\
&= ([\boldsymbol{N}]^{\top}[\boldsymbol{N}])^{-1}[\boldsymbol{N}]^{\top}\langle\{\widetilde{\boldsymbol{\eta}}_g\}\{\widetilde{\boldsymbol{\eta}}_g\}\rangle[\boldsymbol{N}]([\boldsymbol{N}]^{\top}[\boldsymbol{N}])^{-1} \\
&= 2\sigma^2([\boldsymbol{N}]^{\top}[\boldsymbol{N}])^{-1}([\boldsymbol{N}]^{\top}[\boldsymbol{N}])([\boldsymbol{N}]^{\top}[\boldsymbol{N}])^{-1} \\
&= 2\sigma^2[\boldsymbol{M}]^{-1}
\end{aligned} \tag{33}$$

The above result is remarkably simple and compact [122]. What is particularly convenient is that the practical use of the above covariance matrix is to introduce a "metric tensor" (*i.e.,* Mahalanobis distance [140]) to appreciate a scalar product of such displacement fields as $\boldsymbol{u} \cdot \boldsymbol{v} = \{\boldsymbol{u}\}^{\top}[\boldsymbol{Cov}_u]^{-1}\{\boldsymbol{v}\}$. Hence, the appropriate norm to weigh the different degrees of freedom is written as $\|u\|^2 = 1/(2\sigma^2)\{\boldsymbol{u}\}^{\top}[\boldsymbol{M}]\{\boldsymbol{u}\}$, so that there is no need to invert the $[\boldsymbol{M}]$ matrix.

To illustrate this result, the three microstructures shown in Figure 2 are considered in order to assess their sensitivity to noise. For that purpose, the 100 largest eigenvalues of $[\boldsymbol{M}]^{-1}$ (*i.e.,* the lowest sensitivities of measured nodal displacements) for the studied microstructures and element size (ℓ=32 voxels) are shown in Figure 20. This information shows the isolated influence of the microstructure quality on the uncertainty. AA2198 T3 and T8 have higher eigenvalues than

AA2139 T3 and T8 although in the final uncertainty analysis the opposite trend is observed. The heat treatment (T3 or T8) does not play a significant role here. The grading that is observed from AA2198, the most prone to noise, to AA2139 intermediate and finally cast iron, showing the least sensitivity to noise, is consistent with the intuitive appreciation of the richness of the microstructure. However, it has been seen above that the effective level of displacement uncertainty was rather close for these three materials. To solve this apparent contradiction, let us mention that the above covariance is the product of $[\boldsymbol{M}]^{-1}$ by the noise variance $2\sigma^2$, and from Figure 2, it seems that the noise level is not equal in all three cases (AA2139 with its more favorable microstructure is also affected by a stronger noise than AA2198). Moreover, the noise affecting these images seems more due to ring artifacts than random noise. This observation underlines the importance of additional influences (*e.g.,* acquisition and reconstruction artifacts) on uncertainty.

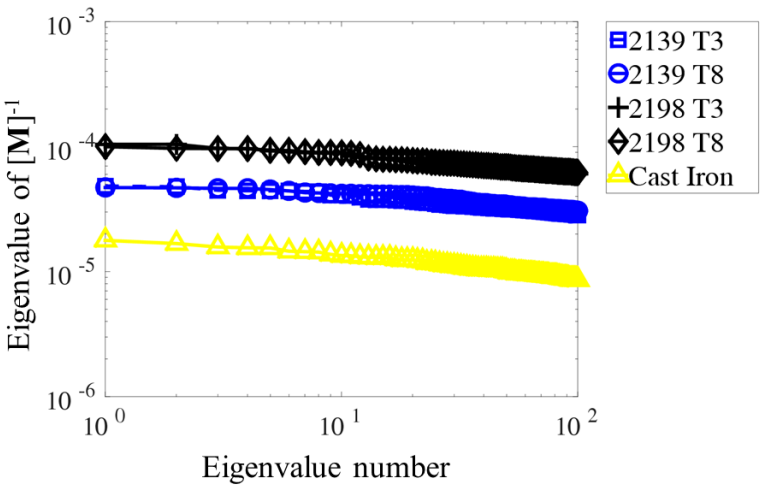

Fig. 20 The largest 100 eigenvalues of the inverse DVC matrix $[M]$ for the studied microstructures and element size ℓ=32 voxels

4.3 How white is white noise?

The above considerations work well for white noise. Such may be the case for the noise affecting radiographs, but the fact that the 3D volume is *computed* naturally introduces correlations in the volume and, ideally, this should be taken into account. Hence the following section aims at computing such correlations in the noise.

For the sake of simplicity, the case of parallel beam tomography is considered. 3D images, $f(\boldsymbol{x})$, are obtained from an inverse Radon transform of the projections $p(\boldsymbol{r}, \theta)$ [114]

$$f(\boldsymbol{x}) = \mathfrak{S}[p(\boldsymbol{r}, \theta)] \tag{34}$$

where $\boldsymbol{r}$ designates the coordinates in the detector space $\boldsymbol{r} = (r, z)$, z is parallel to the rotation axis, θ the angle of the sample for the projection, and p the projection, *i.e.,* the cologarithm of the ratio of the radiograph intensity at position $\boldsymbol{r}$ to the beam intensity (flat field) at the same point. For a parallel beam the different slices perpendicular to the z axis are uncoupled, and are treated independently. The inverse Radon transform consists of computing a convolution (along r) of the projection by $R(r)$

$$q_\theta(r, z) = R \star p(r, z, \theta) \tag{35}$$

where $\mathfrak{F}[R](\boldsymbol{k}) = |\boldsymbol{k}|$ is the so-called Ram-Lak filter [114]. The inverse Radon transform then reads

$$f(x, y, z) = \int_0^\pi q_\theta(x \sin(\theta) - y \cos(\theta), z) \, \mathrm{d}\theta \tag{36}$$

Let us assume a Gaussian white noise on projections

$$\langle \eta_p(\boldsymbol{r}, z) \eta_p(\boldsymbol{r}', z') \rangle = \sigma^2 \delta(\boldsymbol{r} - \boldsymbol{r}') \delta(z - z') \tag{37}$$

with a uniform variance σ^2. This noise in the projection, η_p, induces a noise in the reconstructed image, η_f, which has to be characterized. The linearity of the reconstruction implies that η_f is centered Gaussian noise as well. It is also to be observed, although this may be less intuitive, that

this noise is spatially stationary. In particular, the distance to the rotation axis plays no role. One way to show this property is to note that the rotation axis may be "moved" virtually by a mere translation of the different projections along r, by a quantity that depends on the angle θ. These translations have no effect on the image noise and hence no more on the reconstruction noise, from which stationarity results. Only the covariance of η_f is needed to fully characterize it

$$\langle \eta_f(\boldsymbol{x}) \eta_f(\boldsymbol{x}') \rangle = \sigma^2 \delta(z - z') \int_{\boldsymbol{r}} \mathfrak{S}[\delta(\boldsymbol{r} - \boldsymbol{x}, z)] \mathfrak{S}[\delta(\boldsymbol{r} - \boldsymbol{x}', z)] \mathrm{d}\boldsymbol{r} \tag{38}$$

Because of the decoupling of different z-slices and the statistical independence of the noise along the z axis, the resulting noise η_f is uncorrelated along the z direction. However, in the transverse, (x, y), plane, the spatial covariance of η_f has to be characterized.

It may be further noted that η_f is isotropic, so that the correlation function only depends on the relative distance between points $\boldsymbol{x}$ and $\boldsymbol{x}'$ (provided they lie in the same plane, $z = z'$), $\langle \eta_f(\boldsymbol{x}) \eta_f(\boldsymbol{x}') \rangle = C(|\boldsymbol{x} - \boldsymbol{x}'|)\delta(z - z')$ where $C(d)$ is the covariance of η_f for two points distant of d. The expression of $C(d)$ is more easily computed in Fourier space, as the power spectrum of η_p is uniform in the wavevector. The only subtlety comes from the denser sampling of noise close to the rotation axis, in Fourier space increasing the noise variance as $1/|\boldsymbol{k}|$, which is exactly compensated by the Ram-Lak filter. Hence, the power spectrum of noise in Fourier space is uniform, and the covariance reduces to a delta (Dirac) distribution in real space. Theoretically, in spite of the highly correlated steps involved in the inverse Radon transform (*i.e.,* the back-projection may appear to build up long-range correlations) the reconstructed image displays white noise. Thus, the appropriate similarity measure, as discussed in the previous section, reduces to that of quadratic differences.

However, in practice, the sampling of angles is not continuous, and some small scale details in the representation of voxels are always present. The effective noise is never actually white at the pixel scale, but displays a slight broadening and possibly anti-correlations that come from details of the implementation. If one wants however to see how good/bad the approximation of white

noise is, it is fairly easy to generate a series of projections that consists of uncorrelated Gaussian noise η_p with the very same format as the projections to be exploited, compute the inverse Radon transform of this noise with the used reconstruction code (one single slice is sufficient) and finally compute its pair correlation function. The latter usually departs slightly from the Dirac distribution, apart from nearest neighbor pixels that may display nonzero correlations.

4.4 Measurement biases and artifacts

In the previous sections, the roles of image noise, inter-voxel interpolation or displacement discretization were emphasized. However, other effects such as artifacts inevitably present in tomography may affect the image quality (or fidelity), and in turn possibly bias DVC results. This may be especially dangerous as the quality of image registration may not be at fault, but the interpretation of the results may reveal inappropriate. In the following, various artifacts of 3D imaging systems are discussed and ways to immunize DVC against these effects, and x-ray tomography (because of its dominance in 3D imaging) is the first technique that is considered.

4.4.1 Ring artifacts

Among classical artifacts, "rings" were already mentioned. This is a good illustration of the previous risk, namely when the material absorption coefficient is homogeneous, the main source of contrast in the reconstructed volume may be due to the artifactual rings. However, the latter are not bound to the material, and hence they do not move in the same way as the sample itself. Hence registration may provide displacement data such that rings are positioned on top of each other, that is for a null displacement, and not necessarily the actual one.

Very often the detector exhibits spatially random bias but that is steady in time (and hence in θ), $\eta_{\rm det}(r,z)$. (A similar effect may result from imperfect flat-fields.) Some tomographs now come with a translation of the detector during scan rotation, and these motions are then further

numerically corrected by a mere translation of the projection. This procedure averages out the bias for a large part, and the reconstructed volumes are typically of better quality. Otherwise these biases give rise to "rings" or "half-rings" depending on the spanned angles during the scan. For the aluminium alloys of Figure 2, rings are clearly visible. If the bias itself can be described as Gaussian noise in space, the resulting noise in the image now displays the same ring features in their spatial correlation.

This type of noise presents a nice case study for DVC. A first strategy is to introduce explicitly the possible bias, so that an acquired volume is written as

$$\hat{f}(x,y,z) = f(x,y,z) + \eta_r(\sqrt{x^2+y^2}, z) \tag{39}$$

and thus the DVC problem consists of the determination of both the kinematics *and* the detector bias η_{det}. To this aim, it is to be noted that the deformed image is affected by the same bias, but because of the deformation of the sample and its rigid body motions, the corrected image $\widetilde{g}_{\boldsymbol{u}}$ suffers from a "scrambled" version of this detector bias. The quadratic difference similarity measure thus takes a more complicated expression

$$\begin{aligned} S = \sum_{\boldsymbol{x}} \Big(& \hat{g}(x+u_x, y+u_y, z+u_z) - \hat{f}(x,y,z) \\ & - \eta_{\text{det}}(\sqrt{(x+u_x)^2+(y+u_y)^2}, z+u_z) + \eta_{\text{det}}(\sqrt{x^2+y^2}, z) \Big)^2 \end{aligned} \tag{40}$$

This expression looks like a difficult problem to tackle. However, it can be noted that the detector noise is assumed to be small, and hence one may solve the above minimization iteratively. More precisely, one may initialize the solution of the problem as in standard DVC, that is neglecting η_{det}. Once a first determination of the displacement has been estimated, one may obtain a first estimate of f, f_{est} and η_{det}, using first the average of the reference $\hat{f}$ and corrected deformed image $\widetilde{(\hat{g})}_{\boldsymbol{u}}$ as f_{est}, and from the difference $\hat{f} - f_{\text{est}}$, an angle-average provides an estimate for η_{det}. With the latter, a new estimation of both f_{est} and g_{est} is produced, from which DVC will refine the determination of the kinematics, and iteratively, better and better determinations of the bias and kinematics will be obtained.

Yet another possibility, if time allows, is to acquire several images of the sample without any mechanical loading, but only rigid body motions. In that case, it is rather straightforward to estimate this motion very precisely and the above procedure may provide a prior determination of η_{det} with very few iterations. Equipped with this determination, images can be pre-corrected before performing DVC, and the detector bias should no longer affect the results.

An alternative route is to devise a similarity measure that is unaffected by the detector bias. For instance, a projection operator, P, is introduced such that $g_f = P[f]$ and defined as

$$g_f(r,z) = \int_0^{\pi} f(r\cos(\theta), r\sin(\theta), z)\ \mathrm{d}\theta \tag{41}$$

and its complementary $h_f = Q[f]$

$$h(x,y,z) = f(x,y,z) - g_f(\sqrt{x^2+y^2}, z) \tag{42}$$

Because this linear operator filters out the detector noise as can be observed from $Q[\hat{f}] = Q[f]$ or $Q[\eta_{\text{det}}] = 0$, a similarity measure that is based on the quadratic norm of $Q[\hat{f} - \widetilde{(\hat{g})}_{\boldsymbol{u}}]$ can be considered. However, the projector Q is tuned to $\hat{f}$ but not to $\widetilde{(\hat{g})}_{\boldsymbol{u}}$, and hence this similarity measure is only an approximation. To mend this difficulty, η_{det} would have to be estimated in turn, correct $\hat{f}$ and $\hat{g}$ and iterate, and this would be equivalent to the previous route. As earlier mentioned for the discussion about the similarity measure, the most secure way to proceed is to explicitly describe the type of perturbation that affects the measurement, and determine all the parameters (and/or fields) that are involved in the measurement. This general rule allows the user to judge in the end whether the determined quantities (*i.e.,* both measurements of interest but also artifacts) are consistent with the prior knowledge (or at least assumptions) used to analyze the case under consideration.

4.4.2 Beam hardening

In lab tomographs, the x-ray source has generally a broad distribution of energies. X-ray absorption however depends on the frequency (or energy). Nevertheless, reconstruction softwares usually treat the beam as if it were monochromatic. The differential absorption of x-rays with wavelength means that as the ray penetrates into the solid, its spectrum concentrates onto the least absorbed frequencies, a phenomenon called "beam hardening." The consequence of beam hardening is that the outer layer of the sample will appear as being more absorbent than the core. Such an effect is however generally innocuous for DVC as it is a systematic effect that is attached to the sample. However, in some cases, beam hardening will be responsible for the formation of shadows behind a high or low density inclusion. These shadows are geometric effects that are of geometric origin and will not rotate with the sample. One should be extremely careful with such effects, and residuals should be examined carefully.

Let us note that when the material is made of a single phase (or when this provides a good approximation), it is possible to correct this beam-hardening effect with a procedure due to Herman [91] that consists of nonlinearly rescaling the gray levels.

4.4.3 Spurious motion during scan

Another difficulty comes from the possible motion of the specimen during one scan. This risk is reduced by the possibility of performing high-speed scans at synchrotron beamlines [32,143]. Yet because of an applied mechanical load during a scan, it is difficult to exclude motions due to viscous relaxation, or to delayed damage or plastic flow. In such cases, the reconstructed image appears to be blurred, and DVC may produce erroneous results or at least uncertain ones, prone to high noise. If residuals are not examined in details, such phenomena may go unnoticed. Similarly instead of the sample motion, it may be the rotation axis of the scan that does not remain steady.

These effects are common ones in tomography but the coupling of tomography with in-situ testing aggravates such risks.

Within the same type of artifacts, let us mention a last one due to the change in the source-sample distance in cone-beam setups in between the reference and the deformed image. Such a motion induces a magnification change that should not be interpreted in mechanical terms, especially for small strains [131, 233]. Micrometer-scale displacements of the source may induce a dilation that can easily be confused with a mechanical strain in terms of order of magnitude. As a consequence, an excellent thermal stability is required to prevent such spurious kinematics. Many recent lab systems have a thermal regulation that limits this bias. This last remark underlines the need for comprehensive analyses to fully assess the sources of measurement uncertainties. In Section 5.6, it will be seen that working directly with projections (*i.e.,* radiographs) rather than reconstructed volumes (via P-DVC [124]), first makes the problem less relevant because of the reduction in acquisition time that can be made drastic, and second opens the possibility of performing individual corrections on the projections.

4.4.4 OCT

For full-field Optical Coherence Tomography, the volume consists of a stack of images coming from successive depths within semi-transparent materials. Since no computation is needed to construct the volume, the sources of artifacts are much less numerous. However, as earlier mentioned, OCT is prone to noise, and moreover this noise is depth-dependent. In a similar spirit comes a specific feature of shadowing, namely, under a particle or feature that is a strong scatterer, the intensity of (coherent) light may be too small to permit the detection of further scatterers. If the motion of the sample moves a particle from a hidden to a visible position or vice-versa, registration may not provide a faithful account for motion. In such cases, which resemble the shadows cast by very absorbing features in x-ray tomography [229], a mask should be introduced, which would

correspond to the visible "horizon." Any variation that affects a position that is beyond the horizon should not be utilized. This may be compared to edge effects in classical DIC [99] when a feature present in the region of interest for the reference image is pushed outside the field of view in the deformed image, or conversely appears in the deformed image without being visible in the reference one. Using a frame to delineate a reliable ROI is a good strategy. The difficulty in the case of OCT is that the frame edge should be based on the total scattered intensity rather than being at fixed depth. Thus a direct modeling of OCT should be used to decide on the trusted part of the image and hence of the corresponding kinematics.

4.4.5 Conclusions

Many different modalities exist. Each one with its specific artifacts that, to some extent, can be modelled. It is through this modeling that progress can be made in the interpretation of the images so that artifacts, rather than being a limitation with uncontrolled consequences, can be tamed to be as transparent as possible to DVC analyses, even if not taken into consideration in the reconstruction of 3D images.

5 Challenges

5.1 Material microstructure

The first generic difficulty with 3D imaging is that the actual microstructure of the material can hardly be modified in the bulk in order to enhance contrast. Some attempts were made (*e.g.,* by adding particles [18,77,25,146] or revealing grain boundaries [135] for x-ray µCT) but at the expense of changing the behavior of the investigated material. This is particularly true when studying ductile of brittle fracture [94]. Model materials were also considered for which the attenuation contrast was sufficient [207,69]. Natural materials such as wood (thanks to its cellular

microstructure) enabled DVC analyses to be successfully performed [68,70]. Similarly, low density wood fiberboards could be studied via DVC [222].

This is a major difference with 2D DIC, where a homogeneous or transparent material can always be painted with a speckle pattern, where the experimentalist can fine-tune the homogeneity, pattern correlation length, and contrast more or less at will. In synchrotron facilities, the use of phase contrast can enhance the differences between material phases, and make them visible on the x-ray radiographs. Variants of this technique can be used on lab scale tomograph with polychromatic sources. Thus, this difficulty pushes DVC to deal with microstructures that can be very faint, with very few contrasting phases, possibly with a contrast that is not very salient as compared to reconstruction artifacts (Figure 2). Robustness when dealing with such sparse contrast textures is a major challenge that limits *a priori* the recourse to DVC for well contrasted materials (*e.g.,* biological tissues [209,12,199,195,194,242], foams [207,197] and cellular materials [68]) or material with a large proportion of inclusions [127,69,133]. It is worth noting that even for very low contrasted materials such as aluminum alloys, DVC analyses were shown to be feasible [156] and yielded strain fields whose analysis was very precious in the understanding of the flat-to-slant transition in ductile tearing [158,157].

The occurrence of reconstruction artifacts (such as rings) becomes very detrimental when the contrast due to the natural microstructure of the material is as poor as discussed previously (see Sections 4.1 and 4.4). It is therefore very important to address these cases in order to make DVC useful for a broader class of materials. Let us stress that if numerically filtering images prior to a DVC analysis (*e.g.,* ring artifacts can be significantly reduced [183]) is always an option, it is safer to include this filter in the similarity measure, or to leave as an unknown the effect to be filtered out, in order to validate the consistency of the assumption(s) made, and check that the filter did not affect the true microstructure. Last, let us note that when some information is

discarded and still an acceptable spatial resolution is sought, suited regularization strategies are very helpful [199, 102, 195, 115, 123, 122].

5.2 DVC algorithms

DVC calculations are becoming very involved even for local approaches because of the large size of volumes to be registered. A critical aspect is related to the initialization of the DVC code. One strategy used in local DVC is the global starting point and the information transfer approach. The locations of displacement measurement are ordered by the distance from a global starting point. That point is given special handling, possibly with user intervention. Transferring results to nearby points creates reliable starting points for the final optimization steps.

Multiscale approaches, as discussed in Section 3.3 are a very convenient way for initialization purposes. Such schemes speed up the DVC calculations, and more importantly, they often prevent the DVC code to be trapped in secondary minima. This type of strategy is particularly important when dealing with large deformations [197, 97]. An alternative route is to start DVC calculations with large sub-volumes or elements and gradually refine [74] by initializing the new calculations with the previously converged solution. In the case of large deformations, there is always the possibility of updating the reference configuration, which becomes the deformed configuration of the previous calculation. So-called incremental DVC procedures have been implemented [103, 30, 157]. It is worth remembering that displacement fields have then to be interpolated in order to have access to cumulative displacement fields. Special care should be taken when computing strain fields, in particular in the large transformation framework (*i.e.,* depending on the type of updating strategy, Lagrangian or Eulerian strain descriptors will be computed [223]). Alternatively, the mesh can be advected in order to make the nodes follow the same material points.

The computation of the deformed volume corrected by the current estimate of the displacement field requires gray level interpolations to be performed for all voxels belonging to the ROI, and

more than once for local approaches with overlapping subvolumes. The algorithms being iterative, such operations are repeated numerous times. To avoid such repeated interpolations lookup tables can be pre-computed [170] in order to accelerate DVC runs.

Local approaches have been shown to scale well when parallelized using multiple CPUs and multiple CPU threads. Likewise, these approaches are a natural fit for the massively multi-threaded computation power of graphics processing units (GPUs) [122, 7, 75, 235]. Since DVC is usually concerned with very large data sets, the number of measured kinematic degrees of freedom are generally numerous. For global DVC it has been proposed to describe displacement fields in separated forms for spatial dimensions. Such a specific form can be introduced in the formalism of DIC/DVC, retaining only the dominant mode repeatedly until the residual level has been exhausted [80]. This way of handling the problem is written within the framework of PGD [39, 120] in which the different modes are introduced and the separated form is inserted directly in the variational formulation of DVC. Another route may be provided by domain decomposition methods applied to DVC. It has been followed in DIC analyses [176], but was not yet applied to DVC. However, because most of the computation cost is related to the correction by the measured displacement field of the deformed volume the CPU time gain is not spectacular, up to now, in comparison with standard implementations. When optimized global frameworks also scale nearly perfectly for multi-threading [121]. This is achieved by grouping voxels locally and sending each group to a different CPU thread.

Four dimensional analyses, namely, performing DVC analyses over space *and* time have begun very recently [93]. Time regularization will have some interest provided a sufficient number of scans is available in the analysis. It will also make the calculations even more involved and some of the above routes may turn out to be very useful (*e.g.,* PGD [165]). It is believed that projection-based approaches are more suitable since they precisely provide much more temporal information than using fully reconstructed volumes at different levels of load.

5.3 Identification and validation

The *validation* of material models using tomographic data still is in its infancy (see Section 3.4). This first step is already very challenging for various reasons. First, in-situ (or ex-situ) testing is not yet performed routinely. The fact that more and more labs are equipped with in house tomographs will democratize experiments in such environments. Second, DVC itself has to be mastered in the case of difficult to very difficult microstructures (*e.g.,* with small volume fractions of secondary phases [156, 158]). The simulations at the scale of 3D images are also very demanding in particular when nonlinear constitutive laws are selected.

Figure 21 illustrates one possible route to validate numerical simulations at the microscale. Once sets of tomographic data are available (or by any other 3D imaging means), they can be used first to create meshes that are made compatible with the underlying microstructure revealed by 3D imaging [144]. When such meshes are created, finite element simulations can be run. However, there is still no control on their predictive character. The latter can be assessed by comparing computed displacement fields with their measured counterparts (via DVC). The distance between these two fields, when probed with respect to the measurement uncertainties, enables for *relative* comparisons between experimental and simulated data, the true solution being unknown. One additional step is to prescribe the measured boundary conditions to the numerical model. As underlined in Section 3.4, such approach is crucial in the validation step [206]. More importantly, it allows gray level residuals to be assessed not only for standard DVC analyses, but also for numerical simulations [29]. These residuals can be evaluated *independently* for DVC and numerical simulations. The two approaches are therefore probed individually and their merits (and shortcomings) are assessed in an absolute manner.

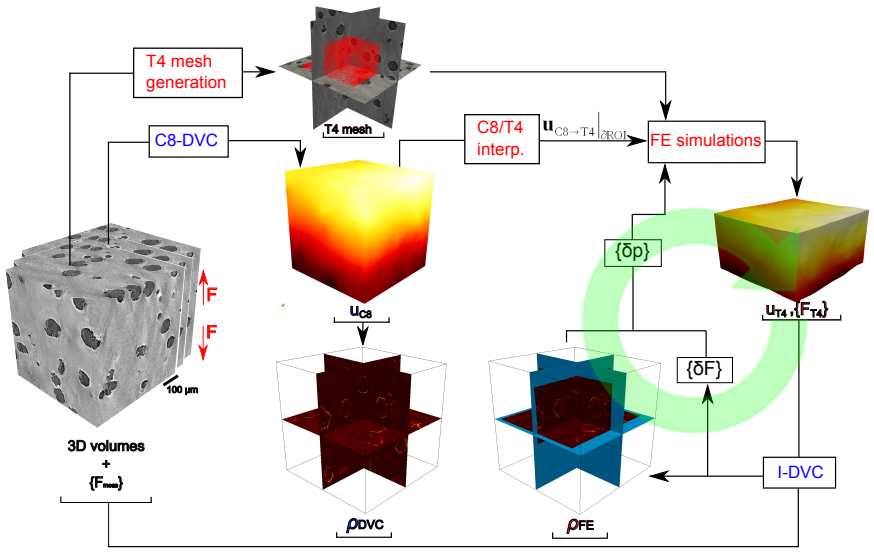

Fig. 21 Schematic representation of methods that can be used for validation and identification purposes via numerical simulations at the microscale (adapted from Ref. [29])

Identification, which is the next step when validation is deemed insufficient, requires the use of numerous simulations in order to calibrate (or update) parameters of material models (Figure 21). Many identification techniques have now reached a reasonable degree of maturity in simpler situations (*e.g.,* when using DIC data [5,83]), which makes them good candidates to be tested in the context of DVC analyses. Yet they are challenged more severely in the context of 3D imaging because of generally higher measurement uncertainties in comparison with regular DIC. This observation may explain why very few studies have, up to now (see Section 3.4), been devoted to such endeavors.

The simulations become very demanding when microstructures are described very finely thanks to tomographic data (*i.e.,* tomography or laminography typically give access to Gvoxel-volumes). For instance, each reconstructed volume can be obtained from a set of $6,000 \times 12$-Mpixel radiographs (*i.e.,* 144 Gbytes per considered step for 16-bit digitizations). For in-situ experiments the

typical number of scans now routinely exceeds ten, which leads to more than 1 Tbyte of data for a single experiment. The mere handling and visualization of such enormous amounts of data becomes challenging. Further, their processing is also becoming tedious. Model/data reduction strategies are one possible route to follow in order to ease and make the exploitation of such experimental data far more efficient [165]. Similarly, much more developments should be performed regarding time and memory savings.

5.4 4D kinematic measurements from fast tomography

One direction for addressing the challenge of resolving small time intervals has already been discussed in the introduction. Stupendous progress has been achieved in ultra-fast tomography scanned at synchrotron beamlines. Even crack propagation followed at 20 Hz showed the potential of such techniques for mechanical properties of materials. However, surprisingly, very few published studies made use of DVC to translate microstructure changes into 4D displacement (or velocity) fields. One exception though is due to one team that studied lithium batteries in operando [178, 65]. In these examples, DVC could inform on the strains, and hence ageing conditions under electrochemical changes, and finally provided a clear picture of the performance loss of such batteries.

It is nowadays a safe bet that fast tomography will open new avenues in experimental mechanics. Yet this remains for the most part a virgin and unexplored land. It is worth noting that as the turntable rotates faster, it may induce vibrations, thereby inducing additional artifacts (due to spurious motions) that will need to be accounted for at the reconstruction stage.

This hardware progress is however not an answer to the avalanche of data produced by in-situ experiments. On the contrary, this is an excellent way of generating more data in a short time. In the remaining part of this section different directions are listed, which give solid hopes on ways to actually decrease the needed experimental data, and hence achieve a better efficiency but not from

a better accumulation of data. The different proposed routes deal with the ability to compress information with no (or a very modest) loss that have been proposed in the recent years. The first one, Section 5.5, aims at reducing the number of projections for reconstructing a tomographic volume, at the expense of formulating simple but generic assumptions on the microstructure. The second one, Section 5.6, is focussed on the displacement field and makes use of model reduction strategies, also devised initially to compress information with as little loss as possible, and with a control of the quality of the "reduction" performance.

5.5 Volume data / duration of acquisition

One limitation comes from the enormous amount of information in 3D images. This challenge is first met at the acquisition stage where a complete scan may require up to one hour or more in some cases, duration such that creep/relaxation may be responsible for a significant motion between the first and last radiographs. Thus one may be tempted to under-sample the orientations and collect fewer projections. The latter option is extremely appealing as it allows for much faster data acquisitions. However, without additional care, such an option generally involves very pronounced artifacts that differ from one reconstruction to the next and thereby compromise DVC.

However, numerous studies following the seminal contribution of Candès *et al.* [34] have shown that the use of some regularization strategies (and in particular the minimization of the total variation, TV) can compensate for the missing information when very few projections are acquired and provide excellent reconstructions. The key to the formidable success of such methods is the exploitation of some sparsity in the description of the to-be-reconstructed material. For instance, the chosen test case for the initial illustration of the benefit of TV-regularization was the Shepp-Logan phantom, a simple mathematical model of an idealized brain image, composed of few "phases," so that the boundary of those different phases, where the total variation is non-zero,

was indeed sparse. And this sparsity is favored by using an L1 norm of the gradient (*i.e.,* the total variation, TV), yet preserving convexity of the problem.

The reliability of such approaches for medical diagnostics has sometimes been questioned [92] since, in this field in particular, it is essential to guarantee that the prior information brought by the regularization is valid (for instance, the presence of smooth gradients would invalidate this approach). Yet, the remarkable success of TV-regularization cannot be ignored, as having only few phases in a material is quite common. Some care is to be exercised, in order to apply such an approach, and in particular, correcting beam hardening is essential as this effect introduces a gradual change of gray levels from the boundary to the bulk of the sample, an effect that is not compatible with a discrete set of gray levels.

Operationally, a very elegant method, Discrete Algebraic Reconstruction Technique (or DART), has been proposed by Batenburg and Sijbers [9,10]. It consists of coupling an algebraic reconstruction technique (SIRT) with a filtering of the reconstructed field in order to meet a constraint on the existence of a given number of phases (say only two for a binary reconstruction). The beauty of this algorithm is that it focuses only on the region in the image where some uncertainty remains and capitalizes the more secure determinations. Moreover, because of the interweaving of these two steps (SIRT and filtering), the approach has a rather low intrusiveness. Finally, DART has been also enriched with TV-regularization (TVR-DART), which adds some "surface tension" at interfaces [244]. Such an algorithm has the potential to achieve a very accurate reconstruction with a limited number of projections.

One may fear that as the number of projections is reduced, the reconstructed volume will display progressively more uncertainty in its microstructure. Actually, this is not quite the case. When the quality of the reconstruction is studied versus the number of projections, it is observed that the problem displays an abrupt "phase transition," from a solvable problem where the reconstruction quality is very good to an unsolvable problem, where no solution is obtained [53].

It is difficult to theoretically qualify this abrupt transition, and determine the minimum number of projections required to reconstruct a solution, as it depends on the quantity of information present in the object to be reconstructed, and hence also on the additional information bought about by the regularization. However, even a very conservative estimate allows several orders of magnitude to be gained in acquisition time.

In the safe convergence side, even if too little information is available for classical reconstruction, it is important to note that each projection has a proper spatial resolution, and hence in order to achieve a proper match of the reconstructed volume with the available projections, an accurate determination of the microstructure features is called for. Therefore, the degradation of the reconstruction quality should not be imagined to be a progressive fuzziness of the boundaries (this would be forbidden by regularization). Rather, a more appropriate schematic picture is that the reconstruction is either excellent, or simply inaccessible. To the best of the authors' knowledge, the combination of regularized reconstruction, say using TVR-DART, and DVC has never been attempted (at least in published form). Such an association appears intuitively adverse to the usual requirement for accuracy. However, for the above mentioned reasons, intuition may not be of safe guidance. The above suggestion is a mere speculation at this stage.

5.6 Projection-based DVC: fast 4D kinematic measurement

The proposed approach to deal with fast 4D (space and time) measurement is called Projection-based Digital Volume Correlation (P-DVC) [124, 213]. Instead of working with reconstructed volumes as in standard DVC (whose acquisition time is one of the major limitation of CT, especially in laboratory facilities), it aims to measure the 4D displacement field from the comparison of a series of 2D projections (*i.e.,* the projection at an angle $\theta(t)$ of the 3D microstructure) acquired at different times, t, angles, $\theta(t)$) and loadings $F(t)$. One reference 3D volume (using classical means) is assumed to be available in order to compute the correction term.

The similarity measure is here the squared difference of projections (since a white Gaussian noise is generally valid for projections). One set of projections is that of the deformed volumes $p(\boldsymbol{r}, t)$ at different loading steps (just one projection per loading step) and the other one is the corresponding projected reference image corrected by the displacement field, $\boldsymbol{u}$. Registration (P-DVC) consists of minimizing this similarity measure

$$\mathfrak{T}_{\mathrm{PDVC}}[\boldsymbol{u}] = \sum_{\boldsymbol{r},t} \Big(\mathfrak{P}_{\theta(t)}[f(\boldsymbol{x} - \boldsymbol{u}(\boldsymbol{x}, t))] - p(\boldsymbol{r}, t) \Big)^2 \tag{43}$$

where $\mathfrak{P}_\theta$ is the projection operator in the direction of angle $\theta(t)$, and $\boldsymbol{r}$ the detector coordinate.

As for usual DVC, in order to validate the procedure, the 2D residual field shows what has not been captured by the kinematic model (*e.g.,* noise, artifacts of the detector, poor convergence, model error). It is defined as

$$\rho(\boldsymbol{r}, t; \boldsymbol{u}) = \mathfrak{P}_{\theta(t)}[f(\boldsymbol{x} - \boldsymbol{u}(\boldsymbol{x}, t))] - p(\boldsymbol{r}, t) \tag{44}$$

5.6.1 Space-time regularization

It is proposed to analyze the deformation of a sample using a reduced basis composed of N_s space shape functions $\boldsymbol{\phi}(\boldsymbol{x})$ (*e.g.,* from a finite element mesh) and N_t time functions $\chi(t)$ (*e.g.,* Dirac distribution if no temporal regularization (free) is considered, polynomials, piecewise linear, or of higher degree)

$$\boldsymbol{u}(\boldsymbol{x}, t) = \sum_{i=1}^{N_t} \sum_{j=1}^{Ns} u_{ij} \chi_i(t) \boldsymbol{\phi}_j(\boldsymbol{x}) \tag{45}$$

where u_{ij} are the amplitudes of the displacement field associated with the chosen basis. Note that the time basis also offers the opportunity to include the time history coming from another modality. For instance, in the present case, a force measurement, $F(t)$, is available. If the sample were linearly elastic, $F(t)$ would be naturally relevant. One can also hybridize different signals (*e.g.,* force and time), and any nonlinear functions thereof.

In the case of a large number of unknowns, the computation of the $N_s \times N_t$ degrees of freedom may be costly. The so-called DIC-PGD framework has been developed to directly extract the dominant displacement modes (using space [175,80] or space-time [111] separation) and provides big savings. However, for the sake of simplicity, this option is not followed herein. The minimization of $\mathfrak{T}_{\mathrm{PDVC}}$ with respect to the displacement parameters $\{\boldsymbol{u}\}$ is performed using Newton's descent method. This procedure requires the computation of the gradient and Hessian of $\mathfrak{T}_{\mathrm{PDVC}}$. They are built from the sensitivities

$$s_{ij}(\boldsymbol{r},t) = \mathfrak{P}_{\theta(t)}[\chi_i(t)\boldsymbol{\phi}_j(\boldsymbol{x}) \cdot \boldsymbol{\nabla}\widetilde{f}_{\boldsymbol{u}}(\boldsymbol{x})] \tag{46}$$

where $\widetilde{f}_{\boldsymbol{u}}(\boldsymbol{x})$ is the reference volume advected with the current (Eulerian) determination of the displacement field $\boldsymbol{u}$, $\widetilde{f}_{\boldsymbol{u}}(\boldsymbol{x}) = f(\boldsymbol{x}-\boldsymbol{u}(\boldsymbol{x},t))$. (Note that in contrast with the previous presentation DVC, the reference image is to be advected to match the deformed volume projections, as only the latter is known, and not the deformed volume itself.) After each evaluation of the displacement corrections, or equivalently of its parameterization, $\{\delta\boldsymbol{u}\}$ from a known displacement $\{\boldsymbol{u}\}^{(n)}$ such as $\{\boldsymbol{u}\}^{(n+1)} = \{\boldsymbol{u}\}^{(n)} + \{\delta\boldsymbol{u}\}$, a correction of the 3D volume is performed so that the previous equation is used *without approximation*. The Hessian of $\mathfrak{T}_{\mathrm{PDVC}}$ with respect to $\{\boldsymbol{u}\}$ and the right hand side vector are written as

$$\begin{aligned} N_{ijkl} &= \sum_{\boldsymbol{r},t} s_{ij}(\boldsymbol{r},t)s_{kl}(\boldsymbol{r},t) \\ n_{ij} &= \sum_{\boldsymbol{r},t} \left(\mathfrak{P}_{\theta(t)}[\widetilde{f}(\boldsymbol{x})_{\boldsymbol{u}}] - p(\boldsymbol{r},t)\right) s_{ij}(\boldsymbol{r},t) \end{aligned} \tag{47}$$

and thus one iteration is obtained by solving the following linear problem

$$[\boldsymbol{N}]\{\delta\boldsymbol{u}\} = \{\boldsymbol{n}\} \tag{48}$$

5.6.2 Experimental test case

The test case for this study is an in-situ tensile test on a ductile cast iron sample. The geometry of the sample is shown in Figure 22(a). (Similar samples were studied in Refs. [219,93].) The

central part (rectangular cross section of 1.31×0.91 mm^2) is thinned with a radius of 20 mm in order to ensure that the specimen will fail in the ligament area and not in the grips. The sample, which was mounted in an in-situ tensile testing machine similar to that used by Buffière *et al.* [26] (Figure 22(b)), was scanned at LMT's lab-tomograph (180 kV, 130 µA, W target) at full resolution was equal to 10.4 µm.

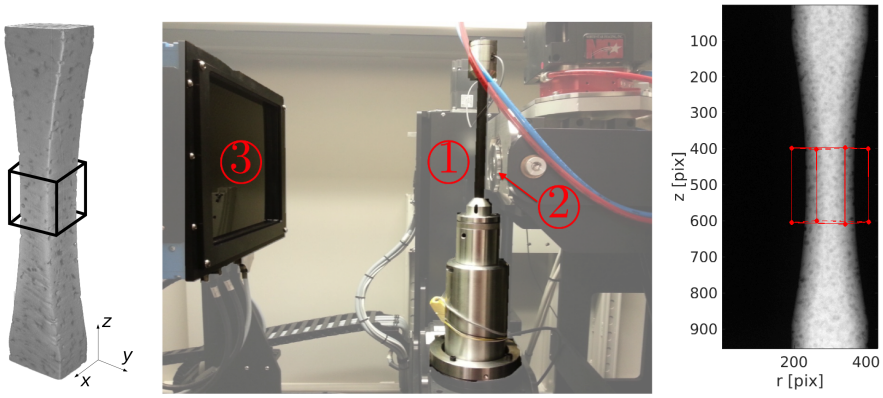

(a) (b) (c)

Fig. 22 In-situ tensile test with (a) the dog-bone sample used in the procedure with the regularization element, (b) the setup with ① the testing machine with the carbon fiber composite loading tube, ② the x-ray source, ③ the x-ray detector, and (c) a projection of the sample at angle $\theta_k = -150^\circ$ for step 110 with the projected spatial degrees of freedom

Two flat-fields and one dark-field were acquired after conditioning and before the experiment in order to perform flat-field corrections. Each radiograph was averaged over 5 frames in order to reduce acquisition noise. The radiographs were cropped to a definition of 954×432 pixels so as to concentrate on the central part of the sample. The projections were obtained after flat-field normalization and standard beam hardening corrections with a third order polynomial [91] due to the high absorption of cast iron. Reconstructions and projections were performed with the

ASTRA toolbox [227] making use of the Feldkamp-Davis-Kress (FDK) reconstruction procedure suited for cone beams [61].

The in-situ experiment consisted of three phases:

- pre-load to 250 N in order to remove the backlash that would introduce rigid body motions;
- complete scan of the reference state (250 N) that consisted of 600 radiographs captured at equally spaced angles ranging over a full 360° revolution. This scan took about 22 min. to be acquired;
- continuous rotation of the sample with 50 acquisitions per revolution. 127 loading steps were captured during 300 s. The first 50 steps (*i.e.,* 1 full rotation) were performed at constant load and were used to quantify the uncertainty. The remaining (starting from time step 50) were carried out with a continuous load change (from 250 to 750 N), which was controlled at a constant stroke rate of 2 µm/s.

The force measurement is shown in Figure 23 and could be used for future identification purposes.

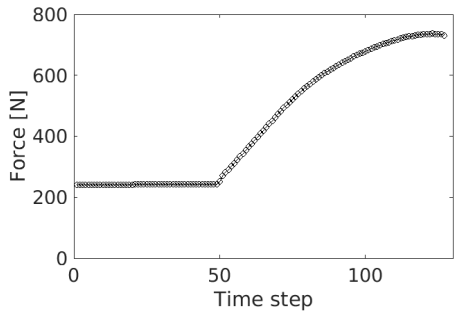

Fig. 23 127 force measurements of the tensile test starting from 250 N. A first complete revolution is performed at constant load, and the load is subsequently increased up to failure. The reference tomographic scan is acquired just before time 0.

5.6.3 Results of the 4D spatiotemporal procedure

It is proposed to focus on the central part of the sample where large plastic strains are expected. A first evaluation of the transverse mean rigid body motions (*i.e.,* perpendicular to the tensile axis) that occurred during the test is performed before displacement measurement. These rigid body motions are corrected from the projections. (This part is not detailed but it uses the same philosophy as previously presented).

Because the behavior is expected to be that of a plastic hinge (*i.e.,* uniform displacement in the top and bottom part of the sample and large strains in the center), the chosen space regularization for the vertical displacement is to use one single element (with 8 nodes of size $200 \times 200 \times 200$ voxels), each composed of a single degree of freedom, vertical displacement, with inside a trilinear interpolation, *i.e.,* a reduced version of a C8 element where transverse displacements are neglected (since the mean transverse translation has already been corrected, this assumption neglects the transverse strains). In the top and bottom parts, the (uniform) displacement is chosen as a constant extension from the central cube face by continuity. The element is located in the central part as shown in Figure 22(a).

The time regularization is based on second order polynomials of the force measurement. A linear interpolation starting at time step 0 is added and another linear function with 0 value during time step [0,49] and linear during the load increase part

$$\begin{aligned} \chi_1(t) &= 1 \\ \chi_2(t) &= F(t) \\ \chi_3(t) &= F(t)^2 \\ \chi_4(t) &= t \\ \chi_5(t) &= \max(0, (t-49)) \end{aligned} \tag{49}$$

The 4D problem is composed of 40 degrees of freedom (*i.e.,* 5 time and 8 space shape functions, χ and ϕ respectively) and focuses on the region of interest corresponding to the projected cube

element. Figure 24 shows the residual field change before and after registration. The residuals are rescaled to the dynamic range of the reference projection. It can be seen that a large part of the residual has been erased meaning that the kinematics has been well captured.

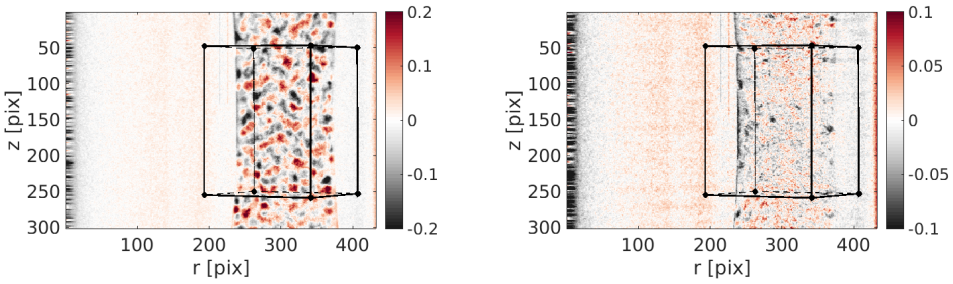

(a) (b)

Fig. 24 Projected residual field at angle $\theta_k = -150^\circ$ for step 110 (a) with no displacement field correction and (b) after the correction of the measured displacement. The black lines are the projections of the central cube element. Note that the gray level color bar (where gray levels are scaled to the full projection dynamic range) differs by a factor 2

The measured displacement for the 8 nodes at each loading step is shown in Figure 25(a). At the end of the experiment, the cube has been stretched in tension by about 11 voxels, or about 110 µm. The gray level residual is quantified, in the region of interest (see Figure 25(b)), by the signal to noise ratio (SNR). The raw difference of projections leads to an SNR of 11.0 dB. The periodicity of about 25 time steps, which is seen in the initial residual, corresponds to the angles where the edges of the sample are aligned with the x-ray beam, namely, where the sensitivity to the radial displacement field is high. After the transverse translation correction, it increases to 23.4 dB. Finally, when the axial strain is accounted for as above described, the SNR reaches 26.8 dB.

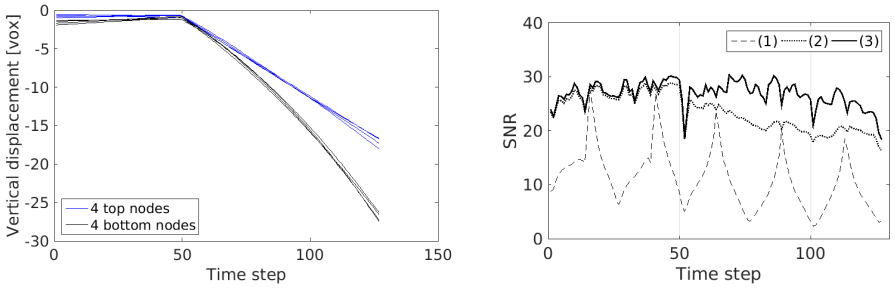

(a) (b)

Fig. 25 (a) Measured displacement of the 8 nodes. During the first revolution ($t \leq 50$) a slight compression is visible, which is attributed to a relaxation phenomenon. In the increasing load part, the central region is stretched by approximately 11 voxels (or 110 µm). (b) SNR history for the initial residual fields (1), the residuals corrected by (x, y) rigid body translations (2), and the final residual fields with all corrections (3)

The 3D displacement for the 127 loading steps has been captured. Run in 300 s, this 4D procedure based on radiographs offers a fast measurement of the experiment with a gain of three orders of magnitude as compared to standard techniques. The entire procedure, including the experiment itself (after the initial tomography of the reference volume) and its analysis, is performed in approximately 10-15 minutes. A more complex and refined mesh could be used in order to characterize the kinematics more thoroughly. However, in order to avoid the increase of the number of degrees of freedom, regularization based on a mechanical model or other experimental observations would be welcome. Moreover, in 4D analyses, a proper generalized decomposition (PGD) approach is an alternative to focus on the most relevant modes and helps keeping the number de degrees of freedom at a decent level [111].

5.6.4 Perspectives

The above example showed that a tremendous potential exists either to save time for getting the same information, or rather, to increase the time resolution at the same experimental time cost. Such a gain is obtained from a better definition of what is known and what is not, starting from

the ultimate goal (*e.g.,* mechanical properties), and progressively assembling from the accessible experimental data and the modeling a complete picture. Moreover, even if redundancy is reduced, as the primary information itself (*i.e.,* the set of radiographs) has been severely deflated, it remains high enough to validate the assumed prior knowledge from residuals.

Stepping back to get a broader perspective, it is worth underlining the parallel that can be drawn in the two previous sections 5.5 and 5.6:

- The former aimed at reconstructing the 3D microstructure from few projections, and required the introduction of prior knowledge on microstructure to allow for reconstruction with too few projections using standard tools.
- The latter aimed at reconstructing the 3D kinematic field from few projections, and required the introduction of prior knowledge on the mechanical behavior to allow for reconstruction with too few projections using standard tools.

In both of these sections, more than two orders of magnitude gains were achieved on complex and realistic examples. It is to be stressed how remarkable is such a progress. Very few fields of research have experienced such a fantastic and sudden advance. Moreover, this huge gain did not originate from better equipments or facilities, but rather from a more intricate use of modeling and experiment. Such improvements are believed to be more the rule than the exception, and hence it is a unique opportunity for such 4D analyses to give a major impetus to the field of mechanics of materials (and structures).

6 Summary

Over the last two decades, DVC has been made operational and reliable for very large classes of materials, wider than originally considered, and together with the progress of tomography and more generally 3D imaging modalities, it is today a very powerful experimental technique serving

in particular the field of mechanics of materials. Commercial codes are now available, for local and global approaches, which makes DVC a tool that does not necessarily require the user to implement their own code. Further, the technique is gradually adopted by industry in the fields of nondestructive evaluation and mechanics of materials. This trend will require good practices to be formalized and possibly standards to be introduced.

During the present decade, 3D imaging has been made more easily accessible thanks to the development of lab tomographs. X-ray microtomography has become the 3D microscope that enables mechanical tests to be performed in-situ. Coupled with DVC, they give access to a wealth of information that will enable progress in the understanding of material microstructures and their changes, as well as their mechanical behavior. One critical aspect is the way 3D images are reconstructed, and all the artifacts associated with the acquisition process during mechanical tests. DVC is a very powerful tool to reveal them and even propose some corrections. These observations call for careful and systematic uncertainty and bias quantifications that not only depend on the contrast in the images but also on the physical and mathematical processes involved in their reconstructions.

In order to explicitly account for acquisition noise, different similarity measures were discussed. They provide a probabilistic framework to image registration, which is not limited to DVC. It was shown how local and global approaches could be retrieved from such a framework. Further, the reconstructed volumes essentially display white noise properties (provided the radiographs themselves do) so that minimization criteria based on the sum of the squared differences are quasi optimal in terms of their least sensitivity to acquisition noise.

Ex-situ and more often in-situ tests have become a growing area in the field of solid mechanics. Commercial (*i.e.,* general purpose) testing systems are now available. The specific conditions associated with 3D imaging means will require the experimentalist to more often design their own loading devices in order to be compatible with the testing environment. Two options are possible.

First the testing machine (and the sample) is put on the turntable of the imaging system. Second, the imaging system is built around testing machines (as the patient in a medical scanner). This second route is more delicate, but not impossible, when the protection to radiation has been carefully implemented.

In the majority of reported results so far, (local or global) DVC was used as a stand-alone technique that measures displacement fields. Strain fields are then deduced from the raw (displacement) measurements. This operation has to be well-mastered and understood since interpolations are required and remain usually implicit for the user. Even though such fields are prevalent for mechanical analyses, special care is to be exercised in their interpretation, in particular, in terms of uncertainties and associated correlations. Both kinematic fields carry a lot of information on the experiment per se and on its mechanical interpretation. When the user does not want to add a priori information, these general purpose codes provide a lot of qualitative and quantitative information about the test of interest. Until the end of the last decade, it was the only way DVC was used [11].

More recently, it has been shown that measured data can also be integrated in numerical simulations and vice versa. The introduction of mechanical modeling in the measurement procedure from regularization techniques is also a very powerful way of continuously tuning discretization effects of the kinematics and simultaneously shaking hands with the further exploitation of kinematic data for mechanical behavior identification. As stressed through various examples, residual fields are very precious to validate all the assumptions used in DVC measurements, and to assess whether the partition between "explained" data, noise and artifacts is satisfactory. In such approaches DVC is not a stand-alone tool, but one link out of many forming a chain between in-situ mechanical testing and mechanical identification and validation.

Further broadening the range of applications will require in situ experiments to be performed faster and possibly uninterrupted. Currently, lab tomographs require acquisition times lasting at

least tens of minutes, which means that the load and displacement have to remain constant in order to ensure good reconstructions. Thanks to the beam power of third generation synchrotrons, subsecond scans are possible with the use of high speed cameras. However, spinning the sample and the loading device faster will inevitably reduce the quality of reconstructions if spurious motions are not accounted for. Another route is provided by spacetime analyses in which radiographs will be acquired on the fly. The latter ones will rely on projection-based DVC. It is envisioned that such techniques will open a new era of 4D tests that are performed in similar ways as conventional mechanical tests. This development will also imply new DVC implementations and maturing that couple reconstructions and displacement measurements.

The benefit of all the above mentioned approaches (be they local, global, regularized or integrated) is huge, and all methods and tools are readily available for the blossoming of 4D in-situ mechanical tests. These 4D analyses are now facing the massive amount of data to be processed efficiently, and that comes together with the impressive development of tomographic facilities and lab equipments. Unique opportunities were also mentioned, coming in particular from applied mathematics through concepts in the vein of "compressed sensing" [35,52] or tools such as "model reduction" [4].

Acknowledgements Different parts of the above mentioned examples were funded by Agence Nationale de la Recherche under the grants ANR-10-EQPX-37 (MATMECA), ANR-14-CE07-0034-02 (COMINSIDE), Saint Gobain, SAFRAN Aircraft Engines and SAFRAN Tech. It is a pleasure to acknowledge the support of BPI France within the DICCIT project, and ESRF for MA1006, MI1149, MA1631,MA1932, and ME1366 experiments.

Fruitful discussions with Profs. Marc Bernacki, Claude Boccara, Pierre-Olivier Bouchard, Jean-Yves Buffière, Stephen Hall, Per-Lennart Larsson, Eric Maire, Cino Viggiani, and Drs. Jérôme Adrien, Edward Andó, Dominique Bernard, Xavier Brajer, René Gy, Lukas Helfen, Thilo Morgeneyer, Amir Nahas, Estelle Parra, Mehdi Rebai, Julien Schneider are acknowledged.

References

1. J. Adam, M. Klinkmueller, G. Schreurs, and B. Wieneke. Quantitative 3D strain analysis in analogue experiments simulating tectonic deformation: Integration of X-ray computed tomography and digital volume correlation techniques. *JOURNAL OF STRUCTURAL GEOLOGY*, 55:127–149, 2013.
2. R.J. Adrian. Twenty years of particle image velocimetry. *EXPERIMENTS IN FLUIDS*, 39:159–169, 2005.
3. E. Andò, S. Hall, G. Viggiani, J. Desrues, and P. Bésuelle. Experimental micromechanics: grain-scale observation of sand deformation. *GÉOTECHNIQUE LETTERS*, 2(3):107–112, 2012.
4. A.C. Antoulas, D.C. Sorensen, and S. Gugercin. A survey of model reduction methods for large-scale systems. *CONTEMPORARY MATHEMATICS*, 280:193–220, 2001.
5. S. Avril, M. Bonnet, A.S. Bretelle, M. Grédiac, F. Hild, P. Ienny, F. Latourte, D. Lemosse, S. Pagano, E. Pagnacco, and F. Pierron. Overview of identification methods of mechanical parameters based on full-field measurements. *EXPERIMENTAL MECHANICS*, 48(4):381–402, 2008.
6. J. Banhart, A. Borbély, K. Dzieciol, F. Garcia-Moreno, I. Manke, N. Kardjilov, A. R. Kaysser-Pyzalla, M. Strobl, and W. Treimer. X-ray and neutron imaging–Complementary techniques for materials science and engineering: Dedicated to Professor Dr. H.-P. Degischer on the occasion of his 65th birthday. *INTERNATIONAL JOURNAL OF MATERIALS RESEARCH*, 101(9):1069–1079, 2010.
7. E. Bar-Kochba, J. Toyjanova, E. Andrews, K.-S. Kim, and C. Franck. A Fast Iterative Digital Volume Correlation Algorithm for Large Deformations. *EXPERIMENTAL MECHANICS*, 55(1):261–274, 2015.
8. J. Baruchel, J.Y. Buffière, E. Maire, P. Merle, and G. Peix, editors. *X-Ray Tomography in Material Sciences*. Hermès Science, Paris (France), 2000.
9. K. J. Batenburg and J. Sijbers. DART: a fast heuristic algebraic reconstruction algorithm for discrete tomography. In *IEEE International Conference on Image Processing (ICIP 2007)*, volume 4, pages IV–133, 2007.
10. K. J. Batenburg and J. Sijbers. DART: a practical reconstruction algorithm for discrete tomography. *IEEE TRANSACTIONS ON IMAGE PROCESSING*, 20(9):2542–2553, 2011.
11. B.K. Bay. Methods and applications of digital volume correlation. *JOURNAL OF STRAIN ANALYSIS FOR ENGINEERING DESIGN*, 43(8):745–760, 2008.
12. B.K. Bay, T.S. Smith, D.P. Fyhrie, and M. Saad. Digital volume correlation: Three-dimensional strain mapping using X-ray tomography. *EXPERIMENTAL MECHANICS*, 39(3):217–226, 1999.
13. E. Beaurepaire, A.C. Boccara, M. Lebec, L. Blanchot, and H. Saint-Jalmes. Full-field optical coherence microscopy. *OPTICS LETTERS*, 23(4):244–246, 1998.

14. A. Benoit, S. Guérard, B. Gillet, G. Guillot, F. Hild, D. Mitton, J.-N. Périé, and S. Roux. 3D analysis from micro-MRI during in situ compression on cancellous bone. *JOURNAL OF BIOMECHANICS*, 42(14):2381–2386, 2009.

15. H. Berek, U. Ballaschk, C.G. Aneziris, K. Losch, and K. Schladitz. The correlation of local deformation and stress-assisted local phase transformations in MMC foams. *MATERIALS CHARACTERIZATION*, 107:139–148, 2015.

16. G. Besnard, F. Hild, and S. Roux. "Finite-element" displacement fields analysis from digital images: Application to Portevin-Le Chatelier bands. *EXPERIMENTAL MECHANICS*, 46:789–803, 2006.

17. T. Bormann, G. Schulz, H. Deyhle, F. Beckmann, M. de Wild, J. Kueffer, C. Muench, W. Hoffmann, and B. Mueller. Combining micro computed tomography and three-dimensional registration to evaluate local strains in shape memory scaffolds. *ACTA BIOMATERIALIA*, 10(2):1024–1034, 2014.

18. M. Bornert, J.-M. Chaix, P. Doumalin, J.-C. Dupré, T. Fournel, D. Jeulin, E. Maire, M. Moreaud, and H. Moulinec. Mesure tridimensionnelle de champs cinématiques par imagerie volumique pour l'analyse des matériaux et des structures. *INSTRUMENTATION, MESURE, MÉTROLOGIE*, 4:43–88, 2004.

19. G. Borstnar, F. Gillard, M.N. Mavrogordato, I. Sinclair, and S.M. Spearing. Three-dimensional deformation mapping of Mode I interlaminar crack extension in particle-toughened interlayers. *ACTA MATERIALIA*, 103:63–70, 2016.

20. A. Bouterf, J. Adrien, E. Maire, X. Brajer, F. Hild, and S. Roux. Failure Mechanisms of Plasterboard in Nail Pull Test Determined by X-ray Microtomography and Digital Volume Correlation. *EXPERIMENTAL MECHANICS*, 56(8):1427–1437, 2016.

21. A. Bouterf, J. Adrien, E. Maire, X. Brajer, F. Hild, and S. Roux. Identification of the crushing behavior of brittle foam: From indentation to oedometric tests. *JOURNAL OF THE MECHANICS AND PHYSICS OF SOLIDS*, 98:181–200, 2017.

22. A. Bouterf, E. Maire, S. Roux, F. Hild, X. Brajer, E. Gouillart, and E. Boller. Analysis of compaction in brittle foam with multiscale indentation tests. Submitted for publication, 2017.

23. A. Bouterf, S. Roux, F. Hild, J. Adrien, E. Maire, and S. Meille. Digital Volume Correlation Applied to X-ray Tomography Images from Spherical Indentation Tests on Lightweight Gypsum. *STRAIN*, 50(5):444–453, 2014.

24. A.I. Bowler, B.W. Drinkwater, and P.D. Wilcox. An investigation into the feasibility of internal strain measurement in solids by correlation of ultrasonic images. *PROCEEDINGS OF THE ROYAL SOCIETY A-MATHEMATICAL PHYSICAL AND ENGINEERING SCIENCES*, 467(2132):2247–2270, 2011.

25. R. Brault, A. Germaneau, J.-C. Dupré, P. Doumalin, S. Mistou, and M. Fazzini. In-situ Analysis of Laminated Composite Materials by X-ray Micro-Computed Tomography and Digital Volume Correlation. *EXPERIMENTAL MECHANICS*, 53(7):1143–1151, 2013.
26. J.-Y. Buffière, E. Maire, J. Adrien, J.-P. Masse, and E. Boller. In Situ Experiments with X-ray Tomography: an Attractive Tool for Experimental Mechanics. *EXPERIMENTAL MECHANICS*, 50(3):289–305, 2010.
27. J.Y. Buffière, E. Maire, P. Cloetens, G. Lormand, and R. Fougères. Characterisation of internal damage in a MMCp using X-ray synchrotron phase contrast microtomography. *ACTA MATERIALIA*, 47(5):1613–1625, 1999.
28. A. Buljac. *Understanding, observation and quantification of ductile failure mechanisms via 3D imaging*. PhD thesis, Université Paris-Saclay, 2017.
29. A. Buljac, M. Shakoor, J. Neggers, M. Bernacki, P.-O. Bouchard, L. Helfen, T.F. Morgeneyer, and F. Hild. Numerical validation framework for micromechanical simulations based on synchrotron 3D imaging. *COMPUTATIONAL MECHANICS*, 59(3):419–441, 2017.
30. A. Buljac, T. Taillandier-Thomas, T.F. Morgeneyer, L. Helfen, S. Roux, and F. Hild. Slant strained band development during flat to slant crack transition in AA 2198 T8 sheet: in situ 3D measurements. *INTERNATIONAL JOURNAL OF FRACTURE*, 200(1-2):49–62, 2016.
31. A. Buljac, V.-M. Trejo Navas, M. Shakoor, A. Bouterf, J. Neggers, M. Bernacki, P.-O. Bouchard, T.F. Morgeneyer, and F. Hild. On the Feasibility of Calibration of Elastoplastic Parameters at the Microscale via X-Ray Microtomography and Digital Volume Correlation for the Simulation of Ductile Damage. Submitted for publication, 2017.
32. B. Cai, S. Karagadde, L. Yuan, T.J. Marrow, T. Connolley, and P.D. Lee. In situ synchrotron tomographic quantification of granular and intragranular deformation during semi-solid compression of an equiaxed dendritic Al-Cu alloy. *ACTA MATERIALIA*, 76:371–380, 2014.
33. B. Cai, P.D. Lee, S. Karagadde, T.J. Marrow, and T. Connolley. Time-resolved synchrotron tomographic quantification of deformation during indentation of an equiaxed semi-solid granular alloy. *ACTA MATERIALIA*, 105:338–346, 2016.
34. E. J. Candès, J. Romberg, and T. Tao. Robust uncertainty principles: Exact signal reconstruction from highly incomplete frequency information. *IEEE TRANSACTIONS ON INFORMATION THEORY*, 52(2):489–509, 2006.
35. E.J. Candès, J. Romberg, and T Tao.
36. D.C. Champeney. *A Handbook of Fourier Theorems*. Cambridge University Press, Cambridge (UK), 1987.

37. Y. Chen, E. Dall'Ara, E. Sales, K. Manda, R. Wallace, P. Pankaj, and M. Viceconti. Micro-CT based finite element models of cancellous bone predict accurately displacement once the boundary condition is well replicated: A validation study. *JOURNAL OF THE MECHANICAL BEHAVIOR OF BIOMEDICAL MATERIALS*, 65:644–651, 2017.

38. F.-P. Chiang and L. Mao. Development of interior strain measurement techniques using random speckle patterns. *MECCANICA*, 50(2):401–410, 2015.

39. F. Chinesta, A. Ammar, and E. Cueto. Recent advances and new challenges in the use of the proper generalized decomposition for solving multidimensional models. *ARCHIVES OF COMPUTATIONAL METHODS IN ENGINEERING*, 17(4):327–350, 2010.

40. C. Choudhari, R. Herblum, M.K. Akens, S. Moore, M. Hardisty, and C.M. Whyne. Post-euthanasia micro-computed tomography-based strain analysis is able to represent quasi-static in vivo behavior of whole vertebrae. *PROCEEDINGS OF THE INSTITUTION OF MECHANICAL ENGINEERS PART H-JOURNAL OF ENGINEERING IN MEDICINE*, 230(9):900–904, 2016.

41. J.L. Colliat-Dangus, J. Desrues, and P. Foray. Triaxial testing of granular soil under elevated cell pressure. In R.T. Donaghe, R.C. Chaney, and M.L. Silver, editors, *Advanced Triaxial Testing of Soil and Rock*, volume STP 977, pages 290–310. American Society for Testing and Materials, Philadelphia, 1988.

42. J.W. Cooley and J.W. Tuckey. An algorithm for the machine calculation of complex fourier series. *MATHEMATICS OF COMPUTATION*, 19(90):297–301, 1965.

43. B. Coudrillier, I.C. Campbell, A.T. Read, D.M. Geraldes, N.T. Vo, A. Feola, J. Mulvihill, J. Albon, R.L. Abel, and C.R. Ethier. Effects of Peripapillary Scleral Stiffening on the Deformation of the Lamina Cribrosa. *INVESTIGATIVE OPHTHALMOLOGY & VISUAL SCIENCE*, 57(6):2666–2677, 2016.

44. B. Coudrillier, D.M. Geraldes, N.T. Vo, R. Atwood, C. Reinhard, I.C. Campbell, Y. Raji, J. Albon, R.L. Abel, and C.R. Ethier. Phase-Contrast Micro-Computed Tomography Measurements of the Intraocular Pressure-Induced Deformation of the Porcine Lamina Cribrosa. *IEEE TRANSACTIONS ON MEDICAL IMAGING*, 35(4):988–999, 2016.

45. N. Dahdah, N. Limodin, A. El Bartali, J.-F. Witz, R. Seghir, E. Charkaluk, and J.-Y. Buffière. Damage Investigation in A319 Aluminium Alloy by X-ray Tomography and Digital Volume Correlation during In Situ High-Temperature Fatigue Tests. *STRAIN*, 52(4):324–335, 2016.

46. E. Dall'Ara, D. Barber, and M. Viceconti. About the inevitable compromise between spatial resolution and accuracy of strain measurement for bone tissue: A 3D zero-strain study. *JOURNAL OF BIOMECHANICS*, 47(12):2956–2963, 2014.

47. V. Danesi, G. Tozzi, and L. Cristofolini. Application of digital volume correlation to study the efficacy of prophylactic vertebral augmentation. *CLINICAL BIOMECHANICS*, 39:14–24, 2016.

48. G.R. Davis and J.C. Elliot. Artefacts in x-ray microtomography of materials. *MATERIALS SCIENCE AND ENGINEERING*, 22(9):1011–1018, 2006.

49. J. Desrues and E. Andò. Strain localisation in granular media. *COMPTES RENDUS PHYSIQUE*, 16(1):26–36, 2015.

50. J. Desrues, R. Chambon, M. Mokni, and F. Mazerolle. Void ratio evolution inside shear bands in triaxial sand specimens studied by computed tomography. *GÉOTECHNIQUE*, 46(3):529–546, 1996.

51. J. Desrues, G. Viggiani, and P. Bésuelle, editors. *Advances in X-ray Tomography for Geomaterials*. Wiley / ISTE, London (UK), 2006.

52. D. L. Donoho. Compressed sensing. *IEEE TRANSACTIONS ON INFORMATION THEORY*, 52(4):1289–1306, 2006.

53. D. L. Donoho, A. Maleki, and A. Montanari. The noise-sensitivity phase transition in compressed sensing. *IEEE TRANSACTIONS ON INFORMATION THEORY*, 57(10):6920–6941, 2011.

54. A. Dubois and L. Vabre. Ultrahigh-resolution OCT using white-light interference microscopy. In *Optical Methods and Optical Coherence Tomography in Biomedicine VII*, volume 4956, pages 14–22. International Society for Optics and Photonics, 2003.

55. D.S. Eastwood, V. Yufit, J. Gelb, A. Gu, R.S. Bradley, S.J. Harris, D.J.L. Brett, N.P. Brandon, P.D. Lee, P.J. Withers, and P.R. Shearing. Lithiation-Induced Dilation Mapping in a Lithium-Ion Battery Electrode by 3D X-Ray Microscopy and Digital Volume Correlation. *ADVANCED ENERGY MATERIALS*, 4(4):1300506, 2014.

56. J.A. Elliott, A.H. Windle, J.R. Hobdell, G. Eeckhaut, R.J. Oldman, W. Ludwig, E. Boller, P. Cloetens, and J. Baruchel. In-situ deformation of an open-cell flexible polyurethane foam characterised by 3d computed microtomography. *JOURNAL OF MATERIALS SCIENCE*, 37(8):1547–1555, 2002.

57. G.E. Elsinga, F. Scarano, B. Wieneke, and B.W. van Oudheusden. Tomographic particle image velocimetry. *EXPERIMENTS IN FLUIDS*, 41(6):933–947, 2006.

58. H.W. Engl, M. Hanke, and A. Neubauer. *Regularization of Inverse Problems*. Kluwer, Dordrecht (the Netherlands), 1996.

59. R. Fedele, A. Ciani, and F. Fiori. X-ray microtomography under loading and 3D-volume digital image correlation. A review. *FUNDAMENTA INFORMATICAE*, 135(1-2):171–197, 2014.

60. R. Fedele, A. Ciani, L. Galantucci, M. Bettuzzi, and L. Andena. A regularized, pyramidal multi-grid approach to global 3D-volume digital image correlation based on X-ray micro-tomography. *FUNDAMENTA INFORMATICAE*, 125(3-4):361–376, 2013.

61. L.A. Feldkamp, L.C. Davis, and J.W. Kress. Practical cone beam algorithm. *JOURNAL OF THE OPTICAL SOCIETY OF AMERICA*, A1:612–619, 1984.

62. X. Feng, M.S. Hall, M. Wu, and C.-Y. Hui. An adaptive algorithm for tracking 3D bead displacements: application in biological experiments. *MEASUREMENT SCIENCE AND TECHNOLOGY*, 25(5):055701, 2014.

63. F. Figueroa Pilz, P.J. Dowey, A.-L. Fauchille, L. Courtois, B. Bay, L. Ma, K.G. Taylor, J. Mecklenburgh, and P.D. Lee. Synchrotron tomographic quantification of strain and fracture during simulated thermal maturation of an organic-rich shale, UK Kimmeridge Clay. *JOURNAL OF GEOPHYSICAL RESEARCH-SOLID EARTH*, 122(4):2553–2564, 2017.

64. T. Fila, O. Jirousek, A. Jung, and I. Kumpova. Identification of strain fields in pure Al and hybrid Ni/Al metal foams using X-ray micro-tomography under loading. *JOURNAL OF INSTRUMENTATION*, 11:C11017, NOV 2016.

65. D.P. Finegan, E. Tudisco, M. Scheel, J.B. Robinson, O.O. Taiwo, S. Eastwood, P.D. Lee, M. Di Michiel, B. Bay, S.A. Hall, G. Hinds, D.J.L. Brett, and P.R. Shearing. Quantifying Bulk Electrode Strain and Material Displacement within Lithium Batteries via High-Speed Operando Tomography and Digital Volume Correlation. *ADVANCED SCIENCE*, 3(3):1500332, 2016.

66. G. Fischer, J. Nellesen, N.B. Anar, K. Ehrig, H. Riesemeier, and W. Tillmann. 3D analysis of microdeformation in VHCF-loaded nodular cast iron by µCT. *MATERIALS SCIENCE AND ENGINEERING A-STRUCTURAL MATERIALS PROPERTIES MICROSTRUCTURE AND PROCESSING*, 577:202–209, 2013.

67. T. G. Flohr, C. H. McCollough, H. Bruder, M. Petersilka, K. Gruber, C. Süβ, M. Grasruck, K. Stierstorfer, B. Krauss, R. Raupach, et al. First performance evaluation of a dual-source ct (dsct) system. *EUROPEAN RADIOLOGY*, 16(2):256–268, 2006.

68. F. Forsberg, R. Mooser, M. Arnold, E. Hack, and P. Wyss. 3D micro-scale deformations of wood in bending: Synchrotron radiation µCT data analyzed with digital volume correlation. *JOURNAL OF STRUCTURAL BIOLOGY*, 164(3):255–262, 2008.

69. F. Forsberg and C.R. Siviour. 3D deformation and strain analysis in compacted sugar using x-ray microtomography and digital volume correlation. *MEASUREMENT SCIENCE AND TECHNOLOGY*, 20(9):095703, 2009.

70. F. Forsberg, M. Sjodahl, R. Mooser, E. Hack, and P. Wyss. Full Three-Dimensional Strain Measurements on Wood Exposed to Three-Point Bending: Analysis by Use of Digital Volume Correlation Applied to Synchrotron Radiation Micro-Computed Tomography Image Data. *STRAIN*, 46(1):47–60, 2010.

71. C. Franck, S. Hong, S. A. Maskarinec, D. A. Tirrell, and G. Ravichandran. Three-dimensional full-field measurements of large deformations in soft materials using confocal microscopy and digital volume correlation. *EXPERIMENTAL MECHANICS*, 47(3):427–438, 2007.

72. J. Fu, M. Haghighi-Abayneh, F. Pierron, and P.D. Ruiz. Depth-Resolved Full-Field Measurement of Corneal Deformation by Optical Coherence Tomography and Digital Volume Correlation. *EXPERIMENTAL MECHANICS*, 56(7):1203–1217, 2016.

73. J. Fu, F. Pierron, and P.D. Ruiz. Elastic stiffness characterization using three-dimensional full-field deformation obtained with optical coherence tomography and digital volume correlation. *JOURNAL OF BIOMEDICAL OPTICS*, 18(12):121512, 2013.

74. M. Gates, J. Gonzalez, J. Lambros, and M.T. Heath. Subset Refinement for Digital Volume Correlation: Numerical and Experimental Applications. *EXPERIMENTAL MECHANICS*, 55(1):245–259, 2015.

75. M. Gates, M.T. Heath, and J. Lambros. High-performance hybrid CPU and GPU parallel algorithm for digital volume correlation. *INTERNATIONAL JOURNAL OF HIGH PERFORMANCE COMPUTING APPLICATIONS*, 29(1):92–106, 2015.

76. M. Genet, L.C. Lee, and S. Kozerke. *A continuum finite strain formulation of the equilibrium gap regularizer for finite element image correlation.* CSMA, http://hal.archives-ouvertes.fr/hal-01661810/, 2017.

77. A. Germaneau, P. Doumalin, and J.-C. Dupré. 3D strain field measurement by correlation of volume images using scattered light: Recording of images and choice of marks. *STRAIN*, 43(3):207–218, 2007.

78. A. Germaneau, F. Peyruseigt, S. Mistou, P. Doumalin, and J.-C. Dupré. 3D mechanical analysis of aeronautical plain bearings: Validation of a finite element model from measurement of displacement fields by digital volume correlation and optical scanning tomography. *OPTICS AND LASERS IN ENGINEERING*, 48(6):676–683, 2010.

79. F. Gillard, R. Boardman, M. Mavrogordato, D. Hollis, I. Sinclair, F. Pierron, and M. Browne. The application of digital volume correlation (DVC) to study the microstructural behaviour of trabecular bone during compression. *JOURNAL OF THE MECHANICAL BEHAVIOR OF BIOMEDICAL MATERIALS*, 29:480–499, 2014.

80. L.A. Gomes Perini, J.-C. Passieux, and J.-N. Périé. A Multigrid PGD-based Algorithm for Volumetric Displacement Fields Measurements. *STRAIN*, 50(4):355–367, 2014.

81. S. Gondrom and S. Schropfer. Digital computed laminography and tomosynthesis — functional principles and industrial applications. *JOURNAL OF NONDESTRUCTIVE TESTING & ULTRASONICS*, 7(2), 1999.

82. S. Gondrom, J. Zhou, M. Maisl, H. Reiter, M. Kröning, and W. Arnold. X-ray computed laminography: an approach of computed tomography for applications with limited access. *NUCLEAR ENGINEERING AND DESIGN*, 190(1):141–147, 1999.

83. M. Grédiac and F. Hild, editors. *Full-Field Measurements and Identification in Solid Mechanics*. ISTE / Wiley, London (UK), 2012.

84. J.-P. Guillet, B. Recur, L. Frederique, B. Bousquet, L. Canioni, I. Manek-Hönninger, P. Desbarats, and P. Mounaix. Review of terahertz tomography techniques. *JOURNAL OF INFRARED, MILLIMETER, AND TERAHERTZ WAVES*, 35(4):382–411, 2014.

85. A. Guvenilir, T.M. Breunig, J.H. Kinney, and Stock S.R. Direct observation of crack opening as a function of applied load in the interior of a notched tensile sample of al-li2090. *ACTA MATERIALIA*, 45:1977–1987, 1997.

86. S. Hall, M. Bornert, J. Desrues, Y. Pannier, N. Lenoir, C. Viggiani, and P. Bésuelle. Discrete and continuum analysis of localised deformation in sand using x-ray micro ct and volumetric digital image correlation. *GÉOTECHNIQUE*, 60(5):315–322, 2010.

87. L. Helfen, T. Baumbach, P. Mikulík, D. Kiel, P. Pernot, P. Cloetens, and J. Baruchel. High-resolution three-dimensional imaging of flat objects by synchrotron-radiation computed laminography. *APPLIED PHYSICS LETTERS*, 86(7):071915, 2005.

88. L. Helfen, A. Myagotin, P. Mikulík, P. Pernot, A. Voropaev, M. Elyyan, M. Di Michiel, J. Baruchel, and T. Baumbach. On the implementation of computed laminography using synchrotron radiation. *REVIEW OF SCIENTIFIC INSTRUMENTS*, 82(063702), 2011.

89. L. Helfen, A. Myagotin, A. Rack, P. Pernot, P. Mikulík, M. Di Michiel, and T. Baumbach. Synchrotron-radiation computed laminography for high-resolution three-dimensional imaging of flat devices. *PHYSICA STATUS SOLIDI (a)*, 204:2760–2765, 2007.

90. L. Helfen, F. Xu, H. Suhonen, L. Urbanelli, P. Cloetens, and T. Baumbach. Nano-laminography for three-dimensional high-resolution imaging of flat specimens. *JOURNAL OF INSTRUMENTATION*, 8(05):C05006, 2013.

91. G.T. Herman. Correction for beam hardening in computed tomography. *PHYSICS IN MEDICINE AND BIOLOGY*, 24(1):81, 1979.

92. G.T. Herman and R. Davidi. Image reconstruction from a small number of projections. *INVERSE PROBLEMS*, 24(045011), 2008.

93. F. Hild, A. Bouterf, L. Chamoin, F. Mathieu, J. Neggers, F. Pled, Z. Tomičević, and S. Roux. Toward 4D Mechanical Correlation. *ADVANCED MODELING AND SIMULATION IN ENGINEERING SCIENCES*, 3(17):1–26, 2016.

94. F. Hild, A. Bouterf, and S. Roux. Damage measurements via DIC From physical to mechanical damage. *INTERNATIONAL JOURNAL OF FRACTURE*, 191(1-2):77–105, 2015.

95. F. Hild, A. Fanget, J. Adrien, E. Maire, and S. Roux. Three-dimensional analysis of a tensile test on a propellant with digital volume correlation. *ARCHIVES OF MECHANICS*, 63(5-6):459–478, 2011.

96. F. Hild, H. Leclerc, S. Roux, N. Swiergiel, and Z. Tomičević. Circumventing the Curse of Resolution versus Spatial Resolution in Digital Image Correlation: From Local to Global and Regularized Approaches. In *IUTAM symposium on Advances of Optical Methods in Experimental Mechanics*, 2012.

97. F. Hild, E. Maire, S. Roux, and J.-F. Witz. Three dimensional analysis of a compression test on stone wool. *ACTA MATERIALIA*, 57:3310–3320, 2009.

98. F. Hild, B. Raka, M. Baudequin, S. Roux, and F. Cantelaube. Multi-scale displacement field measurements of compressed mineral wool samples by digital image correlation. *APPLIED OPTICS*, IP 41(32):6815–6828, 2002.

99. F. Hild and S. Roux. Comparison of local and global approaches to digital image correlation. *EXPERIMENTAL MECHANICS*, 52(9):1503–1519, 2012.

100. F. Hild and S. Roux. Digital image correlation. In P. Rastogi and E. Hack, editors, *Optical Methods for Solid Mechanics. A Full-Field Approach*, pages 183–228. Wiley-VCH, Weinheim (Germany), 2012.

101. F. Hild, S. Roux, D. Bernard, G. Hauss, and M. Rebai. On the use of 3D images and 3D displacement measurements for the analysis of damage mechanisms in concrete-like materials. In J.G.M. Van Mier, G. Ruiz, C. Andrade, Yu R.C., and Zhang X.X., editors, *FraMCoS-8*, pages 1–11, 2013.

102. D.L.G. Hill, P.G. Batchelor, M. Holden, and D.J. Hawkes. Medical image registration. *PHYSICS IN MEDICINE AND BIOLOGY*, 46(3):R1, 2001.

103. Z. Hu, Y. Du, H. Luo, B. Zhong, and H. Lu. Internal Deformation Measurement and Force Chain Characterization of Mason Sand under Confined Compression using Incremental Digital Volume Correlation. *EXPERIMENTAL MECHANICS*, 54(9):1575–1586, 2014.

104. Z. Hu, H. Luo, S.G. Bardenhagen, C.R. Siviour, R.W. Armstrong, and H. Lu. Internal Deformation Measurement of Polymer Bonded Sugar in Compression by Digital Volume Correlation of In-situ Tomography. *EXPERIMENTAL MECHANICS*, 55(1):289–300, 2015.

105. J. Huang, X. Pan, S. Li, X. Peng, C. Xiong, and J. Fang. A digital volume correlation technique for 3-D deformation measurements of soft gels. *INTERNATIONAL JOURNAL OF APPLIED MECHANICS*, 3(2):335–354, 2011.

106. A.I. Hussein, Z.D. Mason, and E.F. Morgan. Presence of intervertebral discs alters observed stiffness and failure mechanisms in the vertebra. *JOURNAL OF BIOMECHANICS*, 46(10):1683–1688, 2013.

107. A.I. Hussein and E.F. Morgan. The effect of intravertebral heterogeneity in microstructure on vertebral strength and failure patterns. *OSTEOPOROSIS INTERNATIONAL*, 24(3):979–989, 2013.

108. T.M. Jackman, A.M. DelMonaco, and E.F. Morgan. Accuracy of finite element analyses of CT scans in predictions of vertebral failure patterns under axial compression and anterior flexion. *JOURNAL OF BIOMECHANICS*, 49(2):267–275, 2016.

109. T.M. Jackman, A.I. Hussein, C. Curtiss, P.M. Fein, A. Camp, L. De Barros, and E.F. Morgan. Quantitative, 3D Visualization of the Initiation and Progression of Vertebral Fractures Under Compression and Anterior Flexion. *JOURNAL OF BONE AND MINERAL RESEARCH*, 31(4):777–788, 2016.

110. C. Jailin, A. Bouterf, M. Poncelet, and S. Roux. In situ µCT Mechanical Tests: Fast 4D Mechanical Identification. *EXPERIMENTAL MECHANICS*, 57(8):1327–1340, 2017.

111. C. Jailin, A. Buljac, A. Bouterf, M. Poncelet, F. Hild, and S. Roux. Self-calibration for lab-µct using space-time regularized projection-based DVC and model reduction. *MEASUREMENT SCIENCE AND TECHNOLOGY*, in press, 2017.

112. T. Joffre, O. Girlanda, F. Forsberg, F. Sahlen, M. Sjodahl, and E.K. Gamstedt. A 3D in-situ investigation of the deformation in compressive loading in the thickness direction of cellulose fiber mats. *CELLULOSE*, 22(5):2993–3001, 2015.

113. T.R.C. Johnson, K. Nikolaou, B. J. Wintersperger, A. W. Leber, F. von Ziegler, C. Rist, S. Buhmann, A. Knez, M. F. Reiser, and C. R. Becker. Dual-source CT cardiac imaging: initial experience. *EUROPEAN RADIOLOGY*, 16(7):1409–1415, 2006.

114. A.C. Kak and M. Slaney. *Principles of computerized tomographic imaging*. IEEE Press, New York, 1988.

115. S. Klein, M. Staring, K. Murphy, M.A. Viergever, and J.P.W. Pluim. ELASTIX: A Toolbox for Intensity-Based Medical Image Registration. *IEEE TRANSACTIONS ON MEDICAL IMAGING*, 29(1):196–205, 2010.

116. M. Kobayashi, H. Toda, Y. Kawai, T. Ohgaki, K. Uesugi, D.S. Wilkinson, T. Kobayashi, Y. Aoki, and M. Nakazawa. High-density three-dimensional mapping of internal strain by tracking microstructural features. *ACTA MATERIALIA*, 56(10):2167–2181, 2008.

117. K. Krupa and M. Bekiesińska-Figatowska. Artifacts in magnetic resonance imaging. *POLISH JOURNAL OF RADIOLOGY*, 80:93, 2015.

118. S. Kullback. *Information theory and statistics*. John Wiley and Sons, New-York (USA), 1959.

119. J. Lachambre, J. Réthoré, A. Weck, and J.-Y. Buffière. Extraction of stress intensity factors for 3D small fatigue cracks using digital volume correlation and X-ray tomography. *INTERNATIONAL JOURNAL OF FATIGUE*, 71:3–10, 2015.

120. P. Ladevèze. PGD in linear and nonlinear computational solid mechanics. In *Separated Representations and PGD-Based Model Reduction*, pages 91–152. Springer, 2014.

121. H. Leclerc, J. Neggers, F. Mathieu, F. Hild, and S. Roux. Correli 3.0. Agence pour la Protection des Programmes, IDDN.FR.001.520008.000. S. P.2015.000.31500, 2015.

122. H. Leclerc, J.-N. Périé, F. Hild, and S. Roux. Digital volume correlation: what are the limits to the spatial resolution? *MECHANICS & INDUSTRY*, 13(6):361–371, 2012.

123. H. Leclerc, J-N. Périé, S. Roux, and F. Hild. Voxel-Scale Digital Volume Correlation. *EXPERIMENTAL MECHANICS*, 51(4):479–490, 2011.

124. H. Leclerc, S. Roux, and F. Hild. Projection Savings in CT-based Digital Volume Correlation. *EXPERIMENTAL MECHANICS*, 55(1):275–287, 2015.

125. P. Lecomte-Grosbras, J. Réthoré, N. Limodin, J.-F. Witz, and M. Brieu. Three-Dimensional Investigation of Free-Edge Effects in Laminate Composites Using X-ray Tomography and Digital Volume Correlation. *EXPERIMENTAL MECHANICS*, 55(1):301–311, 2015.

126. J. Lemaitre. *A Course on Damage Mechanics*. Springer-Verlag, Berlin (Germany), 1992.

127. N. Lenoir, M. Bornert, J. Desrues, P. Bésuelle, and G. Viggiani. Volumetric digital image correlation applied to X-ray microtomography images from triaxial compression tests on argillaceous rock. *STRAIN*, 43:193–205, 2007.

128. P. Leplay, J. Réthoré, S. Meille, M.-C. Baietto, J. Adrien, J. Chevalier, and E. Maire. Three-dimensional Analysis of an In Situ Double-torsion Test by X-ray Computed Tomography and Digital Volume Correlation. *EXPERIMENTAL MECHANICS*, 53(7):1265–1275, 2013.

129. A. Lesman, J. Notbohm, D.A. Tirrel, and G. Ravichandran. Contractile forces regulate cell division in three-dimensional environments. *JOURNAL OF CELL BIOLOGY*, 205(2):155–162, 2014.

130. K.Y. Lim, J.T. Henderson, and C.P. Neu. Cell and tissue deformation measurements: Texture correlation with third-order approximation of displacement gradients. *JOURNAL OF BIOMECHANICS*, 46(14):2490–2496, 2013.

131. N. Limodin, J. Réthoré, J. Adrien, J.-Y. Buffière, F. Hild, and S. Roux. Analysis and Artifact Correction for Volume Correlation Measurements Using Tomographic Images from a Laboratory X-ray Source. *EXPERIMENTAL MECHANICS*, 51(6):959–970, 2011.

132. N. Limodin, J. Réthoré, J.-Y. Buffière, F. Hild, S. Roux, W. Ludwig, J. Rannou, and A. Gravouil. Influence of closure on the 3D propagation of fatigue cracks in a nodular cast iron investigated by X-ray tomography and 3D Volume Correlation. *ACTA MATERIALIA*, 58(8):2957–2967, 2010.

133. N. Limodin, J. Réthoré, J.Y. Buffière, A. Gravouil, F. Hild, and S. Roux. Crack closure and stress intensity factor measurements in nodular graphite cast iron using 3D correlation of laboratory X ray microtomography images. *ACTA MATERIALIA*, 57(14):4090–4101, 2009.

134. L. Liu and E.F. Morgan. Accuracy and precision of digital volume correlation in quantifying displacements and strains in trabecular bone. *JOURNAL OF BIOMECHANICS*, 40(15):3516–3520, 2007.

135. W. Ludwig, J.-Y. Buffière, S. Savelli, and P. Cloetens. Study of the interaction of a short fatigue crack with grain boundaries in a cast Al alloy using X-ray microtomography. *ACTA MATERIALIA*, 51(3):585–598, 2003.

136. P. Ludwik. *Elemente der technologischen Mechanik*. Verlag Von Julius Springer, Leipzig (Germany), 1909.

137. K. Madi, G. Tozzi, Q. H. Zhang, J. Tong, A. Cossey, A. Au, D. Hollis, and F. Hild. Computation of full-field displacements in a scaffold implant using digital volume correlation and finite element analysis. *MEDICAL ENGINEERING & PHYSICS*, 35(9):1298–1312, 2013.

138. B.A. Mae. *The revolution in Medical Imaging*. Rosen Pub. Group, New York, NY (USA), 2003.

139. F. Maes, A. Collignon, D. Vandermeulen, G. Marchal, and P. Suetens. Multimodality image registration by maximization of mutual information. *IEEE TRANSACTIONS ON MEDICAL IMAGING*, 16(2):187–198, 1997.

140. P. C. Mahalanobis. On the generalised distance in statistics. *PROCEEDINGS OF THE NATIONAL INSTITUTE OF SCIENCES OF INDIA*, pages 49–55, 1936.

141. J.B.A. Maintz and M.A. Viergever. A survey of medical image registration. *MEDICAL IMAGE ANALYSIS*, 2(1):1–36, 1998.

142. E. Maire, J.-Y. Buffière, L. Salvo, J. J. Blandin, W. Ludwig, and J.-M. Létang. On the application of x-ray microtomography in the field of materials science. *ADVANCED ENGINEERING MATERIALS*, 3(8):539–546, 2001.

143. E. Maire, C. Le Bourlot, J. Adrien, A. Mortensen, and R. Mokso. 20-Hz X-ray tomography during an in situ tensile test. *INTERNATIONAL JOURNAL OF FRACTURE*, 200(1):3–12, 2016.

144. E. Maire and P. J. Withers. Quantitative X-ray tomography. *INTERNATIONAL MATERIALS REVIEWS*, 59(1):1–43, 2014.

145. M. Makitalo and A. Foi. Optimal inversion of the generalized anscombe transformation for poisson-gaussian noise. *IEEE TRANSACTIONS ON IMAGE PROCESSING*, 22(1):91–103, 2013.

146. V. Malfroy Camine, H.A. Rudiger, D.P. Pioletti, and A. Terrier. Full-field measurement of micromotion around a cementless femoral stem using micro-CT imaging and radiopaque markers. *JOURNAL OF BIOMECHANICS*, 49(16):4002–4008, 2016.

147. T.J. Marrow, M. Mostafavi, T. Hashimoto, and G.E. Thompson. A quantitative three-dimensional in situ study of a short fatigue crack in a magnesium alloy. *INTERNATIONAL JOURNAL OF FATIGUE*, 66:183–193, 2014.

148. S.A. Maskarinec, C. Franck, D.A. Tirrell, and G. Ravichandran. Quantifying cellular traction forces in three dimensions. *PROCEEDINGS OF THE NATIONAL ACADEMY OF SCIENCES OF THE UNITED STATES OF AMERICA*, 106(52):22108–22113, 2009.

149. F. Mathieu, F. Hild, and S. Roux. Identification of a crack propagation law by digital image correlation. *INTERNATIONAL JOURNAL OF FATIGUE*, 36:146–154, 2012.

150. F. Mathieu, H. Leclerc, F. Hild, and S. Roux. Estimation of elastoplastic parameters via weighted FEMU and integrated-DIC. *EXPERIMENTAL MECHANICS*, 55(1):105–119, 2015.

151. S.A. McDonald and P.J. Withers. Combining X-ray microtomography and three-dimensional digital volume correlation to track microstructure evolution during sintering of copper powder. *JOURNAL OF STRAIN ANALYSIS FOR ENGINEERING DESIGN*, 49(4):257–269, 2014.

152. A. Mendoza, S. Roux, J. Schneider, and E. Parra. Extraction of topological differences in woven composite materials. In *7th Conference on Industrial Computed Tomography*, 2017.

153. A. Mendoza, S. Roux, J. Schneider, E. Parra, and E. Obert. Unwrapping textile fabric. In *3rd International Conference on Tomography of Materials and Structures*, 2017.

154. E. H. Moore. On the reciprocal of the general algebraic matrix. *BULLETIN AMERICAN MATHEMMATICAL SOCIETY*, 2(26):394–395, 1920.

155. P. Morandi, E. Brémand, P. Doumalin, A. Germaneau, and J.-C. Dupré. New Optical Scanning Tomography using a rotating slicing for time-resolved measurements of 3D full field displacements in structures. *OPTICS AND LASERS IN ENGINEERING*, 58:85–92, 2014.

156. T.F. Morgeneyer, L. Helfen, H. Mubarak, and F. Hild. 3D Digital Volume Correlation of Synchrotron Radiation Laminography Images of Ductile Crack Initiation: An Initial Feasibility Study. *EXPERIMENTAL MECHANICS*, 53(4):543–556, 2013.

157. T.F. Morgeneyer, T. Taillandier-Thomas, A. Buljac, L. Helfen, and F. Hild. On strain and damage interactions during tearing: 3D in situ measurements and simulations for a ductile alloy (AA2139-T3). *JOURNAL OF THE MECHANICS AND PHYSICS OF SOLIDS*, 96:550–571, 2016.

158. T.F. Morgeneyer, T. Taillandier-Thomas, L. Helfen, T. Baumbach, I. Sinclair, S. Roux, and F. Hild. In situ 3-D observation of early strain localization during failure of thin Al alloy (2198) sheet. *ACTA MATERIALIA*, 69:78–91, 2014.

159. F. Mortazavi, E. Ghossein, M. Levesque, and I. Villemure. High resolution measurement of internal full-field displacements and strains using global spectral digital volume correlation. *OPTICS AND LASERS IN ENGINEERING*, 55:44–52, 2014.

160. M. Mostafavi, N. Baimpas, E. Tarleton, R.C. Atwood, S.A. McDonald, A.M. Korsunsky, and T.J. Marrow. Three-dimensional crack observation, quantification and simulation in a quasi-brittle material. *ACTA MATERIALIA*, 61(16):6276–6289, 2013.

161. M. Mostafavi, R. Bradley, D.E.J. Armstrong, and T.J. Marrow. Quantifying yield behaviour in metals by X-ray nanotomography. *SCIENTIFIC REPORTS*, 6:34346, 2016.

162. M. Mostafavi, D.M. Collins, B. Cai, R. Bradley, R.C. Atwood, C. Reinhard, X. Jiang, M. Galano, P.D. Lee, and T.J. Marrow. Yield behavior beneath hardness indentations in ductile metals, measured by three-dimensional computed X-ray tomography and digital volume correlation. *ACTA MATERIALIA*, 82:468–482, 2015.

163. M. Mostafavi, S.A. McDonald, H. Cetinel, P.M. Mummery, and T.J. Marrow. Flexural strength and defect behaviour of polygranular graphite under different states of stress. *CARBON*, 59:325–336, 2013.

164. A. Nahas, M. Bauer, S. Roux, and A.C. Boccara. 3D static elastography at the micrometer scale using Full Field OCT. *BIOMEDICAL OPTICS EXPRESS*, 4(10):2138–2149, 2013.

165. J. Neggers, O. Allix, F. Hild, and S. Roux. Big Data in Experimental Mechanics and Model Order Reduction: Today's Challenges and Tomorrow's Opportunities. *ARCHIVES OF COMPUTATIONAL METHODS IN ENGINEERING*, 24:1–22, 2017.

166. T.T. Nguyen, J. Yvonnet, M. Bornert, and C. Chateau. Initiation and propagation of complex 3D networks of cracks in heterogeneous quasi-brittle materials: Direct comparison between in situ testing-microCT experiments and phase field simulations. *JOURNAL OF THE MECHANICS AND PHYSICS OF SOLIDS*, 95:320–350, 2016.

167. R.A. Novelline. *Squire's Fundamentals of Radiology*. Harvard University Press, Cambridge, MA (USA), 2018.

168. M. Palanca, L. Cristofolini, E. Dall'Ara, M. Curto, F. Innocente, V. Danesi, and G. Tozzi. Digital volume correlation can be used to estimate local strains in natural and augmented vertebrae: An organ-level study. *JOURNAL OF BIOMECHANICS*, 49(16):3882–3890, 2016.

169. M. Palanca, G. Tozzi, L. Cristofolini, M. Viceconti, and E. Dall'Ara. Three-Dimensional Local Measurements of Bone Strain and Displacement: Comparison of Three Digital Volume Correlation Approaches. *JOURNAL OF BIOMECHANICAL ENGINEERING-TRANSACTIONS OF THE ASME*, 137(7):071006, 2015.

170. B. Pan, B. Wang, D. Wu, and G. Lubineau. An efficient and accurate 3D displacements tracking strategy for digital volume correlation. *OPTICS AND LASERS IN ENGINEERING*, 58:126–135, 2014.

171. B. Pan, D. Wu, and Z. Wang. Internal displacement and strain measurement using digital volume correlation: a least-squares framework. *MEASUREMENT SCIENCE AND TECHNOLOGY*, 23(4), 2012.

172. K.J. Parker, M.M. Doyley, and D.J. Rubens. Corrigendum 1: Imaging the elastic properties of tissue: the 20 year perspective. *PHYSICS IN MEDICINE & BIOLOGY*, 56(2):513, 2011.

173. K.J. Parker, M.M. Doyley, and D.J. Rubens. Imaging the elastic properties of tissue: the 20 year perspective. *PHYSICS IN MEDICINE & BIOLOGY*, 56(1):R1, 2011.

174. K.J. Parker, M.M. Doyley, and D.J. Rubens. Corrigendum 2: Imaging the elastic properties of tissue: the 20 year perspective. *PHYSICS IN MEDICINE & BIOLOGY*, 57(16):5359, 2012.

175. J.-C. Passieux and J.-N. Périé. High resolution digital image correlation using proper generalized decomposition: PGD-DIC. *INTERNATIONAL JOURNAL FOR NUMERICAL METHODS IN ENGINEERING*, 92(6):531–550, 2012.

176. J.-C. Passieux, J.-N. Périé, and M. Salaün. A dual domain decomposition method for finite element digital image correlation. *INTERNATIONAL JOURNAL FOR NUMERICAL METHODS IN ENGINEERING*, 102(10):1670–1682, 2015.

177. B.M. Patterson, N.L. Cordes, K. Henderson, J.C. E. Mertens, A.J. Clarke, B. Hornberger, A. Merkle, S. Etchin, A. Tkachuk, M. Leibowitz, D. Trapp, W. Qiu, B. Zhang, H. Bale, X. Lu, R. Hartwell, P.J. Withers, and R.S. Bradley. In Situ Laboratory-Based Transmission X-Ray Microscopy and Tomography of Material Deformation at the Nanoscale. *EXPERIMENTAL MECHANICS*, 56(9):1585–1597, 2016.

178. J.M. Paz-Garcia, O.O. Taiwo, E. Tudisco, D.P. Finegan, P.R. Shearing, D.J.L. Brett, and S.A. Hall. 4D analysis of the microstructural evolution of Si-based electrodes during lithiation: Time-lapse X-ray imaging and digital volume correlation. *JOURNAL OF POWER SOURCES*, 320:196–203, 2016.

179. R. Penrose. On best approximate solutions of linear matrix equations. *MATHEMATICAL PROCEEDINGS OF THE CAMBRIDGE PHILOSOPHICAL SOCIETY*, 52(1):17–19, 1956.

180. M. Petersilka, H. Bruder, Bernhard Krauss, Karl Stierstorfer, and Thomas G Flohr. Technical principles of dual source CT. *EUROPEAN JOURNAL OF RADIOLOGY*, 68(3):362–368, 2008.

181. F. Pierron, S.A. McDonald, D. Hollis, J. Fu, P.J. Withers, and A. Alderson. Comparison of the Mechanical Behaviour of Standard and Auxetic Foams by X-ray Computed Tomography and Digital Volume Correlation. *STRAIN*, 49(6):467–482, 2013.

182. D.P. Popescu, L.-P. Choo-Smith, C. Flueraru, Y. Mao, S. Chang, J. Disano, S. Sherif, and M.G. Sowa. Optical coherence tomography: fundamental principles, instrumental designs and biomedical applications. *BIOPHYSICAL REVIEWS*, 3(3):155–169, 2011.

183. D. Prell, Y. Kyriakou, and W.A. Kalender. Comparison of ring artifact correction methods for flat-detector CT. *PHYSICS IN MEDICINE & BIOLOGY*, 54(12):3881, 2009.

184. B. Rahmani, E. Ghossein, I. Villemure, and M. Levesque. In-situ mechanical properties identification of 3D particulate composites using the Virtual Fields Method. *INTERNATIONAL JOURNAL OF SOLIDS AND STRUCTURES*, 51(18):3076–3086, 2014.

185. J. Rannou, N. Limodin, J. Réthore, A. Gravouil, W. Ludwig, M.-C. Baietto-Dubourg, J.-Y. Buffière, A. Combescure, F. Hild, and S. Roux. Three dimensional experimental and numerical multiscale analysis of a fatigue crack. *COMPUTER METHODS IN APPLIED MECHANICS AND ENGINEERING*, 199(21-22):1307–1325, 2010.

186. M. Ren, J. Liang, and B. Wei. Accurate B-spline-based 3-D interpolation scheme for digital volume correlation. *REVIEW OF SCIENTIFIC INSTRUMENTS*, 87(12):125114, 2016.

187. J. Réthoré, F. Hild, and S. Roux. Shear-band capturing using a multiscale extended digital image correlation technique. *COMPUTER METHODS IN APPLIED MECHANICS AND ENGINEERING*, 196(49-52):5016–5030, 2007.

188. J. Réthoré, F. Hild, and S. Roux. Extended digital image correlation with crack shape optimization. *INTERNATIONAL JOURNAL FOR NUMERICAL METHODS IN ENGINEERING*, 73(2):248–272, 2008.

189. J. Réthoré, N. Limodin, J.-Y. Buffière, F. Hild, W. Ludwig, and S. Roux. Digital volume correlation analyses of synchrotron tomographic images. *JOURNAL OF STRAIN ANALYSIS FOR ENGINEERING DESIGN*, 46(7):683–695, 2011.

190. J. Réthoré, S. Roux, and F. Hild. An extended and integrated digital image correlation technique applied to the analysis fractured samples. *EUROPEAN JOURNAL OF COMPUTATIONAL MECHANICS*, 18:285–306, 2009.

191. J. Réthoré, S. Roux, and F. Hild. Optimal and noise-robust extraction of fracture mechanics parameters from kinematic measurements. *ENGINERRING FRACTURE MECHANICS*, 78(9):1827–1845, 2011.

192. J. Réthoré, J.-P. Tinnes, S. Roux, J.-Y. Buffière, and F. Hild. Extended three-dimensional digital image correlation (x3d-dic). *COMPTES RENDUS MÉCANIQUE*, 336:643–649, 2008.

193. B.C. Roberts, E. Perilli, and K.J. Reynolds. Application of the digital volume correlation technique for the measurement of displacement and strain fields in bone: A literature review. *JOURNAL OF BIOMECHANICS*, 47(5):923–934, 2014.

194. B.A. Roeder, K. Kokini, J.P. Robinson, and S.L. Voytik-Harbin. Local, three-dimensional strain measurements within largely deformed extracellular matrix constructs. *JOURNAL OF BIOMECHANICAL ENGINEERING-TRANSACTIONS OF THE ASME*, 126(6):699–708, 2004.

195. T. Rohlfing, C.R. Maurer, D.A. Bluemke, and M.A. Jacobs. Volume-preserving nonrigid registration of MR breast images using free-form deformation with an incompressibility constraint. *IEEE TRANSACTIONS ON MEDICAL IMAGING*, 22(6):730–741, 2003.

196. S. Roux and F. Hild. Stress intensity factor measurements from digital image correlation: post-processing and integrated approaches. *INTERNATIONAL JOURNAL OF FRACTURE*, 140(1-4):141–157, 2006.

197. S. Roux, F. Hild, P. Viot, and D. Bernard. Three-dimensional image correlation from X-ray computed tomography of solid foam. *COMPOSITES PART A-APPLIED SCIENCE AND MANUFACTURING*, 39(8):1253–1265, 2008.

198. S. Roux, J. Réthoré, and F. Hild. Digital image correlation and fracture: An advanced technique for estimating stress intensity factors of 2d and 3d cracks. *JOURNAL OF PHYSICS D: APPLIED PHYSICS*, 42:214004, 2009.

199. D. Rueckert, L.I. Sonoda, C. Hayes, D.L.G. Hill, M.O. Leach, and D.J. Hawkes. Nonrigid registration using free-form deformations: application to breast MR images. *IEEE TRANSACTIONS ON MEDICAL IMAGING*, 18(8):712–721, 1999.

200. L. Salvo, P. Cloetens, E. Maire, S. Zabler, J.-J. Blandin, J.Y. Buffière, W. Ludwig, E. Boller, D. Bellet, and C. Josserond. X-ray micro-tomography an attractive characterisation technique in materials science. *NUCLEAR INSTRUMENTS AND METHODS IN PHYSICS RESEARCH SECTION B: BEAM INTERACTIONS WITH MATERIALS AND ATOMS*, 200:273–286, 2003.

201. L. Saucedo-Mora, M. Mostafavi, D. Khoshkhou, C. Reinhard, R. Atwood, S. Zhao, B. Connolly, and T.J. Marrow. Observation and simulation of indentation damage in a SiC-SiC fibre ceramic matrix composite. *FINITE ELEMENTS IN ANALYSIS AND DESIGN*, 110:11–19, 2016.

202. L. Saucedo-Mora, C. Zou, T. Lowe, and T.J. Marrow. Three-dimensional measurement and cohesive element modelling of deformation and damage in a 2.5-dimensional woven ceramic matrix composite. *FATIGUE & FRACTURE OF ENGINEERING MATERIALS & STRUCTURES*, 40(5):683–695, 2017.

203. F. Scarano. Tomographic PIV: principles and practice. *MEASUREMENT SCIENCE AND TECHNOLOGY*, 24(1):012001, 2013.

204. J. Schneider, H. Leclerc, F. Hild, and S. Roux. Procédé de caractérisation d'une pièce. Patent, WO2015092212 A1.

205. I.J. Schoenberg. Contributions to the Problem of Approximation of Equidistant Data by Analytic Functions. Part A. *QUARTERLY OF APPLIED MATHEMATICS*, 4:45–99, 1946.

206. M. Shakoor, A. Buljac, J. Neggers, F. Hild, T.F. Morgeneyer, L. Helfen, M. Bernacki, and P.-O. Bouchard. On the choice of boundary conditions for micromechanical simulations based on 3D imaging. *INTERNATIONAL JOURNAL OF SOLIDS AND STRUCTURES*, 112:83–96, 2017.

207. T.S. Smith, B.K. Bay, and M.M. Rashid. Digital volume correlation including rotational degrees of freedom during minimization. *EXPERIMENTAL MECHANICS*, 42(3):272–278, 2002.

208. S.R. Stock. Recent advances in X-ray microtomography applied to materials. *INTERNATIONAL MATERIALS REVIEWS*, 53(3):129–181, 2008.

209. C. Studholme, D.L.G. Hill, and D.J. Hawkes. Automated 3-D registration of MR and CT images of the head. *MEDICAL IMAGE ANALYSIS*, 1(2):163–175, 1996.

210. C. Sukjamsri, D.M. Geraldes, T. Gregory, F. Ahmed, D. Hollis, S. Schenk, A. Amis, R. Emery, and U. Hansen. Digital volume correlation and micro-CT: An in-vitro technique for measuring full-field interface micromotion around polyethylene implants. *JOURNAL OF BIOMECHANICS*, 48(12):3447–3454, 2015.

211. F. Sur and M. Grédiac. Measuring the noise of digital imaging sensors by stacking raw images affected by vibrations and illumination flickering. *SIAM JOURNAL OF IMAGING SCIENCES*, 8(1):611–643, 2015.

212. M.A. Sutton, J.J. Orteu, and H. Schreier. *Image correlation for shape, motion and deformation measurements: Basic Concepts, Theory and Applications*. Springer, New York, NY (USA), 2009.

213. T. Taillandier-Thomas, S. Roux, and F. Hild. Soft Route to 4D Tomography. *PHYSICAL REVIEW LETTERS*, 117(2):025501, 2016.

214. T. Taillandier-Thomas, S. Roux, T.F. Morgeneyer, and F. Hild. Localized strain field measurement on laminography data with mechanical regularization. *NUCLEAR INSTRUMENTS & METHODS IN PHYSICS RESEARCH SECTION B-BEAM INTERACTIONS WITH MATERIALS AND ATOMS*, 324:70–79, 2014.

215. A.N. Tikhonov and V.Y. Arsenin. *Solutions of ill-posed problems*. J. Wiley, New York (USA), 1977.

216. H. Toda, E. Maire, Y. Aoki, and M. Kobayashi. Three-dimensional strain mapping using in situ X-ray synchrotron microtomography. *JOURNAL OF STRAIN ANALYSIS FOR ENGINEERING DESIGN*, 46(7):549–561, 2011.

217. H. Toda, I. Sinclair, J.-Y. Buffière, E. Maire, K.H. Khor, P. Gregson, and T. Kobayashi. A 3d measurement procedure for internal local crack driving forces via synchrotron x-ray microtomography. *ACTA MATERIALIA*, 52:1305–1317, 2004.

218. Z. Tomičević, F. Hild, and S. Roux. Mechanics-aided digital image correlation. *JOURNAL OF STRAIN ANALYSIS FOR ENGINEERING DESIGN*, 48:330–343, 2013.

219. Z. Tomičević, J. Kodvanj, and F. Hild. Characterization of the nonlinear behavior of nodular graphite cast iron via inverse identification-Analysis of uniaxial tests. *EUROPEAN JOURNAL OF MECHANICS A-SOLIDS*, 59:140–154, 2016.

220. G. Tozzi, V. Danesi, M. Palanca, and L. Cristofolini. Elastic Full-Field Strain Analysis and Microdamage Progression in the Vertebral Body from Digital Volume Correlation. *STRAIN*, 52(5):446–455, 2016.

221. G. Tozzi, Q.-H. Zhang, and J. Tong. Microdamage assessment of bone-cement interfaces under monotonic and cyclic compression. *JOURNAL OF BIOMECHANICS*, 47(14):3466–3474, 2014.

222. H. Tran, P. Doumalin, C. Delisée, J.-C. Dupré, J. Malvestio, and A. Germaneau. 3D mechanical analysis of low-density wood-based fiberboards by X-ray microcomputed tomography and Digital Volume Correlation. *JOURNAL OF MATERIALS SCIENCE*, 48(8):3198–3212, 2013.

223. C. Truesdell and W. Noll. *The Non-Linear Field Theories of Mechanics*, volume III/3. Springer-Verlag, Berlin (Germany), 1965.

224. E. Tudisco, S.A. Hall, E.M. Charalampidou, N. Kardjilov, A. Hilger, and H. Sone. Full-field Measurements of Strain Localisation in Sandstone by Neutron Tomography and 3D-Volumetric Digital Image Correlation. *PHYSICS PROCEDIA*, 69:509–515, 2015.

225. E. Tudisco, C. Jailin, A. Mendoza, A. Tengattini, E. Andò, S. Hall, G. Viggiani, F. Hild, and S. Roux. An extension of digital volume correlation for multimodality image registration. *MEASUREMENT SCIENCE AND TECHNOLOGY*, 28(9):095401, 2017.

226. I. Vajda. *Theory of statistical inference and information*, volume 11. Kluwer Academic Pub, 1989.

227. W. Van Aarle, W.J. Palenstijn, J. De Beenhouwer, T. Altantzis, S. Bals, K.J. Batenburg, and J. Sijbers. The ASTRA Toolbox: A platform for advanced algorithm development in electron tomography. *ULTRAMICROSCOPY*, 157:35–47, 2015.

228. P.A. van den Elsen, E.J.D. Pol, and M.A. Viergever. Medical image matching: a review with classification. *IEEE ENGINEERING IN MEDICINE AND BIOLOGY MAGAZINE*, 12(1):26–39, 1993.

229. G. Van Gompel, K. Van Slambrouck, M. Defrise, K. J. Batenburg, J. de Mey, J. Sijbers, and J. Nuyts. Iterative correction of beam hardening artifacts in CT. *MEDICAL PHYSICS*, 38(S1):S36–S49, 2011.

230. E. Verhulp, B. van Rietbergen, and R. Huiskes. A three-dimensional digital image correlation technique for strain measurements in microstructures. *JOURNAL OF BIOMECHANICS*, 37(9):1313–1320, 2004.

231. Y. Vertyagina, M. Mostafavi, C. Reinhard, R. Atwood, and T.J. Marrow. In situ quantitative three-dimensional characterisation of sub-indentation cracking in polycrystalline alumina. *JOURNAL OF THE EUROPEAN CERAMIC SOCIETY*, 34(12):3127–3132, 2014.

232. K. Wan and P. Yang. Expanded digital volume correlation for ex situ applications. *MEASUREMENT SCIENCE AND TECHNOLOGY*, 26(9), 2015.

233. B. Wang, B. Pan, R. Tao, and G. Lubineau. Systematic errors in digital volume correlation due to the self-heating effect of a laboratory x-ray CT scanner. *MEASUREMENT SCIENCE AND TECHNOLOGY*, 28(5):055402, 2017.

234. L. Wang, N. Limodin, A. El Bartali, J.-F. Witz, R. Seghir, J.-Y. Buffière, and E. Charkaluk. Influence of pores on crack initiation in monotonic tensile and cyclic loadings in lost foam casting A319 alloy by using 3D in-situ analysis. *MATERIALS SCIENCE AND ENGINEERING A-STRUCTURAL MATERIALS PROPERTIES MICROSTRUCTURE AND PROCESSING*, 673:362–372, 2016.

235. T. Wang, Z. Jiang, Q. Kemao, F. Lin, and S.H. Soon. GPU Accelerated Digital Volume Correlation. *EXPERIMENTAL MECHANICS*, 56(2):297–309, 2016.

236. W. M. Wells, P. Viola, H. Atsumi, S. Nakajima, and R. Kikinis. Multi-modal volume registration by maximization of mutual information. *MEDICAL IMAGE ANALYSIS*, 1(1):35–51, 1996.

237. P.J. Withers. X-ray nanotomography. *MATERIALS TODAY*, 10(12):26–34, 2007.

238. F. Xu, L. Helfen, T. Baumbach, and H. Suhonen. Comparison of image quality in computed laminography and tomography. *OPTICS EXPRESS*, 20:794–806, 2012.

239. S. Xu and K.J. Grande-Allen. The Evolution of the Field of Biomechanics Through the Lens of Experimental Mechanics. *EXPERIMENTAL MECHANICS*, 50(6):667–682, 2010.

240. Z. Yang, W. Ren, R. Sharma, S. McDonald, M. Mostafavi, Y. Vertyagina, and T.J. Marrow. In-situ X-ray computed tomography characterisation of 3D fracture evolution and image-based numerical homogenisation of concrete. *CEMENT & CONCRETE COMPOSITES*, 75:74–83, 2017.

241. Y.N. Yeni, B. Wu, L. Huang, and D. Oravec. Mechanical Loading Causes Detectable Changes in Morphometric Measures of Trabecular Structure in Human Cancellous Bone. *JOURNAL OF BIOMECHANICAL ENGINEERING-TRANSACTIONS OF THE ASME*, 135(5):54505, 2013.

242. R. Zauel, Y.N. Yeni, B.K. Bay, X.N. Dong, and D.P. Fyhrie. Comparison of the linear finite element prediction of deformation and strain of human cancellous bone to 3D digital volume correlation measurements.

JOURNAL OF BIOMECHANICAL ENGINEERING-TRANSACTIONS OF THE ASME, 128(1):1–6, 2006.

243. M.-L. Zhu, Q.-H. Zhang, C. Lupton, and J. Tong. Spatial resolution and measurement uncertainty of strains in bone and bone-cement interface using digital volume correlation. *JOURNAL OF THE MECHANICAL BEHAVIOR OF BIOMEDICAL MATERIALS*, 57:269–279, 2016.

244. X. Zhuge, W. J. Palenstijn, and K. J. Batenburg. TVR-DART: a more robust algorithm for discrete tomography from limited projection data with automated gray value estimation. *IEEE TRANSACTIONS ON IMAGE PROCESSING*, 25(1):455–468, 2016.

245. B. Zitová and J. Flusser. Image registration methods: a survey. *IMAGE AND VISION COMPUTING*, 21(11):977–1000, 2003.